

Tunable Permittivity Sensors

by

Alaaeldin Ahmed

A thesis

presented to the University of Waterloo

in fulfillment of the

thesis requirement for the degree of

Doctor of Philosophy

in

Systems Design Engineering

Waterloo, Ontario, Canada, 2021

© Alaaeldin Ahmed 2021

Examining Committee Membership

The following served on the Examining Committee for this thesis. The decision of the Examining Committee is by majority vote.

External Examiner	Mohammed Daqaq Professor
Supervisor	Eihab Abdel-Rahman Professor
Supervisor	Mohamad Basha Research Associate Professor
Internal Member	Glenn Heppler Professor
Internal Member	Mustafa Yavuz Professor
Internal-external Member	Safieddin Safavi-Naeini Professor

Author's Declaration

This thesis consists of material all of which I authored or co-authored: see Statement of Contributions included in the thesis. This is a true copy of the thesis, including any required final revisions, as accepted by my examiners. I understand that my thesis may be made electronically available to the public.

Statement of Contributions

Certain parts of this thesis are based on co-authored published research, as detailed here:

Chapter 5: (Section 3, Subsection 1)

Elhady, Alaa and E. M. Abdel-Rahman, “Characterization of shear horizontal waves using a 1D laser Doppler vibrometer,” *Sensors*, vol. 21, no. 7, p. 2467, 2021

This paper, co-authored with my supervisor, Prof. Eihab Abdel-Rahman, details a novel method to characterize Shear-Horizontal Surface Acoustic Waves using a one-dimensional Laser Doppler Vibrometer. In this paper, I developed the conceptualization, visualization, experimental validation, and wrote the paper draft. I worked alongside Prof. Abdel-Rahman on the methodology. Prof. Abdel-Rahman also provided manuscript revision and supervision.

Chapter 6:

Elhady, Alaa, M. Basha, and E. M. Abdel-Rahman, “Analysis of tunable Bleustein-Gulyaev permittivity sensors,” *Journal of Applied Physics*, vol. 129, no. 16, p. 164501, 2021

This paper, co-authored with my supervisors, Dr. Mohamed Basha and Prof. Eihab Abdel-Rahman, details the modeling and experimental validation of the BG sensor DC Forced response. In this paper, I developed the concepts and performed the simulation using both mathematical and Finite Element modeling. I also executed the experimental validation, created the visualization, and wrote the paper draft. I worked alongside Prof. Abdel-Rahman on the investigation and mathematical modeling. Prof. Abdel-Rahman and Dr. Basha both provided manuscript revision and supervision.

Chapter 7:

Elhady, Alaa, M. Basha, and E. M. Abdel-Rahman, “Measurement of electric permittivity using Bleustein-Gulyaev wave sensors,” *Journal of Micromechanics and Microengineering*, 2021. In progress

This work is still in progress. It has not yet been accepted for publication.

This paper, co-authored with my supervisors, Dr. Mohamed Basha and Prof. Eihab Abdel-Rahman, details the modeling and experimental validation of the dynamic permittivity sensor. In this paper, I developed a rigorous mathematical framework with supervision from Prof. Abdel-Rahman. I also performed the simulation, carried out the experiments, and conducted the data collection and analysis. Finally, I wrote the paper draft. Prof. Abdel-Rahman and Dr. Basha both provided manuscript revision and supervision.

Abstract

This thesis presents a novel electric permittivity sensor based on Bleustein-Gulyaev (BG) waves; waves that propagate along the surface of shear-poled piezoelectric materials. BG waves couple electromagnetic and acoustic waves, thereby reducing the speed of electromagnetic propagation to near acoustic speeds. Exploiting this property allows the development of permittivity sensors that feature several orders of magnitude reduction in size and operating frequency. This releases the limitations of RF complexity while reducing cost considerably. It also makes the sensor attractive for biological applications, as opposed to RF sensors that are limited by the water relaxation phenomenon at frequencies beyond 4 GHz.

To date, sensors that used BG waves were limited to sensing mechanical properties, such as viscosity and density, which exploited the acoustic component of the wave only. To our best knowledge, this is the first attempt to probe and sense an electrical property acoustically using BG-waves.

Towards that end, the nonlinear partial differential equations governing an electromechanical BG wave resonator are formulated. The permittivity of the medium-under-test was found to influence the sensor eigenvalues, enabling the implementation of a frequency-shift permittivity sensor. We also find that the sensor sensitivity is enhanced by increasing bias voltage to drive the sensor into the nonlinear regime, but this is limited by electrical breakdown.

Sensor prototypes were fabricated on PZT4 and LiNbO_3 shear-poled substrates. A novel method to characterize shear-horizontal surface acoustic waves, SH-SAW, using a 1D Laser Doppler Vibrometer was developed to test the sensors.

The method was also shown to be able to estimate the in-plane displacement field decay rate into the substrate. This technique provides researchers with a quick and effective method for the characterization of SH-SAW. The resonator model was validated using this experimental method.

A Vector Network Analyzer was employed to observe the shift in the fundamental natural frequency of the fabricated permittivity sensors in the presence of various media-under-test. Measurements show deterministic and repeatable frequency shifts in the natural frequency in the presence of ethanol and deionized water compared to that of the bare surface, thereby demonstrating the permittivity sensor.

Acknowledgments

All praise is due to God for providing me with the guidance, strength, and patience to write this thesis.

Next, I would like to thank my supervisors, Prof. Eihab Abdel-Rahman, and Dr. Mohamed Basha, for their support and guidance. I would also like to thank CMC for the MNT funding that made the fabrication possible.

Further, I would like to thank my parents for instilling me with a strong passion for science. Finally, I wish to express my deep gratitude and sincere thanks to my wife for her patience, encouragement, and continuous support.

Thank you all.

Table of Contents

Examining Committee Membership	ii
Author's Declaration	iii
Statement of Contributions	iv
Abstract	vi
Acknowledgments	viii
List of Figures	xiv
List of Tables	xx
Nomenclature	xxi
1 Introduction	1
1.1 Piezoelectricity	1
1.2 Bleustein-Gulyaev Waves	2
1.3 Permittivity Sensors	5
1.4 Problem Statement and Objectives	8
2 BG Resonator	11

2.1	BG Wave Equations	11
2.1.1	Field Definitions	12
2.1.2	Constitutive Equations	12
2.1.3	Governing Equations	13
2.1.4	Boundary Conditions	14
2.2	Solution of the Homogeneous Equations	16
2.3	Quasi-static approximation	21
2.4	Nondimensionalization	22
2.5	Summary	25
3	Nonlinearity in BG Waves	26
3.1	Sources of Nonlinearities	27
3.1.1	Electrostriction Nonlinearity	30
3.2	Nonlinear Constitutive and Governing Equations	33
3.3	Linearization Around a Bias Point	35
3.4	Nondimensionalization	36
3.5	Summary	37
4	Eigenvalue Analysis	38
4.1	Sensor Eigenvalue Problem	38
4.1.1	Metallized Surface	39
4.1.2	Bare Surface	40
4.1.3	Higher Modes	41
4.2	Sensor Sensitivity	42
4.3	Eigenfunctions	44
4.4	Summary	46

5	Sensor Design, Fabrication, and Characterization	47
5.1	Sensor Prototypes	47
5.1.1	Sensor Design	47
5.1.2	PZT4 Sensors	50
5.1.3	LiNbO ₃ Sensors	51
5.2	Fabrication	54
5.2.1	Fabrication Process	54
5.2.2	Post-Processing	60
5.3	Optical Detection	65
5.3.1	Optical Characterization of SH Wave	68
5.3.2	Relationship Between In-Plane and Out-of-Plane Displacements	69
5.3.3	Linear Static Response	75
5.4	Electrical Detection	79
5.4.1	Experimental Setup	79
5.4.2	Modeling of S-Parameters	81
5.5	Summary	84
6	Non-Resonant Excitation	85
6.1	Excitation and Damping Mechanisms	85
6.1.1	Charge Excitation	85
6.1.2	Damping	86
6.2	Linear Static Response	87
6.3	Nonlinear Static Response	89
6.4	Simulation Results	92
6.4.1	Finite Element Model	92
6.4.2	Reduced-Order Model	93

6.5	Experimental Verification	101
6.6	Summary	102
7	Resonant Excitation	105
7.1	Linear BG Resonator	105
7.2	Nonlinear BG Resonator	107
7.2.1	Problem Statement	107
7.2.2	Discretization	108
7.2.3	Numerical Solution	111
7.3	Simulation Results	111
7.4	Experimental Validation	119
7.4.1	Experimental Setup	121
7.4.2	Permittivity Sensor Validation	121
7.5	Summary	126
8	Conclusion and Future Work	127
8.1	Conclusion	127
8.2	Future Work	129
	Bibliography	131
	Appendices	149
A	Material Constants	150
B	Tensor Manipulations	151
C	Nonlinear Operators and Equations	153

C.1 Electrostriction Operators	153
C.2 Equilibrium Equations	154
C.3 Equations of Motion	155

List of Figures

1.1	Standard IDT geometry used to excite SAW	3
2.1	Sensor schematic showing the substrate, medium-under-test, and the IDT design. The front section view is shown in (a) and the top view in (b).	14
3.1	The hysteresis loop of the polarization P created under an applied external electric field E in ferroelectric materials.	28
3.2	Linearized relative effective permittivity as a function of bias electric field. ϵ_o is the free space permittivity.	36
4.1	Excitation of the first and second modes, using 4 IDT fingers, including the two half-electrodes at the edges.	42
4.2	The sensitivity S_ω of a frequency-shift PZT4 sensor as a function of the medium relative permittivity ϵ_r^u	44
4.3	Biased sensitivity of PZT4, under applied biasing electric fields of $E_{x_o} = 0$ MV/m (black) and $E_{x_o} = 10$ MV/m (red). The blue markers track the position of maximum sensitivity.	45
5.1	The BG sensor IDT structure	48
5.2	Schematic of the use of metal electrode reflectors to reflect the wave and create the resonator.	49

5.3	Schematic of the resonator using deep trench edges to reflect the wave.	50
5.4	Post fabrication SEM photos for the PZT4. A grain defect was brought into focus and several close-up views were taken.	52
5.5	Different LiNbO ₃ designs	53
5.6	Photos for the PZT4 at different steps during fabrication	55
5.7	Process steps	56
5.8	Microscopic image of the LiNbO ₃ substrate with patterned IDT electrodes.	57
5.9	Microscopic image of the LiNbO ₃ substrate with patterned IDT electrodes using a different illumination method. LiNbO ₃ is semitransparent.	58
5.10	Microscopic image of the LiNbO ₃ substrate with a close-up view of the edge electrode. The electrode shows minimal over-etching.	59
5.11	Profilometer measurement of the IDT fingers on the PZT4 sensor.	59
5.12	Profilometer measurement of the IDT fingers on the LiNbO ₃ sensor. The mea- sured metal thickness does not match the manufacturer provided specifications. . .	60
5.13	Profilometer screenshot during the measurement of the LiNbO ₃ sensor. The scratches on the surface are superficial and do not pose a problem.	60
5.14	Laser trimming at resonator edges.	61
5.15	FEA COMSOL simulations of the effect of trench depth on containment of the BG wave. The wave was excited at resonance.	63
5.16	Profilometer screenshot during trench depth measurement on the PZT4 sensor. The gray line (lower left plot) represents interpolation by the profilometer soft- ware. The blue line indicates true measurement. The bottom of the trench was not captured by the profilometer sensor.	64
5.17	Localized heat damage near the trench due to the laser trimmer.	65
5.18	Experimental setups	66

5.19	LiNbO ₃ sensor directly probed, under the microscope.	67
5.20	(a) The experimental configuration of the proposed measurement technique. (b) Positions of the laser spot (marked by ⊗), the displacement field $u(x, y, z, t)$ (marked by the dashed-line arrows), and the propagation direction of the shear horizontal (SH) wave (marked by the double-line arrow).	69
5.25	Laser Doppler Vibrometer scan, showing the out-of-plane deflection in front of the finger tip, when the PZT4 sensor was excited at resonance.	74
5.26	FEA of out-of-plane motion in a BGW Sensor. The black box is the area scanned experimentally.	75
5.27	A microscopic image of the fabricated IDT for the BG wave resonator, showing the location of the Laser Doppler Vibrometry (LDV) laser spot.	76
5.28	Experimental validation for the proposed technique. Experimental measurements are shown as black circles, and the model prediction line is shown as a solid blue line.	77
5.29	Experimental setup using the Agilent E5061B VNA.	80
5.30	Measurement calibration stages for the vector network analyzer.	81
5.31	RLC equivalent circuit for the IDT BG resonator and the VNA cable.	83
6.1	Comparison of the ideal voltage distribution, generated by the geometric shape of the IDT, and the empirical function $V(x, y)$ used to represent it.	91
6.2	FEA model geometry showing the PZT4 box, and a 2D metal surface with the IDT shape.	92
6.3	FEM predicted potential and displacement field distributions under 100 V applied across the IDT electrodes. (a) Electric potential and (b) displacement field distribution.	93

6.4	Convergence plots showing the peak-to-peak displacement $u_{z(pp)}$ as a function of electrode voltage V_o for PZT4 with air as the medium-under-test: linear static response (red), nonlinear static response using 2 modes (black), 3 modes (green), and 4 modes (blue).	94
6.5	The peak-to-peak displacement $u_{z(pp)}$ as a function of electrode voltage V_o for a PZT4 sensor with the medium-under-test set as air (green), deionized water (blue), and with a metallized surface (black). The linear solution (red) is shown for reference.	95
6.6	The peak-to-peak displacement $u_{z(pp)}$ as a function of electrode voltage V_o for the PZT4 sensor with deionized water as a medium-under-test. Stable equilibria are shown as solid black lines, and unstable equilibria are shown as dashed red lines.	97
6.7	The eigenvalues of the equilibria appearing along the lower branch in the voltage range $[0, 85]$ V for a PZT4 sensor with deionized water as the medium-under-test.	98
6.8	The peak-to-peak displacement $u_{z(pp)}$ as a function of electrode voltage V_o for the PZT4 sensor with air as a medium-under-test. Stable equilibria are shown as solid black lines, and unstable equilibria are shown as dashed red lines.	99
6.9	The eigenvalues of the equilibria along the primary branch of the PZT4 sensor for an air sample and the voltage range $[0, 92]$ V. Arrows indicate the direction of increasing voltage.	100
6.10	Eigenvalues of all equilibria of a PZT4 sensor for an air sample.	101
6.11	A prototype of the fabricated PZT4 sensor, prior to laser patterning.	102
6.12	Comparison of experimentally measured peak-to-peak displacement of the PZT4 sensor in air (gray line) as a function of DC voltage V_o to those predicted by linear (blue line) and nonlinear models (black and red dashed lines). The error bars show the standard deviation.	103

6.13	The sensor before (a) and after (b) breakdown.	103
7.1	The time evolution of the potential field $\psi(0, 0, t)$ for the PZT4 (red line) and LiNbO ₃ (black line) resonators under a pure AC excitation of $1 V_{pp}$ at the excitation frequencies $\Omega = 64.8$ MHz and 21.4 MHz, respectively.	112
7.2	The time evolution of the shear displacement field $u_z(0, 0, t)$ for the PZT4 (red line) and LiNbO ₃ (black line) resonators under a pure AC excitation of $1 V_{pp}$ at the frequencies $\Omega = 64.8$ MHz and 21.4 MHz, respectively.	113
7.3	The frequency-response curves of the shear displacement field u_z at the origin $(0, 0)$ of the PZT4 sensor under a voltage waveform with an amplitude of $V_{AC} = 0.5$ V for three media-under-test.	115
7.4	The frequency-response curves of the potential field ψ at the origin $(0, 0)$ of the PZT4 sensor under a voltage waveform with an amplitude of $V_{AC} = 0.5$ V for three media-under-test.	116
7.5	The frequency-response curves of the shear displacement field u_z at the origin $(0, 0)$ of the LiNbO ₃ sensor under a voltage waveform with an amplitude of $V_{AC} = 0.5$ V for three media-under-test.	117
7.6	The frequency-response curves of the potential field ψ at the origin $(0, 0)$ of the LiNbO ₃ sensor under a voltage waveform with an amplitude of $V_{AC} = 0.5$ V for three media-under-test.	118
7.7	The frequency-response curves of the shear displacement field u_z at the origin $(0, 0)$ of the PZT4 sensor in the vicinity of the second mode natural frequency ω_2 for three media-under-test. The sensor is excited with an unbiased voltage waveform (solid lines) and a waveform biased with $V_{DC} = 40$ V (dashed lines). The AC amplitude for both waveforms is $V_{AC} = 0.5$ V.	119

7.8	The frequency-response curves of the potential field ψ at the origin $(0, 0)$ of the PZT4 sensor in the vicinity of the second mode natural frequency ω_2 for three media-under-test. The sensor is excited with an unbiased voltage waveform (solid lines) and a waveform biased with $V_{DC} = 40$ V (dashed lines). The AC amplitude for both waveforms is $V_{AC} = 0.5$ V.	120
7.9	Modeled S-parameters based on the RLC equivalent circuit for the LiNbO ₃ sensor. The model includes parasitic capacitors for the different media-under-test.	122
7.10	Experimental S_{11} measurements for the PZT4 sensor in air.	123
7.11	Experimental S_{11} measurements for the PZT4 sensor for different media-under-test.	124
7.12	Experimental S_{11} measurements for the LiNbO ₃ sensor for different media-under-test.	125
7.13	Probing of the LiNbO ₃ sensor, with a DI water droplet covering its surface.	126

List of Tables

1.1	Permittivity sensors in the literature	7
5.1	Laser trimmer settings used and the corresponding depths etched.	64
6.1	Coefficients of the empirical fit for the spatial voltage distribution.	90
7.1	Specification of the fabricated prototypes.	120
7.2	Statistical results of the experimental measurements of the resonances for the LiNbO ₃ based sensor for different media-under-test.	124
7.3	Comparison of theoretical with experimental natural frequencies for the LiNbO ₃ sensor under different media-under-test.	125
A.1	Properties of different material considered for the permittivity sensor substrate. .	150

Nomenclature

Functions, variables, and operators

T	Stress tensor
S	Strain tensor
u	Displacement vector
$u_z(x, y, t)$	Shear displacement in the z-direction
E	Electric field vector
$E_x(x, y, t)$	Electrical field in the x-direction
$E_y(x, y, t)$	Electrical field in the y-direction
D	Electric displacement vector
$D_x(x, y, t)$	Electrical displacement in the x-direction
$D_y(x, y, t)$	Electrical displacement in the y-direction
H	Magnetic field vector
$H_z(x, y, t)$	Magnetic field in the z-direction
$\psi(x, y, t)$	Electric potential
$w(x, y, z, t)$	Out-of-plane surface deformation
$\phi_n(x, y)$	The n^{th} mode shape
q_{si}	The i^{th} modal coordinate of the static displacement

p_{si}	The i^{th} modal coordinate of the static potential
$q_i(t)$	The i^{th} modal coordinate of the dynamic displacement
$p_i(t)$	The i^{th} modal coordinate of the dynamic potential
$\zeta(x, y)$	Charge density distribution
$V(x, y)$	Applied voltage distribution
L_1, L_2	Nonlinear differential operators

Constants and parameters

l	Resonator length
λ	Wavelength
H	Substrate thickness
C	Stiffness tensor
G	Shear stiffness
ν	Poisson's ratio
e	Zero-strain piezoelectric tensor
e	Zero-strain shear piezoelectric constant
d	Zero-stress piezoelectric tensor
d	Zero-stress shear piezoelectric constant
M	Electrostrictive tensor
M	Shear electrostrictive constant
ρ	Substrate density
μ	Permeability
ϵ	Zero-strain permittivity of the substrate

ϵ_T	Zero-stress permittivity of the substrate
ϵ^u	Permittivity of the medium-under-test
r	Ratio of ϵ to ϵ^u
ι	Surface metalization constant, such as $\epsilon^u = \iota \epsilon_{ideal}^u$
c_s	Modified speed of sound in the substrate
c_l	Speed of light in the substrate
c_l^u	Speed of light in the medium-under-test
$\omega_1 \& \beta$	Natural frequency of the first mode shape
ω_n	Natural frequency of the n^{th} mode shape
Ω	Excitation frequency
k_x	The first mode wavenumber in the x-direction
k_n	The the n^{th} mode wavenumber in the x-direction
κ_u	Decay constant of the displacement field in the y-direction inside the substrate
κ_h	Decay constant of the magnetic field in the y-direction inside the substrate
κ_h^u	Decay constant of the magnetic field in the y-direction into the medium-under-test
κ_n	Decay constant of the displacement field in the y-direction inside the substrate for the n^{th} mode
η	The ratio of κ_h to k_x
ζ	The ratio of κ_u to k_x
v	BG wave speed
m	Number of IDT fingers
n	Mode number
N	Number of modes

K_{15}^2	Shear coupling coefficient
S_{11}	Reflection coefficient of port one
Z_{11}	Input impedance of port one
Z_o	The characteristic impedance of a cable
Z_c	Parasitic impedance of the sensor
c_p	Parasitic capacitance of the sensor
Q	Quality factor
σ	Substrate conductivity

Abbreviations

MEMS	Micro-Electro-Mechanical System
SAW	Surface Acoustic Waves
SH	Shear Horizontal
BG	Bleustein Gulyaev
IDT	Inter-Digitated Transducer
TM	Transverse-Magnetic
PZT4	Lead Zirconate Titanate (Navy Type I)
LiNbO_3	Lithium Niobate
PR	Photoresist
LDV	Laser Doppler Vibrometer
FEA(M)	Finite Element Analysis (Model)
RF	Radio Frequency
VNA	Vector Network Analyzer
DI water	De-Ionized water

SNR	Signal to Noise Ratio
SEM	Scanning Electron Microscopy

Chapter 1

Introduction

1.1 Piezoelectricity

Dielectric crystals, in general, are classified into either centrosymmetric or non-centrosymmetric groups, and piezoelectricity is a property of the latter. Only 20 out of the 32 crystallographic classes are piezoelectric. The absence of a center of symmetry is necessary for the appearance of piezoelectricity, however, it is not sufficient. One of the non-centrosymmetric classes (class-432) is not piezoelectric because the piezoelectric charges developed cancel each other [4]. The relationships between the piezoelectric induced strain (S) and the applied electric field (E), and between the electric displacement (D) and the stress (T) can be written as:

$$S_{ij} = d_{kij}E_k \quad (1.1)$$

$$D_k = d_{kij}T_{ij} \quad (1.2)$$

where d is the zero-stress piezoelectric constant.

Furthermore, some piezoelectric dielectrics are ferroelectric. Ferroelectric materials are de-

defined as piezoelectrics that exhibit spontaneous polarization. When such materials are exposed to an external electric field, the domains start to orient themselves, and an internal spontaneous polarization is created even after the external field is turned off. This creates a phenomenon called hysteresis [4]. This property allows for poling, where high electric fields are applied, usually with heat and the result is a remnant polarization.

The direction of poling affects the kind of Surface Acoustic Waves (SAW) that the piezoelectric substrate will support. A shear poled piezoelectric means that the direction of the poling electric field is parallel to the surface of the crystal that will support the wave.

1.2 Bleustein-Gulyaev Waves

Bleustein-Gulyaev Waves (BG waves) were discovered independently by Bleustein [5], and Gulyaev [6]. Since then, they have been under research for their unique nature; coupled electromagnetic and mechanical components that propagate together. The surface shear wave is coupled to a transverse magnetic, TM, electromagnetic field on the surface of shear poled piezoelectrics.

The direction of propagation of BG waves is orthogonal to the poling direction and parallel to the surface itself [7]. This will be further explained in detail in Section 2.1 both mathematically and graphically. More details on ferroelectricity and other nonlinearities will be discussed in Section 3.1.

Excitation

Excitation of BG waves is usually achieved through inter-digitated transducers (IDT). They are widely used to excite and detect various types of SAWs [8]. They are an array of thin metallic electrodes on the surface of a piezoelectric substrate.

Figure 1.1 shows a top view for an IDT array used to excite SAWs, such as BG waves. The electrodes consist of two interlocking sets of electrodes (fingers), where each set is comb-shaped. The structure is periodic, and the period is used to define the wavelength of the excited/detected SAW. The overlap of the fingers defines the aperture of the wave.

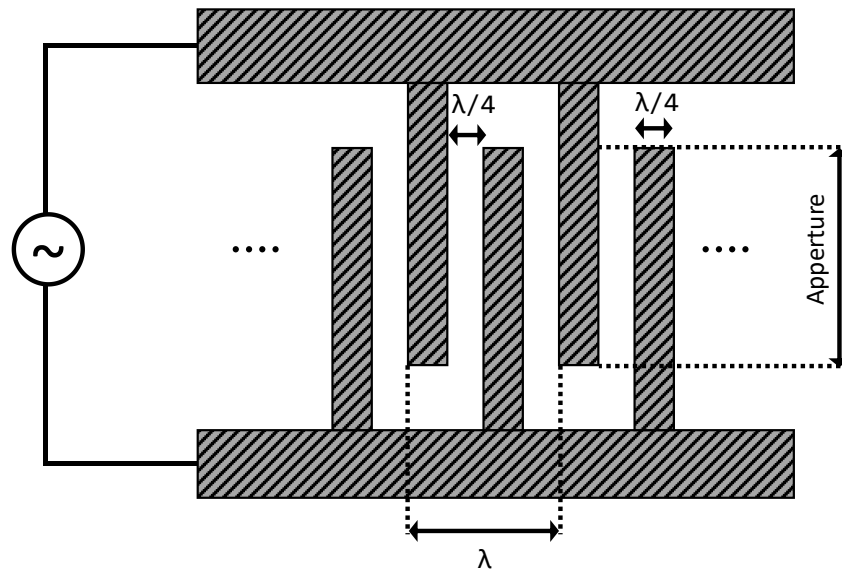


Figure 1.1: Standard IDT geometry used to excite SAW

An IDT converts the applied voltage difference into mechanical SAW vibrations and vice versa. The transduction efficiency depends on the IDT shape and the electromechanical coupling coefficient of the substrate to the specific SAW. Several IDT designs try to enhance the coupling efficiency, directionality, or the bandwidth of generated/detected SAW [9].

Applications

BG waves have been mainly used in two applications; liquid property sensing and radio frequency filters. They are attractive for liquid sensing as they do not radiate (dissipate) acoustic

energy into the liquid bulk and, thus, they avoid micro-streaming effects and realize a high-quality factor. The viscosity and density of the liquid slow down wave propagation speed and thus create a detectable phase difference with respect to a reference wave [10, 11, 12, 13]. BG waves offer sensitive liquid sensors capable of operating at various pressures and temperatures [14] and thus have wide applications. These sensors were also shown to work for conductive [15, 16] and viscoelastic [17, 18] fluids.

The second most common BG waves application is RF filters. These require trapping of the surface waves into a standing mode to create spectral selectivity. BG wave filters can be realized in more compact designs than regular SAW filters [19, 20] since they reflect completely at the edges of the piezoelectric material, eliminating the need for the cascaded electrodes that typical SAW filters use to reflect waves [21]. These filters can operate up to frequencies of 190 MHz and with a low insertion loss [22].

Successful commercial implementation of BG wave filters in television tuners has been achieved [23]. One advantage of using BG waves filters is that the quality factor is in the few hundreds [20], an advantage that is surpassed by micro-electromechanical systems (MEMS) based resonators [24]. However, MEMS resonators usually suffer from high insertion losses due to the mismatch between the low impedance transmission lines and the high impedance MEMS capacitive-based devices, while BG wave filters have a low insertion loss.

Several other attempts to employ BG waves in applications are also mentioned in the literature. One application for BG waves exploits their sensitivity to rotation by building surface wave-based gyroscopes. This was investigated mathematically [25, 26, 27, 28, 29], reporting a dynamic range of up to $\pm 150^\circ/s$ [30]. Another, Ivanov [31], suggests the use of BG waves simultaneously with other types of acoustic waves to sense the mass of bio-materials forming on a surface and thus measure bacterial growth, reporting mass sensitivity on the order of 1 pico-gram per square centimeter.

Although the theory behind BG waves was based on the piezoelectric properties, which is by definition a linear phenomenon, several factors can alter the linearity of the wave. For instance, prestress can affect the linearity of the wave [32, 33, 34, 35]. Moreover, the effect of interface imperfections [36], and amplification by semiconductors or exposure to light for photo-conducting crystals [37, 38, 39] were reported. However, other sources of nonlinearities exist, like electrostriction which is the source of nonlinearity in piezoelectric ceramics. Such effects have not been properly modeled and investigated. Indeed, some work was done to study nonlinear BG waves [40], however, they have merely brushed the subject, only proving that such nonlinearities are mathematically possible.

1.3 Permittivity Sensors

The dielectric constant is defined as the relative permittivity of the material. It is the ratio of the permittivity of the material to that of free space and thus is dimensionless. Permittivity in Maxwell's equations, along with other constants, defines the propagation constant of the electromagnetic wave. In materials, it represents the capability to permit electric field lines, and thus it characterizes the relationship between the electric displacement and the electric field [41]. The value of free space permittivity is 8.854×10^{-12} F/m. Together with the magnetic permeability of free space, these two constants define the speed of light and causality itself.

Permittivity sensors are widely used in industrial, environmental, and biological applications. Industrial applications include soil testing [42] for levels of moisture underground, oil characterization [43, 44] for testing of oil wells, and several pharmaceutical applications [45]. Environmental applications like regular and seawater salinity testing are reported [46], as well as for studying microwave radiation emitted by the ocean surface [47].

Biological applications of permittivity sensors were also reported, like DNA [48] and cell

type [49, 50, 51] discrimination. For DNA, the electric permittivity was used to distinguish single from double strands [48]. Cancer cell identification [52, 53] can also be performed by inspecting fine differences in the dielectric constant, which allows for rapid, cheap, and reliable cancer testing. Since the blood contains several electrolytes, any change of concentration would create a shift in the effective permittivity. This was reported to be used in blood analysis [54], noninvasive glucose detection [55], and blood alcohol content (ethanol) measurement [50, 56]. It has also been suggested that different viral pathogens have unique dielectric properties [57, 58], and thus a permittivity sensor can be developed towards the detection of viruses.

Current implementations are typically RF devices working beyond the GHz range. This allows for the wavelengths to be in the order of millimeters and thus permits relatively compact sensor size [49, 59, 60]. Using metamaterials, one group [61] managed to work in the THz range in order to reach micrometer dimensions. However, the use of high-frequency signals introduces additional complexity to the sensor, including specialized RF circuits. This introduces design challenges that are reflected in cost, reliability, and overall device size. Indeed, using current technology and operating at lower frequencies inflates the sensor size beyond a centimeter in length [62]. One group, [63], report sub millimeter dimensions using relatively low operating frequencies, through clever yet complex RF circuit design that exploits the higher harmonics of the sensor.

A summary of permittivity sensors available in the literature, their principle of operation, operating frequency, and dimensions is shown in Table 1.1. The table shows that current technology results in sensors that typically operate in GHz range and measure in the millimeter to centimeter size. The only exceptions are sensors that have tried to reduce size by increasing the operating frequency to the THz range or using higher order modes.

Table 1.1: Permittivity sensors in the literature

Sensor	Frequency	Size	Notes
CMOS microwave cavity [64]	10 GHz	0.9 mm	
CMOS microwave cavity [65]	0.62–10 GHz	1.4 mm	
CMOS microwave cavity [66]	0.7–6 GHz	~1.1 mm	
CMOS microwave cavity [63]	0.1–10 GHz	100 μ m	Higher modes
Microwave cavity [67]	0.6 GHz	~ 1 cm	
Split-ring resonator [68]	2 GHz	1 cm	Metamaterials
Split-ring resonator [69]	0.2–1.6 THz	36 μ m	Metamaterials
Split-ring resonator [70]	2.5 GHz	1 cm	
Split-ring resonator [71]	2.6–2.9 GHz	3 cm	
Split-ring resonator [72]	2.4 GHz	1 cm	Planar circular design
Split-ring resonator [60]	5.8–7.9 GHz	6–11 mm	
Open-ended waveguide [42]	4–6 GHz	10 cm	
Open-ended waveguide [73]	0.2–20 GHz	3.6 mm	
Open-ended waveguide [74]	0.01–1.8 GHz	4 cm	
Open-ended waveguide [75]	1–8 GHz	11 mm	
Microstrip planar resonator [76]	2 GHz	13 mm	
Microstrip resonant cell [62]	0.17–0.29 GHz	2.3 mm	
Microstrip resonant cell [59]	5 GHz	7-9 mm	
Ultrannarrow waveguide [77]	1–2 GHz	12.7 cm	
Coplanar waveguide [49]	125 GHz	1.1 mm	

Coplanar waveguide [78]	3 GHz	20 cm	
Metamaterial waveguide [61]	50 THz	$\sim 10 \mu\text{m}$	
Interdigitated capacitor [79]	20 GHz	1.3 mm	
Interdigitated capacitor* [80]	Static-50 kHz	7.5 cm	Low sensitivity due to parasitics
Interdigitated capacitor* [81]	Static-50 Hz	7 mm	Low sensitivity due to parasitics
Radio-Frequency Identifier (RFID) [82]	4 GHz	3.6 cm	
Radio-Frequency Identifier (RFID) [83]	3 GHz	5 mm	

We note that all of these sensors use a dynamic detection mode, they measure the frequency shift of an electromagnetic resonator due to the presence of the media-under-test, except for the two sensors marked with an asterisk. Those sensors use a static detection mode, measuring the change in the sensor capacitance due to the presence of the media-under-test.

1.4 Problem Statement and Objectives

The use of BG waves in sensing is promising, as the shear wave is sensitive to any discontinuity in properties at the surface. One major advantage is that the wave is localized at the surface, which maximizes the efficiency in using it to detect target properties at that surface. Indeed, there have been many successful attempts at detecting mechanical properties, like viscosity and density, using BG waves [10, 11, 14, 15]. However, the wave is part mechanical and

part electromagnetic, and few attempts have been made to exploit the latter, with none in sensing applications. Amplification of BG waves using a semiconductor close to the surface is one example [39]. However, since the wave has an electric field component, the potential remains of acoustically sensing an electrical property, such as the electric permittivity.

Another issue found in the literature is that researchers seem to shy away from nonlinearities such as electrostriction when performing the analysis for BG waves. Some attempts investigated the effect of biasing or prestressing the piezoelectric material [34, 84, 85], but without allocating proper explanations and without the utilization of nonlinearities to allow the application of the phenomenon in a useful manner.

Additionally, as discussed, current limitations of permittivity sensors can be summed as a trade-off between device size and the attendant complexity of RF devices. Devices operating below the GHz range have sensors that are few centimeters wide [44, 62]. For compact designs, the frequency of operation would have to be driven beyond 100 GHz, which requires specialized RF circuits. Another major issue with operating in the GHz range is observed when working with aqueous-based samples. This is due to the relaxation phenomenon of water at frequencies beyond 4 GHz [54]. Indeed, working in the RF range prohibits the measurement of the DC permittivity of aqueous media. Alternatively, slowing down the phase velocities of electromagnetic waves has been suggested to permit the design of compact and sensitive permittivity sensors [86].

In this work, a novel sensor based on BG waves that operates in the MHz range is presented. BG waves couple electromagnetic and acoustic waves, thereby reducing the speed of electromagnetic propagation to near acoustic wave speeds. Therefore the BG wave permittivity sensor feature several orders of magnitude reduction in both size and operating frequency. This allows the development of compact sensors with micrometer wavelengths which breaks the limitations of RF complexity and drops the cost considerably.

Furthermore, we propose to exploit a nonlinearity that arises under high bias fields due to electrostriction. This lowers the effective linearized permittivity of the piezoelectric substrate, as seen by the wave. This promises to tune and match the effective piezoelectric permittivity to enhance the sensitivity of the wave to the permittivity of the medium placed on the BG waves surface. Indeed, several important biological and industrial properties can affect the dielectric constant and, thus, the sensor could provide a cheap and accurate water salinity sensor or bio-detector.

Moreover, the reported method for building a compact filter [21] into constructing the sensor is implemented, ensuring that both size and cost are kept at a minimum. Additionally, this work presents a first-of-a-kind approach to probe an electric property acoustically using BG waves.

Towards that end, the first objective of this work is to solve the BG wave equations under the resonant boundary conditions in Chapter 2. The next objective is to analyze the nonlinearities in BG waves and then investigate the possibility of the linearization of parameters around a bias point, Chapter 3. Then, the eigenvalue analysis is carried out in Chapter 4, and the sensor prototypes are proposed accordingly in Chapter 5. The fabrication process and the experimental setups and techniques are also discussed in Chapter 5.

The following objective is the examination of the response of the BG wave to forced non-resonant and static excitation. The effect of different kinds of damping in the system and the method of wave excitation are also studied. This analysis is in Chapter 6, and it allows for the expansion of the dynamic solution around the equilibrium solution, in the following chapter.

Lastly, the full dynamic linear and nonlinear solutions, as well as the experimental validation, of the permittivity sensor are detailed in Chapter 7. In Chapter 8, the thesis is concluded, and the suggested future work is outlined.

Chapter 2

BG Resonator

In this chapter, the basic model of the BG-wave-based sensor will be discussed. Specifically, the undamped and unforced linear sensor model. The constitutive and governing equations, as well as the boundary conditions, will be explained. The traditional homogeneous solution [5, 6] of the wave, subject to boundary conditions set by the edge reflectors, will be formulated. Finally, the quasi-static approximation will be discussed, and the system is nondimensionalized.

2.1 BG Wave Equations

The problem of the BG wave is described in two half-spaces, one containing the piezoelectric and the other encompassing the space above it. Maxwell's equations hold for both half-spaces, but the lower one is also governed by piezoelectric relationships.

2.1.1 Field Definitions

The BG wave has a displacement field (\mathbf{u}) coupled to a transversely magnetic (TM) electromagnetic field (\mathbf{E} and \mathbf{H}), defined as [5, 6, 10, 87, 88]:

$$\mathbf{u}(x, y, t) = \begin{pmatrix} 0 \\ 0 \\ u_z \end{pmatrix}, \quad \mathbf{E}(x, y, t) = \begin{pmatrix} E_x \\ E_y \\ 0 \end{pmatrix}, \quad \mathbf{H}(x, y, t) = \begin{pmatrix} 0 \\ 0 \\ H_z \end{pmatrix} \quad (2.1)$$

where x and z are the propagation and poling directions, respectively. This definition of the displacement field results in a strain field (\mathbf{S}) that can be written in Voigt notation, such as:

$$\mathbf{S}(x, y, t) = \begin{pmatrix} 0 \\ 0 \\ 0 \\ \partial u_z / \partial y \\ \partial u_z / \partial x \\ 0 \end{pmatrix} \quad (2.2)$$

2.1.2 Constitutive Equations

Figure 2.1 shows the piezoelectric substrate, the medium-under-test, the axes, and poling direction. The wave synchronously propagates in the x -direction along the surface of a piezoelectric substrate. A thin metallic IDT is patterned on the surface of the substrate to excite the wave. At $x = 0$ and $x = l$, two trenches are etched to acoustically reflect the wave, thereby creating a resonator, where l is the total length of the resonator.

The positive direction of the y -axis is chosen to point into the more interesting (piezoelectric) half-space. The medium-under-test is deposited on top of the sensor in the upper half-space.

The only non-trivial elements of the relevant stress and polarization tensors in the piezoelec-

tric material ($y > 0$) are [5]:

$$T_{yz} = G \frac{\partial u_z}{\partial y} - e E_y \quad (2.3)$$

$$T_{xz} = G \frac{\partial u_z}{\partial x} - e E_x \quad (2.4)$$

$$D_x = \epsilon E_x + e \frac{\partial u_z}{\partial x} \quad (2.5)$$

$$D_y = \epsilon E_y + e \frac{\partial u_z}{\partial y} \quad (2.6)$$

where $\epsilon = \epsilon_{xx}$ is the zero-strain permittivity of the piezoelectric, $G = c_{44}$ is the shear modulus of the piezoelectric, and $e = e_{15} = c_{44} d_{15}$ is the zero-strain shear piezoelectric constant.

In the medium-under-test ($y < 0$), the polarization tensors can be written, such as:

$$D_x^u = \epsilon^u E_x^u \quad (2.7)$$

$$D_y^u = \epsilon^u E_y^u \quad (2.8)$$

where ϵ^u is the permittivity of the medium-under-test and the superscript u denotes the field and properties of the medium-under-test in the upper half-space ($y < 0$).

2.1.3 Governing Equations

The acoustic equation of motion for the displacement field for a unit volume is given by [88]:

$$\nabla \cdot \mathbf{T} = \rho \ddot{u}_z \quad (2.9)$$

where ρ is the density of the piezoelectric material. Moreover, Maxwell's equations state that the divergence of the electric displacement field \mathbf{D} vanishes in a volume with no net charge

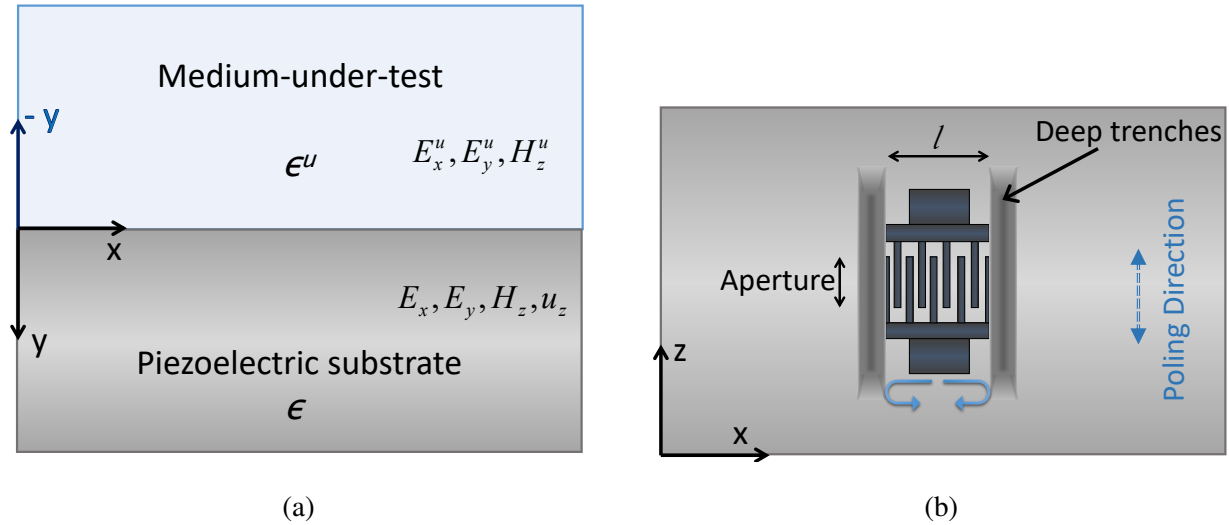


Figure 2.1: Sensor schematic showing the substrate, medium-under-test, and the IDT design. The front section view is shown in (a) and the top view in (b).

(unforced). They also relates the electric \mathbf{E} and magnetic \mathbf{H} fields. This can be written such as:

$$\nabla \cdot \mathbf{D} = 0 \tag{2.10}$$

$$\nabla \times \mathbf{E} = -\mu \dot{\mathbf{H}} \tag{2.11}$$

$$\nabla \times \mathbf{H} = \dot{\mathbf{D}} \tag{2.12}$$

where μ is the magnetic permeability of the piezoelectric material.

2.1.4 Boundary Conditions

BG waves are surface waves and, thus, they decay along the y-axis into the substrate, within a few wavelengths [5, 6]. Therefore, the field equations are solved subject to boundary conditions

specifying that the surface wave vanishes at the far-side of the lower-half space, such as:

$$u_z \Big|_{y=\infty} = 0, \quad H_z \Big|_{y=\infty} = 0 \quad (2.13)$$

$$E_x \Big|_{y=\infty} = 0, \quad E_y \Big|_{y=\infty} = 0 \quad (2.14)$$

as well as for the upper-half space:

$$H_z^u \Big|_{y=-\infty} = 0, \quad E_x^u \Big|_{y=-\infty} = 0, \quad E_y^u \Big|_{y=-\infty} = 0 \quad (2.15)$$

The air created by the trenches beyond the edges of the IDT offers a lower acoustic impedance to the propagation of the wave than the piezoelectric substrate. Therefore, the resonator edges represent free-end conditions, ideally with perfect acoustic reflection and no phase shift. This can be formulated as:

$$\frac{\partial u_z}{\partial x} \Big|_{x=0} = 0, \quad \frac{\partial u_z}{\partial x} \Big|_{x=l} = 0 \quad (2.16)$$

Further, assuming that there are no mechanical loads applied to the piezoelectric (interface) surface, we set the shear component $T_{yz} = 0$, which yields:

$$G \frac{\partial u_z}{\partial y} \Big|_{y=0} - e E_y \Big|_{y=0} = 0 \quad (2.17)$$

Additionally, the continuity of the electromagnetic field necessitates the matching of its components at the interface between the piezoelectric substrate and the medium-under-test, at ($y = 0$).

This can be written as:

$$E_x \Big|_{y=0} = E_x^u \Big|_{y=0} \quad (2.18)$$

$$H_z \Big|_{y=0} = H_z^u \Big|_{y=0} \quad (2.19)$$

$$D_y \Big|_{y=0} = D_y^u \Big|_{y=0} \quad (2.20)$$

where $D_y^u = \epsilon^u E_y^u = \frac{\epsilon}{r} E_y^u$ and $r = \frac{\epsilon}{\epsilon^u}$ is the ratio of the permittivity of the substrate to that of the piezoelectric medium-under-test. Using the constitutive equations (2.6) and (2.8), equation (2.20) can be rewritten such as:

$$r\epsilon E_y \Big|_{y=0} + re \frac{\partial u_z}{\partial y} \Big|_{y=0} = \epsilon E_y^u \Big|_{y=0} \quad (2.21)$$

2.2 Solution of the Homogeneous Equations

The acoustic equation of motion (2.9) and the electric displacement divergence equation (2.10) can both be rewritten after substituting with the constitutive equations (2.3) to (2.6), such as:

$$G \left(\frac{\partial^2 u_z}{\partial x^2} + \frac{\partial^2 u_z}{\partial y^2} \right) - e \left(\frac{\partial E_x}{\partial x} + \frac{\partial E_y}{\partial y} \right) = \rho \ddot{u}_z \quad (2.22)$$

$$e \left(\frac{\partial^2 u_z}{\partial x^2} + \frac{\partial^2 u_z}{\partial y^2} \right) + \epsilon \left(\frac{\partial E_x}{\partial x} + \frac{\partial E_y}{\partial y} \right) = 0 \quad (2.23)$$

These equations can be simplified by rewriting them to eliminate the electric field, such as:

$$\begin{aligned} \rho \ddot{u}_z &= \left(G + \frac{e^2}{\epsilon} \right) \left(\frac{\partial^2 u_z}{\partial x^2} + \frac{\partial^2 u_z}{\partial y^2} \right) \\ \ddot{u}_z &= c_s^2 \nabla^2 u_z \end{aligned} \quad (2.24)$$

where $c_s = \sqrt{\frac{(G + \frac{e^2}{\epsilon})}{\rho}}$ is the acoustic speed of the wave. It is important to note that this speed is not the speed of the BG wave, but rather the speed of a shear acoustic wave, has it existed independently and uncoupled.

Similarly, equations (2.11) and (2.12) can be also written as:

$$\mu \dot{H}_z = \frac{\partial E_x}{\partial y} - \frac{\partial E_y}{\partial x} \quad (2.25)$$

$$\frac{\partial H_z}{\partial y} = e \frac{\partial \dot{u}_z}{\partial x} + \epsilon \dot{E}_x \quad (2.26)$$

$$\frac{\partial H_z}{\partial x} = -e \frac{\partial \dot{u}_z}{\partial y} - \epsilon \dot{E}_y$$

Differentiating equation (2.25) with respect to time and substituting in the result for the electric field with (2.26), we obtain:

$$\begin{aligned} \epsilon \mu \ddot{H}_z &= \frac{\partial^2 H_z}{\partial x^2} + \frac{\partial^2 H_z}{\partial y^2} \\ \ddot{H}_z &= c_l^2 \nabla^2 H_z \end{aligned} \quad (2.27)$$

where $c_l = \sqrt{\frac{1}{\epsilon \mu}}$ is the speed of light in the piezoelectric.

Since no solid deformation exists in the upper-half space, we only have Maxwell's equations for the electric and magnetic fields in the medium, such as:

$$\mu \epsilon^u \ddot{H}_z^u = \frac{\partial^2 H_z^u}{\partial x^2} + \frac{\partial^2 H_z^u}{\partial y^2} \quad (2.28)$$

$$\frac{\partial H_z^u}{\partial y} = \epsilon^u \dot{E}_x^u \quad (2.29)$$

$$\frac{\partial H_z^u}{\partial x} = \epsilon^u \dot{E}_y^u$$

The solution describing the fields in the lower half-space ($y > 0$) can be obtained as follows: Equations (2.24), and (2.27) can be solved for the displacement and magnetic fields, respectively. Then, the electric field is obtained by substituting the solution into equation (2.26).

First, we assume a solution in the form [5, 6]:

$$u_z = X(x)Y(y)T(t) \quad (2.30)$$

and substitute it into equation (2.24), to obtain:

$$c_s^2(X''YT + XY''T) = XY\ddot{T}$$

where the primes stand for spatial derivatives and the overdots stand for time derivatives. Dividing both sides of the equation by $XYTc_s^2$ yields:

$$\frac{X''}{X} + \frac{Y''}{Y} = \frac{\ddot{T}}{c_s^2 T} = -\left(\frac{\beta}{c_s}\right)^2$$

where β is the natural frequency of the mode shape. This equation can be solved as a set of two equations describing variations in space and time. For the time variation, we write:

$$\ddot{T} + \beta^2 T = 0$$

The solution of this equation is:

$$T = a_1(e^{i(\beta t + \theta_0)} + e^{-i(\beta t + \theta_0)}) \quad (2.31)$$

where a_1 and θ_0 are real constants obtained by satisfying the initial conditions. Assuming that the initial conditions start from rest, we set the phase angle equal to zero $\theta_0 = 0$.

For the spatial variation, we can write:

$$\begin{aligned} \frac{X''}{X} + \frac{Y''}{Y} &= -\left(\frac{\beta}{c_s}\right)^2 \\ \frac{Y''}{Y} + \left(\frac{\beta}{c_s}\right)^2 &= \frac{-X''}{X} = k_x^2 \end{aligned}$$

where k_x is the wavenumber. We can solve for the spacial variation along the x , and y directions separately. First, we write:

$$X'' + k_x^2 X = 0$$

The solution of this equation is:

$$X = a_2 e^{ik_x x} + \bar{a}_2 e^{-ik_x x}$$

where a_2 and k_x are complex constants obtained by satisfying the boundary conditions.

Applying the boundary conditions (2.16), at time $t = 0$, we get:

$$\begin{aligned} \left. \frac{dX}{dx} \right|_{x=0} &= ik_x(a_2 - \bar{a}_2) = 0 \quad \rightarrow \quad a_2 = \bar{a}_2 \\ \left. \frac{dX}{dx} \right|_{x=l} &= ik_x a_2 (e^{ik_x l} - e^{-ik_x l}) = 0 \quad \rightarrow \quad k_x = \frac{m\pi}{l}, \quad m = 1, 2, 3, \dots \end{aligned}$$

As a result, we can reduce the variation along the x-direction to:

$$X = a_2 e^{im\pi x} + a_2 e^{-im\pi x} = 2a_2 \cos(m\pi x) \quad (2.32)$$

where m is the spatial mode number. Setting the number of inter-digitated fingers to m can be used for selective excitation of the corresponding mode.

Similarly, the spatial variation in the y -direction is written as:

$$\frac{Y''}{Y} + \left(\frac{\beta}{c_s}\right)^2 = k_x^2$$

This can be re-written, such as:

$$Y'' - \kappa_u^2 Y = 0$$

where κ_u is the decay constant in the y -direction, given by:

$$\kappa_u^2 = k_x^2 - \left(\frac{\beta}{c_s}\right)^2 \quad (2.33)$$

Assuming that $k_x^2 > c_s^2 \beta^2$ to keep κ_u as a real number, the solution is written in the form:

$$Y = a_4 e^{-\kappa_u y} + a_5 e^{\kappa_u y}$$

Using the surface wave boundary condition (2.13), we observe that a_5 must be identically zero, therefore:

$$Y = a_4 e^{-\kappa_u y} \quad (2.34)$$

Thus, substituting equations (2.31), (2.32), and (2.34) into equation (2.30), we can write the displacement field such as [5, 6]:

$$\begin{aligned} u_z &= a_1 a_2 a_4 e^{-\kappa_u y} (e^{i\frac{m\pi}{l}x} + e^{-i\frac{m\pi}{l}x}) (e^{i\beta t} + e^{-i\beta t}) \\ &= U_o e^{-\kappa_u y} (e^{i\frac{m\pi}{l}x} + e^{-i\frac{m\pi}{l}x}) (e^{i\beta t} + e^{-i\beta t}) \end{aligned} \quad (2.35)$$

where $U_o = a_1 a_2 a_4$ is the amplitude of the displacement field.

Following a similar approach, we can solve the magnetic field equations (2.27) and (2.28) for H_z and H_z^u , respectively, and use the boundary conditions (2.13) and (2.16) to obtain [5, 6]:

$$H_z = H_o e^{-\kappa_h y} (e^{i\frac{m\pi}{l}x} + e^{-i\frac{m\pi}{l}x}) (e^{i\beta t} + e^{-i\beta t}) \quad (2.36)$$

$$H_z^u = H_o^u e^{\kappa_h^u y} (e^{i\frac{m\pi}{l}x} + e^{-i\frac{m\pi}{l}x}) (e^{i\beta t} + e^{-i\beta t}) \quad (2.37)$$

where H and H^u are the amplitudes of the magnetic fields in the piezoelectric and the medium-under-test, respectively, and

$$\kappa_h^2 = k_x^2 - \left(\frac{\beta}{c_l}\right)^2 \quad \text{and} \quad \kappa_h^{u2} = k_x^2 - \left(\frac{\beta}{c_l^u}\right)^2$$

where c_l^u is the speed of light in the medium-under-test.

Finally, the electric field is obtained by substituting the displacement and magnetic fields (2.35)–(2.37) into equations (2.26), and integrating over time. The solution is, thus, obtained such as

[5, 6]:

$$E_x = i \frac{H_o \kappa_h}{\epsilon \beta} e^{-\kappa_h y} (e^{i \frac{m\pi}{l} x} + e^{-i \frac{m\pi}{l} x}) (e^{i\beta t} - e^{-i\beta t}) - i \frac{m\pi e}{\epsilon l} U_o e^{-\kappa_u y} (e^{i \frac{m\pi}{l} x} - e^{-i \frac{m\pi}{l} x}) (e^{i\beta t} + e^{-i\beta t}) \quad (2.38)$$

$$E_y = -\frac{m\pi H_o}{\epsilon l \beta} e^{-\kappa_h y} (e^{i \frac{m\pi}{l} x} - e^{-i \frac{m\pi}{l} x}) (e^{i\beta t} - e^{-i\beta t}) + \frac{\kappa_u e}{\epsilon} U_o e^{-\kappa_u y} (e^{i \frac{m\pi}{l} x} + e^{-i \frac{m\pi}{l} x}) (e^{i\beta t} + e^{-i\beta t}) \quad (2.39)$$

$$E_x^u = -i \frac{\kappa_h^u r H_o^u}{\epsilon \beta} e^{\kappa_h^u y} (e^{i \frac{m\pi}{l} x} + e^{-i \frac{m\pi}{l} x}) (e^{i\beta t} - e^{-i\beta t}) \quad (2.40)$$

$$E_y^u = -\frac{m\pi r H_o^u}{\epsilon l \beta} e^{\kappa_h^u y} (e^{i \frac{m\pi}{l} x} - e^{-i \frac{m\pi}{l} x}) (e^{i\beta t} - e^{-i\beta t}) \quad (2.41)$$

2.3 Quasi-static approximation

The time constant of the wave's electromagnetic component is five orders-of-magnitude smaller than its elastic counterpart. Therefore, variations in the electromagnetic component in response to the elastic component appear to happen instantaneously. This justifies the adoption of a quasi-static approximation of the electromagnetic component. We note that this approximation remains valid as long as the effective wave speed is at the order of acoustic speeds. Under this assumption, equation (2.11) can be reduced to:

$$\dot{H}_z = 0 \quad \Rightarrow \quad \frac{\partial E_y}{\partial x} - \frac{\partial E_x}{\partial y} = 0 \quad (2.42)$$

which can be satisfied by assuming a potential function ψ , such as:

$$E_x = -\frac{\partial \psi}{\partial x}, \quad E_y = -\frac{\partial \psi}{\partial y} \quad (2.43)$$

Substituting in the governing equations (2.22) and (2.23), we obtain:

$$\begin{aligned} G\left(\frac{\partial^2 u_z}{\partial x^2} + \frac{\partial^2 u_z}{\partial y^2}\right) + e\left(\frac{\partial^2 \psi}{\partial x^2} + \frac{\partial^2 \psi}{\partial y^2}\right) &= \rho \ddot{u}_z \\ e\left(\frac{\partial^2 u_z}{\partial x^2} + \frac{\partial^2 u_z}{\partial y^2}\right) - \epsilon\left(\frac{\partial^2 \psi}{\partial x^2} + \frac{\partial^2 \psi}{\partial y^2}\right) &= 0 \end{aligned}$$

which can be rewritten as:

$$G\nabla^2 u_z + e\nabla^2 \psi = \rho \ddot{u}_z \quad (2.44)$$

$$e\nabla^2 u_z - \epsilon\nabla^2 \psi = 0 \quad (2.45)$$

Substituting the potential function in the boundary conditions (2.14) to (2.20), we obtain:

$$\psi \Big|_{y=\infty} = 0, \quad \psi^u \Big|_{y=-\infty} = 0 \quad (2.46)$$

$$G \frac{\partial u_z}{\partial y} \Big|_{y=0} + e \frac{\partial \psi}{\partial y} \Big|_{y=0} = 0 \quad (2.47)$$

$$\frac{\partial \psi}{\partial x} \Big|_{y=0} - \frac{\partial \psi^u}{\partial x} \Big|_{y=0} = 0 \quad (2.48)$$

$$r\epsilon \frac{\partial \psi}{\partial y} \Big|_{y=0} - re \frac{\partial u_z}{\partial y} \Big|_{y=0} - \epsilon \frac{\partial \psi^u}{\partial y} \Big|_{y=0} = 0 \quad (2.49)$$

This system of equations is simpler to solve and will be handled in detail in upcoming chapters. However, first, the eigenvalue problem will be considered in the next chapter.

2.4 Nondimensionalization

It is useful to nondimensionalize the system of equations, to be able to solve the system numerically. It also helps understand and visualize the relevant terms in the equations. Towards

that effect, the system is rewritten as follows:

$$\begin{aligned} \hat{x} &= \frac{x}{l}, & \hat{y} &= \frac{y}{l}, & \hat{t} &= \frac{t}{\tau}, \\ \hat{\mathbf{E}} &= \frac{\mathbf{E}}{E_o}, & \hat{\mathbf{H}} &= \frac{\mathbf{H}}{h_o}, & \hat{\mathbf{u}} &= \frac{\mathbf{u}}{u_o}, \\ \hat{\mathbf{E}}^u &= \frac{\mathbf{E}^u}{E_o^u}, & \hat{\mathbf{H}}^u &= \frac{\mathbf{H}^u}{h_o^u}, & & \end{aligned}$$

where l is the device's length and u_o is the linearized ideal response to a nominal 1 Volt applied, or 1 V. Both the electric and magnetic fields are also normalized to a nominal 1 V. The time-scale τ and the nominal values u_o , E_o , h_o are defined, such as:

$$\begin{aligned} \tau &= \lambda/c_s, & c_s &= \sqrt{\frac{G + \frac{e^2}{\epsilon}}{\rho}} \\ E_o &= E_o^u = \frac{(1V)}{l} = \frac{1}{l} & h_o &= \frac{(1V)}{l} \sqrt{\frac{\epsilon}{\mu}} = \frac{1}{l} \sqrt{\frac{\epsilon}{\mu}} \\ u_o &= \frac{e}{G}(1V) = \frac{e}{G} & h_o^u &= \frac{1}{l} \sqrt{\frac{\epsilon^u}{\mu}} \end{aligned}$$

where λ is the wavelength. Dropping the hats for convenience, the non-dimensional governing equations (2.22) and (2.23) can be written as:

$$\left(\frac{\partial^2 u_z}{\partial x^2} + \frac{\partial^2 u_z}{\partial y^2} \right) - \left(\frac{\partial E_x}{\partial x} + \frac{\partial E_y}{\partial y} \right) = \alpha \ddot{u}_z \quad (2.50)$$

$$\frac{e^2}{G\epsilon} \left(\frac{\partial^2 u_z}{\partial x^2} + \frac{\partial^2 u_z}{\partial y^2} \right) + \left(\frac{\partial E_x}{\partial x} + \frac{\partial E_y}{\partial y} \right) = 0 \quad (2.51)$$

where $\alpha = \frac{l^2}{\lambda^2} \left(\frac{e^2}{G\epsilon} + 1 \right)$. Similarly, equations (2.24) and (2.27) can be written as:

$$\ddot{u}_z = \frac{\lambda^2}{l^2} \nabla^2 u_z \quad (2.52)$$

$$\ddot{H}_z = \frac{\lambda^2 \delta^2}{l^2} \nabla^2 H_z \quad (2.53)$$

where $\delta = \frac{c_l}{c_s}$. The boundary conditions in equations (2.13) to (2.16) can also be nondimensionalized, such as:

$$u_z \Big|_{y=\infty} = 0, \quad H_z \Big|_{y=\infty} = 0, \quad H_z^u \Big|_{y=-\infty} = 0 \quad (2.54)$$

$$\frac{\partial u_z}{\partial x} \Big|_{x=0} = \frac{\partial u_z}{\partial x} \Big|_{x=1} = 0 \quad (2.55)$$

$$\frac{\partial H_z}{\partial x} \Big|_{x=0} = \frac{\partial H_z}{\partial x} \Big|_{x=1} = 0 \quad (2.56)$$

Further, equations (2.17), (2.18), (2.19), and (2.21), are nondimensionalized, such as:

$$\frac{\partial u_z}{\partial y} \Big|_{y=0} - E_y \Big|_{y=0} = 0 \quad (2.57)$$

$$E_x \Big|_{y=0} - E_x^u \Big|_{y=0} = 0 \quad (2.58)$$

$$\sqrt{r} H_z \Big|_{y=0} - H_z^u \Big|_{y=0} = 0 \quad (2.59)$$

$$\left(r \frac{e^2}{G\epsilon} \frac{\partial u_z}{\partial y} \Big|_{y=0} + r E_y \Big|_{y=0} \right) = E_y^u \Big|_{y=0} \quad (2.60)$$

The quasistatic equations (2.44) and (2.45) can also be nondimensionalized, such as:

$$\nabla^2 u_z + \nabla^2 \psi = \alpha \ddot{u}_z \quad (2.61)$$

$$\nabla^2 u_z - \frac{G\epsilon}{e^2} \nabla^2 \psi = 0 \quad (2.62)$$

where the potential, ψ , is nondimensionalized such as $\hat{\psi} = \frac{\psi}{\psi_0}$ and $\psi_0 = 1$ V. The hats were dropped for convenience. Lastly, the nondimensional boundary conditions under the quasistatic

approximation are written, such as:

$$\psi \Big|_{y=\infty} = 0, \quad \psi^u \Big|_{y=-\infty} = 0 \quad (2.63)$$

$$\frac{\partial u_z}{\partial y} \Big|_{y=0} + \frac{\partial \psi}{\partial y} \Big|_{y=0} = 0 \quad (2.64)$$

$$\frac{\partial \psi}{\partial x} \Big|_{y=0} - \frac{\partial \psi^u}{\partial x} \Big|_{y=0} = 0 \quad (2.65)$$

$$r\epsilon \frac{\partial \psi}{\partial y} \Big|_{y=0} - r \frac{e^2}{G} \frac{\partial u_z}{\partial y} \Big|_{y=0} - \epsilon \frac{\partial \psi^u}{\partial y} \Big|_{y=0} = 0 \quad (2.66)$$

2.5 Summary

The BG wave is explained and the BG wave field definitions and constitutive equations are outlined. The governing under the resonant boundary conditions were formulated and the homogenous system was solved. Moreover, the quasistatic approximation was applied. Finally the system was nondimensionalized.

Chapter 3

Nonlinearity in BG Waves

Piezoelectricity is a linear phenomenon that relates stress in a material to the electric field applied across it. Strain is generated when the electric field ‘pulls’ on the polarized crystals of the material. The converse effect is also true, a stress-induced strain separates or squeezes the crystal creating a net polarization, an overall internal electric field.

Nonlinearity in piezoelectrics arises from electrostriction, which is an entirely different phenomenon. It occurs in all dielectrics, centrosymmetric or not, while piezoelectricity can only occur in non-centrosymmetric crystals. It is described by a quadratic relationship between mechanical deformation and polarization of the crystal ($S \propto E^2$). As a result, the strain direction does not flip when the electric field polarity is flipped. This behavior has occasionally been misidentified as a piezoelectric nonlinearity. Other sources of nonlinearity in piezoelectrics include hysteresis and mechanical stress-strain nonlinearities.

In this chapter, the sources of nonlinearities in BG waves are investigated and applied to the governing equations. Then the relative orders of these nonlinearities are considered, and the constitutive relationships governing the BG waves are rewritten, thereby extending the linear

equations into the nonlinear domain. Finally, the system is linearized as a first approximation to study the effect of biasing on the sensor.

3.1 Sources of Nonlinearities

The three most important sources for the deviation from linear behavior in piezoelectrics are mechanical nonlinearities, polarization hysteresis, and electrostriction. Mechanical nonlinearities are either irreversible plasticity or geometric nonlinearities. The former is undesirable as it permanently deforms the material and the latter is only significant under moderately large displacements. For this work, we are interested in surface waves where loads are kept small enough to avoid plasticity and deformations are infinitesimal.

The crystal structure of piezoelectric materials is non-centrosymmetric. The cells of those crystals possess multiple equilibria, each exhibiting a non-zero polarization. When crystal dipoles align inside grains in naturally occurring materials, they are randomly aligned. As a result, the material exhibits zero internal polarization.

Once an external electric field E is applied, grains align their polarization with the field resulting in a net internal polarization P proportional to the electric field, as shown by the red line in Figure 3.1. After the field is removed, a fraction of the crystals retains their new equilibrium and polarization, resulting in a remnant internal polarization, P_R . This is the case because, under room temperature, crystals do not possess enough energy to clear the potential barrier separating multiple equilibria. Beyond a temperature threshold, the Currie Temperature T_c , crystals have enough energy to clear that potential barrier. Above T_c , once the electric field is removed the crystals and grains regain their random orientation, and the internal polarization disappears completely. As the temperature increases towards T_c , the likelihood of a crystal receiving enough

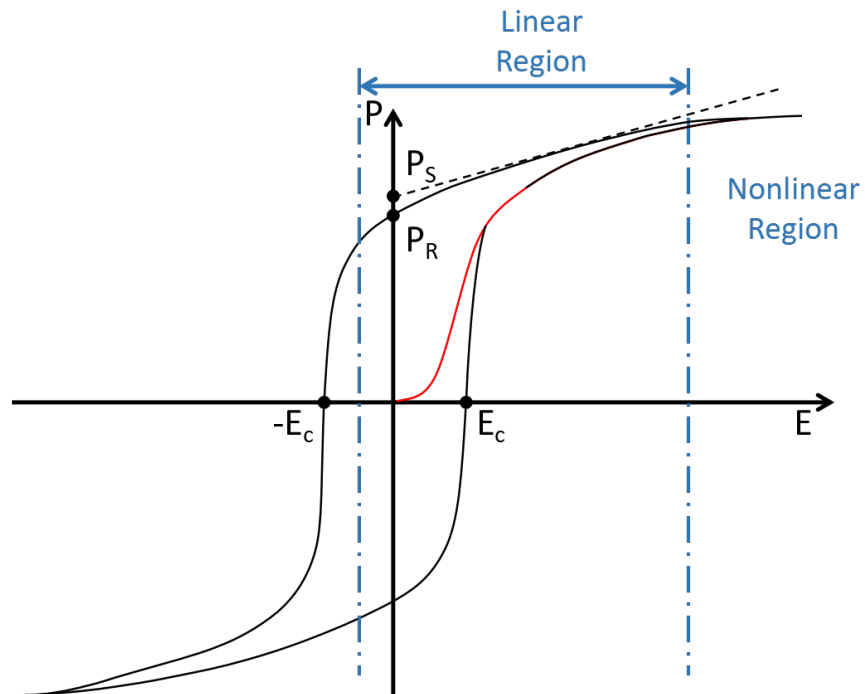


Figure 3.1: The hysteresis loop of the polarization P created under an applied external electric field E in ferroelectric materials.

energy to clear the potential barrier increases. Therefore, it is usually advised to stay below half T_c to reduce the likelihood of depolarization after prolonged operation [89].

The existence of remnant polarization is the source of hysteretic loops in ferroelectric piezoelectrics. Application of an electric field opposite to the remnant polarization can force the material to reorient its grains below T_c , as it provides the dipoles with enough energy to overcome the barriers. The value of the minimum electric field required to eliminate the internal polarization is called the coercive electric field E_c . This is, however, usually not a hard value as the application of small electric fields for an extended amount of time could reorient the domains as well. Increasing the electric field further beyond that point will polarize the material in the opposite

direction. Repetitive polarization in opposite directions creates a hysteretic loop, as shown in Figure 3.1.

Spontaneous polarization P_S is defined as the saturation polarization due to the reorientation of grains alone, under no piezoelectric effect. It is obtained by linear extrapolation, the dotted line in Figure 3.1, that assumes a linear piezoelectric effect. It differs from remnant polarization as the latter is the actual polarization at ($E = 0$) reduced by random reorientation of outlier energetic grains at room temperature.

The process of creating remnant polarization is called poling and is shown by the red line in Figure 3.1. It involves applying a strong electric field under heat to help orient the grains. Although hysteresis is a form of nonlinearity, once the material becomes poled, it can operate almost linearly within a range extending from P_S to another point close to the coercive field shown in Figure 3.1. Electric fields applied in the same direction as the poling field must remain lower than the poling value. Venturing beyond this point can create nonlinearities. Most piezoelectric actuators in the literature try to remain inside this linear region.

Electrostriction, on the other hand, is the quadratic response of strain to applied electric fields. By definition, it is a nonlinear relationship that exists in all dielectrics, including piezoelectrics, between strain and polarization. Because the polarization and the electric field are linearly related, within limited regions of the hysteretic loop, strain can be related to the electric field within such regions as follows:

$$S_{ij} = Q_{ijkl}P_kP_l = M_{ijkl}E_kE_l \quad ; \quad i, j, k, l = 1, 2, 3 \quad (3.1)$$

where Q_{ijkl} and M_{ijkl} are elements of the electrostrictive polarization and electrostrictive electric field constant tensors, respectively, and indicial notation is invoked. In subsequent sections, we limit our interest to a linear region of the hysteretic loop, thereby leaving electrostriction as the dominant source of nonlinearity.

3.1.1 Electrostriction Nonlinearity

The binomial expansion of the crystal Gibbs free Energy (PE) including all possible nonlinearities is [90]:

$$PE = \alpha_1 E^2 + \alpha_2 T^2 + \alpha_3 TE + \alpha_4 E^3 + \alpha_5 T^3 + \alpha_6 T^2 E + \alpha_7 E^2 T \\ + \alpha_8 T^4 + \alpha_9 E^4 + \alpha_{10} E^3 T + \alpha_{11} T^3 E + \alpha_{12} T^2 E^2 + \dots$$

We scale the electric field \mathbf{E} at $O(\hat{\epsilon})$ and the stress tensor \mathbf{T} at $O(\hat{\epsilon}^2)$, where $\hat{\epsilon}$ is a small bookkeeping parameter, and substitute in the energy formulation to obtain:

$$PE = \hat{\epsilon}^2 \alpha_1 E^2 + \hat{\epsilon}^4 \alpha_2 T^2 + \hat{\epsilon}^3 \alpha_3 TE + \hat{\epsilon}^3 \alpha_4 E^3 + \hat{\epsilon}^6 \alpha_5 T^3 + \hat{\epsilon}^5 \alpha_6 T^2 E + \hat{\epsilon}^4 \alpha_7 E^2 T \\ + \hat{\epsilon}^8 \alpha_8 T^4 + \hat{\epsilon}^4 \alpha_9 E^4 + \hat{\epsilon}^5 \alpha_{10} E^3 T + \hat{\epsilon}^7 \alpha_{11} T^3 E + \hat{\epsilon}^6 \alpha_{12} T^2 E^2 + \dots$$

Dropping terms of order $O(\hat{\epsilon}^5)$ and higher and removing the bookkeeping parameter:

$$PE = \alpha_1 E^2 + \alpha_2 T^2 + \alpha_3 TE + \alpha_4 E^3 + \alpha_7 E^2 T + \alpha_9 E^4 + H.O.T. \quad (3.2)$$

The strain can be obtained from the potential energy by differentiating with respect to stress:

$$S = \frac{\partial PE}{\partial T} = 2\alpha_2 T + \alpha_3 E + \alpha_7 E^2$$

Rearranging, we write the stress as:

$$T = \frac{1}{2\alpha_2} S - \frac{\alpha_3}{2\alpha_2} E - \frac{\alpha_7}{2\alpha_2} E^2 \quad (3.3)$$

Similarly, the electric displacement can be obtained from the potential energy by differentiating with respect to the electric field:

$$D = \frac{\partial PE}{\partial E} = 2\alpha_1 E + \alpha_3 T + 3\alpha_4 E^2 + 2\alpha_7 TE + 4\alpha_9 E^3 \quad (3.4)$$

Although this approach ensures that we capture all possible nonlinearities, it does little to explain the physics behind each term. Thus, a more physical approach is taken, and the final results are compared to (3.3) and (3.4) to verify accounting for all nonlinearities.

The strain tensor can be defined to account for all three phenomena under investigation, elasticity, piezoelectricity, and electrostriction, as follows [91]:

$$\mathbf{S} = \mathbf{C}^{-1}\mathbf{T} + \mathbf{d}\mathbf{E} + \mathbf{M}\mathbf{E}^2$$

where \mathbf{C} and \mathbf{M} are the stiffness and electrostriction matrices respectively and \mathbf{d} is the piezoelectric-strain constant matrix. For the 3m-Rhombohedral crystal \mathbf{C} and \mathbf{M} are defined as [92]:

$$\mathbf{C} = \begin{pmatrix} C_{11} & C_{12} & C_{13} & 0 & 0 & 0 \\ C_{12} & C_{11} & C_{13} & 0 & 0 & 0 \\ C_{13} & C_{13} & C_{33} & 0 & 0 & 0 \\ 0 & 0 & 0 & C_{44} & 0 & 0 \\ 0 & 0 & 0 & 0 & C_{44} & 0 \\ 0 & 0 & 0 & 0 & 0 & 2(C_{11} - C_{12}) \end{pmatrix}$$

$$\mathbf{M} = \begin{pmatrix} M_{11} & M_{21} & M_{31} & M_{41} & 0 & 0 \\ M_{21} & M_{11} & M_{31} - M_{41} & 0 & 0 & 0 \\ M_{13} & M_{13} & M_{33} & 0 & 0 & 0 \\ M_{14} - M_{14} & 0 & M_{44} & 0 & 0 & 0 \\ 0 & 0 & 0 & 0 & M_{44} & 2M_{14} \\ 0 & 0 & 0 & 0 & M_{41} & M_{66} \end{pmatrix}$$

Re-arranging, we write the stress tensor as:

$$\begin{aligned} \mathbf{T} &= \mathbf{C}\mathbf{S} - \mathbf{C}\mathbf{d}\mathbf{E} - \mathbf{C}\mathbf{M}\mathbf{E}^2 \\ &= \mathbf{C}\mathbf{S} - \mathbf{e}\mathbf{E} - \mathbf{C}\mathbf{M}\mathbf{E}^2 \end{aligned} \tag{3.5}$$

where piezoelectric-stress constant matrix e for the 3m-Rhombohedral crystal is defined as [92]:

$$e = \mathbf{C} \mathbf{d} = \begin{pmatrix} 0 & 0 & e_{31} \\ 0 & 0 & e_{31} \\ 0 & 0 & e_{33} \\ 0 & e_{15} & 0 \\ e_{15} & 0 & 0 \\ 0 & 0 & 0 \end{pmatrix}$$

and

$$\mathbf{E}^2 = \mathbf{E} \mathbf{E}^T = \begin{pmatrix} E_x^2 \\ E_y^2 \\ E_z^2 \\ E_y E_z \\ E_x E_z \\ E_x E_y \end{pmatrix} = \begin{pmatrix} E_x^2 \\ E_y^2 \\ 0 \\ 0 \\ 0 \\ E_x E_y \end{pmatrix}$$

The electric displacement vector has also been defined empirically as [91]:

$$\mathbf{D} = \epsilon^T \mathbf{E} + \mathbf{d} \mathbf{T} + 2\mathbf{M} \mathbf{T} \mathbf{E} \quad (3.6)$$

where ϵ^T is the zero-stress permittivity matrix. Substituting for the stress tensor with equation (3.5):

$$\mathbf{D} = \epsilon \mathbf{E} + e^T \mathbf{S} - e^T \mathbf{M} \mathbf{E}^2 - 2\mathbf{M} e \mathbf{E} \mathbf{E} + 2\mathbf{M} \mathbf{C} \mathbf{S} \mathbf{E} - 2\mathbf{M} \mathbf{C} \mathbf{M} \mathbf{E}^2 \mathbf{E} \quad (3.7)$$

where $\epsilon^T = \epsilon + \mathbf{d} e$ and the zero strain permittivity matrix the 3m-Rhombohedral crystal is defined as [92]:

$$\epsilon = \begin{pmatrix} \epsilon_{xx} & 0 & 0 \\ 0 & \epsilon_{xx} & 0 \\ 0 & 0 & \epsilon_{zz} \end{pmatrix}$$

Since \mathbf{T} , \mathbf{C} , \mathbf{S} , e , \mathbf{M} , and \mathbf{E}^2 are originally higher-order tensors reduced using the Voigt notation to matrices, while \mathbf{D} , ϵ , \mathbf{E} are not, care must be taken when evaluating the last three

terms in equation (3.7). These terms have both reduced and regular tensors multiplied with each other. This issue is solved by un-reducing the tensors from their Voigt 6x1 form into the 3x3 tensor, as illustrated in Appendix B, before multiplication with \mathbf{E} .

Comparing equations (3.5) and (3.6) to equations (3.3) and (3.4), we find that the electric displacement equation in the literature does not capture all the nonlinearities, specifically the terms associated with α_4 and α_9 are missing. However, when considering equation (3.7), the missing nonlinearities are recaptured.

3.2 Nonlinear Constitutive and Governing Equations

Using the field definitions in equations (2.1), the non-trivial components of the stress tensor \mathbf{T} , equation (3.5), and polarization vector \mathbf{D} , equation (3.6), inside the piezoelectric after tensor manipulation, reduce to [91]:

$$T_{yz} = G \frac{\partial u_z}{\partial y} - eE_y - GME_x^2 + GME_y^2 \quad (3.8)$$

$$T_{xz} = G \frac{\partial u_z}{\partial x} - eE_x - 2GME_xE_y \quad (3.9)$$

$$D_x = \epsilon E_x + e \frac{\partial u_z}{\partial x} + 2ME_xT_{yz} + 4ME_yT_{xz} \quad (3.10)$$

$$D_y = \epsilon E_y + e \frac{\partial u_z}{\partial y} + 4ME_xT_{xz} - 2ME_yT_{yz} \quad (3.11)$$

where $M = M_{14}$ is the only relevant electrostrictive coefficient. Substituting with the shear stress from equations (3.8) and (3.9) into the electric displacement equations (3.10) and (3.11),

we obtain:

$$D_x = \epsilon E_x + e \frac{\partial u_z}{\partial x} + 2GM \frac{\partial u_z}{\partial y} E_x + 4GM \frac{\partial u_z}{\partial x} E_y - 6eM E_x E_y - 6GM^2 E_x E_y^2 - 2GM^2 E_x^3 \quad (3.12)$$

$$D_y = \epsilon E_y + e \frac{\partial u_z}{\partial y} - 4eM E_x^2 + 2eM E_y^2 - 2GM \frac{\partial u_z}{\partial y} E_y + 4GM \frac{\partial u_z}{\partial x} E_x - 6GM^2 E_x^2 E_y - 2GM^2 E_y^3 \quad (3.13)$$

Rewriting equations (2.9)–(2.11), after using the higher-order expressions for stress and electric displacement, equations (3.8)–(3.13), we obtain

$$\rho \ddot{u}_z = G \nabla^2 u_z - e \nabla \cdot \mathbf{E} + ML_1(E_x, E_y) \quad (3.14)$$

$$0 = e \nabla^2 u_z + \epsilon \nabla \cdot \mathbf{E} + ML_2(u_z, E_x, E_y) \quad (3.15)$$

$$\mu \dot{H}_z = \frac{\partial E_x}{\partial y} - \frac{\partial E_y}{\partial x} \quad (3.16)$$

where the nonlinear electrostriction differential operators $L_1(E_x, E_y)$ and $L_2(u_z, E_x, E_y)$ are given in Appendix C by equations (C.1) and (C.2), respectively. Applying the quasistatic assumptions stated in section 2.3 we can rewrite these equations, such as:

$$\rho \ddot{u}_z = G \nabla^2 u_z + e \nabla^2 \psi + MGL_1(\psi) \quad (3.17)$$

$$0 = e \nabla^2 u_z - \epsilon \nabla^2 \psi + ML_2(u_z, \psi) \quad (3.18)$$

where $L_1(\psi)$ and $L_2(u_z, \psi)$ are the quasistatic versions of the nonlinear electrostriction differential operators $L_1(E_x, E_y)$ and $L_2(u_z, E_x, E_y)$, respectively, given in Appendix C by equations (C.3) and (C.4)

3.3 Linearization Around a Bias Point

It is useful to linearize the fields around an equilibrium (operating point), defined by applied prestress (and the corresponding prestrain S_o) and DC electric field E_o . The linearized constants can be used in investigating the effect of biasing. The relevant constants found in equations (3.14) and (3.15) are the piezoelectric permittivity ϵ , the piezoelectric constant e , and the shear stiffness G . These are defined from the constitutive equations (3.8) to (3.11), such as:

$$\epsilon_{Lij} = \frac{\partial D_i}{\partial E_j} \Big|_{(E_{j_o}, S_{m_o})} \quad (3.19)$$

$$C_{Lmn} = \frac{\partial T_n}{\partial S_m} \Big|_{(E_{j_o}, S_{m_o})} = C_{mn} \quad (3.20)$$

$$e_{Ljn} = -\frac{\partial T_n}{\partial E_j} \Big|_{(E_{j_o}, S_{m_o})} \quad (3.21)$$

$$\text{or } e_{Lim} = \frac{\partial D_i}{\partial S_m} \Big|_{(E_{j_o}, S_{m_o})}$$

Therefore, the effective linearized permittivity of the piezoelectric under a set of electrodes applying a bias of E_{x_o} is:

$$\epsilon_{Lxx} = \epsilon - 6GM^2 E_{x_o}^2 \quad (3.22)$$

This will later be proven to allow the tuning of the sensitivity equation, and thus, the peak of maximum sensitivity could be shifted to lower values to match that of the sample under test. This will be discussed in detail in Chapter 4, specifically, equation (4.16) and Figure 4.2. For example, using the sensor to detect small changes in the dielectric constant of aqueous media, like blood plasma, is possible by applying a biasing electric field to drop down the effective relative permittivity to match that of blood plasma. Thus, any small change in the dielectric constant would create an observable shift in the resonance frequency of the BG wave. Figure 3.2 shows the plot of the equation (3.19), in the case of using PZT4 and assuming that the electrostrictive coefficient for PZT4 is $M = 12.7 \times 10^{-18}$. This value was experimentally identified, as will

be discussed later in Chapter 6. The Figure shows that applying a DC bias in the x-direction of about 14 MV/m is required to create a sensor that operates in water or blood plasma.

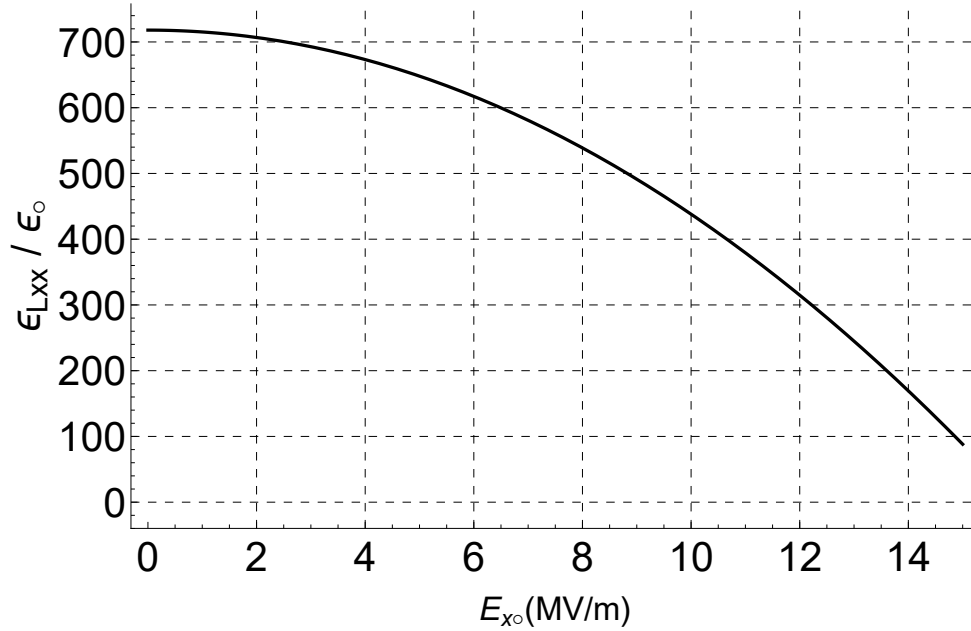


Figure 3.2: Linearized relative effective permittivity as a function of bias electric field. ϵ_0 is the free space permittivity.

3.4 Nondimensionalization

Following the nondimensionalization in section 2.4, the nonlinear equations (3.14) and (3.15) can also be nondimensionalized, such as:

$$\alpha \ddot{u}_z = \nabla^2 u_z - \nabla \cdot \mathbf{E} + \hat{M} \hat{L}_1(E_x, E_y) \quad (3.23)$$

$$0 = \frac{e^2}{G\epsilon} \nabla^2 u_z + \nabla \cdot \mathbf{E} + \hat{M} \hat{L}_2(u_z, E_x, E_y) \quad (3.24)$$

where $\hat{M} = \frac{MG}{el}$. The differential operator L_i is replaced with a nondimensional version \hat{L}_i , given in Appendix C. Similarly, the quasistatic nonlinear equations (3.17) and (3.18) can be nondimensionalized, such as:

$$\alpha \ddot{u}_z = \nabla^2 u_z + \nabla^2 \psi + \hat{M} \hat{L}_1(\psi) \quad (3.25)$$

$$0 = \nabla^2 u_z - \frac{G\epsilon}{e^2} \nabla^2 \psi + \hat{M} \hat{L}_{2A}(u_z, \psi) + \hat{M}^2 \hat{L}_{2B}(u_z, \psi) \quad (3.26)$$

3.5 Summary

In this chapter, the sources of nonlinearities in BG waves were investigated. Specifically, electrostriction in BG waves was analyzed and formulated into the constitutive equations of the sensor. Then, the possibility of the linearization of parameters around a bias point was investigated. The linearization approach showed that the sensor sensitivity could be enhanced and tuned towards aquatic media under test. Finally, the nondimensionalization was redone for the nonlinear system of equations.

Chapter 4

Eigenvalue Analysis

In this chapter, the sensor eigenvalue problem is investigated, and the sensor sensitivity is defined. Both cases of full and no metalization of the surface are considered. Finally, the mode shapes are outlined.

4.1 Sensor Eigenvalue Problem

In order to state the eigenvalue problem, we first apply the remaining boundary conditions to solve for the propagation constants. Substituting the solution from equations (2.35) to (2.41) in the no-load boundary condition, equation (2.17), yields:

$$U_o \kappa_u \left(G + \frac{e^2}{\epsilon} \right) \left(e^{i \frac{m\pi}{l} x} + e^{-i \frac{m\pi}{l} x} \right) \left(e^{i\beta t} + e^{-i\beta t} \right) - H_o \frac{m\pi e}{\epsilon l \beta} \left(e^{i \frac{m\pi}{l} x} - e^{-i \frac{m\pi}{l} x} \right) \left(e^{i\beta t} - e^{-i\beta t} \right) = 0 \quad (4.1)$$

This can be simplified in trigonometric form, such as:

$$4U_o \kappa_u \left(G + \frac{e^2}{\epsilon} \right) \cos(\pi m x) \cos(\beta t) + 4H_o \frac{m\pi e}{\epsilon l \beta} \sin(\pi m x) \sin(\beta t) = 0 \quad (4.2)$$

4.1.1 Metallized Surface

Applying a perfect conductor to the piezoelectric surface sets the transverse electric field at the surface to vanish. This case can also represent the limiting case of using a conductive liquid as the medium-under-test, and thus is important to analyze. It replaces the boundary condition in equation (2.18) by:

$$E_x \Big|_{y=0} = 0$$

Substituting by the solution from (2.38) and transforming into the trigonometric form yields:

$$4 \frac{m\pi e}{\epsilon l} U_o \sin(m\pi x) \cos(\beta t) - 4 \frac{H_o \kappa_h}{\epsilon \beta} \cos(m\pi x) \sin(\beta t) = 0 \quad (4.3)$$

For a non-trivial solution, the determinant of coefficients of the linear system obtained from equations (4.2) and (4.3) must vanish, such as:

$$\begin{vmatrix} \kappa_u (G + \frac{e^2}{\epsilon}) U_o & \frac{m\pi e}{\epsilon L \beta} H_o \\ \frac{m\pi e}{\epsilon l} U_o & -\frac{\kappa_h}{\epsilon \beta} H_o \end{vmatrix} = 0 \quad (4.4)$$

We define the following ratios between the propagation constants:

$$\eta = \frac{\kappa_h}{k_x} = \frac{\kappa_h l}{m\pi} \quad , \quad \zeta = \frac{\kappa_u}{k_x} = \frac{\kappa_u l}{m\pi} \quad (4.5)$$

and use them to rewrite the determinant (4.4), such as:

$$\begin{vmatrix} \eta \frac{m\pi}{l} (G + \frac{e^2}{\epsilon}) U_o & \frac{m\pi e}{\epsilon L \beta} H_o \\ \frac{m\pi e}{\epsilon l} U_o & -\frac{\zeta m\pi}{l \epsilon \beta} H_o \end{vmatrix} = 0 \quad (4.6)$$

For a nontrivial solution, the determinant must vanish, which yields:

$$\eta \zeta = \frac{e^2}{G\epsilon + e^2} \quad (4.7)$$

The positive value for η corresponds to the decaying displacement and magnetic fields in the lower-half space ($y < 0$), and ζ is positive for physical positive mode numbers. The propagation

ratios, equation (4.5), can be used to simplify the dispersion relation, equation (2.33), for the displacement field, such as:

$$\beta^2 = c_s^2(k_x^2 - \kappa_u^2) = c_s^2 k_x^2 (1 - \zeta^2) \quad (4.8)$$

Likewise, we simplify the dispersion relation for the magnetic field as:

$$\beta^2 = c_l^2(k_x^2 - \kappa_h^2) = c_l^2 k_x^2 (1 - \eta^2) \quad (4.9)$$

The wave velocity can, therefore, be written such as:

$$v^2 = \frac{\beta^2}{k_x^2} = c_s^2(1 - \zeta^2) = c_l^2(1 - \eta^2) \quad (4.10)$$

We can use equation (4.10) to solve for η as follows:

$$\eta = \sqrt{1 - \left(\frac{c_s}{c_l}\right)^2(1 - \zeta^2)}$$

Since the ratio $\frac{c_s}{c_l}$ is of the order $O(10^{-5})$, we can take $\eta \approx 1$ and use equation (4.7) to obtain an expression for the decay ratio of the displacement field in the lower-half space as:

$$\zeta \approx \frac{e^2}{G\epsilon + e^2} \quad (4.11)$$

This means that we can write $\kappa_h \approx k_x = \frac{m\pi}{l}$. This statement is also true for the upper half space, and therefore we can write $\kappa_h^u \approx \kappa_h \approx k_x$ as well.

4.1.2 Bare Surface

On the other hand, applying the bare surface boundary conditions, equations (2.18) and (2.19), in trigonometric form, yields:

$$4 \frac{m\pi e}{\epsilon l} U_o \sin(m\pi x) \cos(\beta t) - 4 \frac{H_o(1+r)\kappa_h}{\epsilon\beta} \cos(m\pi x) \sin(\beta t) = 0 \quad (4.12)$$

For a non-trivial solution, the determinant of coefficients of the linear system obtained from equations (4.2) and (4.12), while using the definitions in (4.5), must vanish, such as:

$$\begin{vmatrix} \eta \frac{m\pi}{l} (G + \frac{e^2}{\epsilon}) U_o & \frac{m\pi e}{\epsilon L \beta} H_o \\ \frac{m\pi e}{\epsilon l} U_o & -\frac{\zeta m\pi}{l \epsilon \beta} H_o (1 + r) \end{vmatrix} = 0$$

Taking $\eta \approx 1$, the determinant is solved, such as:

$$\zeta = \frac{e^2}{G\epsilon + e^2} \frac{1}{1 + r} \quad (4.13)$$

Finally, the boundary condition on the normal component of the electric displacement, equation (2.20), is identically satisfied by substituting the displacement and electric fields into the equation. Therefore, the natural frequencies for a bare surface can be written following equation (4.8), such as:

$$\omega = \beta = \frac{c_s m \pi}{l} \sqrt{1 - \zeta^2}$$

The expression indicates that the electromagnetic part of the mode shape acts like damping to the acoustic part of the mode. Substituting for c_s , α , k_x , and ζ , we get:

$$\omega = \frac{m\pi}{l} \sqrt{\frac{G + \frac{e^2}{\epsilon}}{\rho}} \sqrt{1 - \frac{e^4}{(G\epsilon + e^2)^2} \frac{1}{(1 + r)^2}} \quad (4.14)$$

This expression shows that the natural frequency of the resonant sensor depends on r , the ratio of the zero strain electric permittivity of the piezoelectric material, ϵ , to that of the medium in the upper half-space, ϵ^u .

4.1.3 Higher Modes

Since m was pinned to be the physical number of inter-digitated fingers used and not the actual spatial mode number, a multiplier, n , is added to allow for modeling higher modes. Therefore, a system with $m = 4$ and $n = 2$ has 4 IDT fingers (2 pairs) excited at the second resonant

mode, Figure 4.1. Therefore, the resonant frequencies are rewritten, such as:

$$\omega_n = n \frac{m\pi}{l} \sqrt{\frac{G + \frac{e^2}{\epsilon}}{\rho}} \sqrt{1 - \frac{e^4}{(G\epsilon + e^2)^2} \frac{1}{(1+r)^2}} \quad (4.15)$$

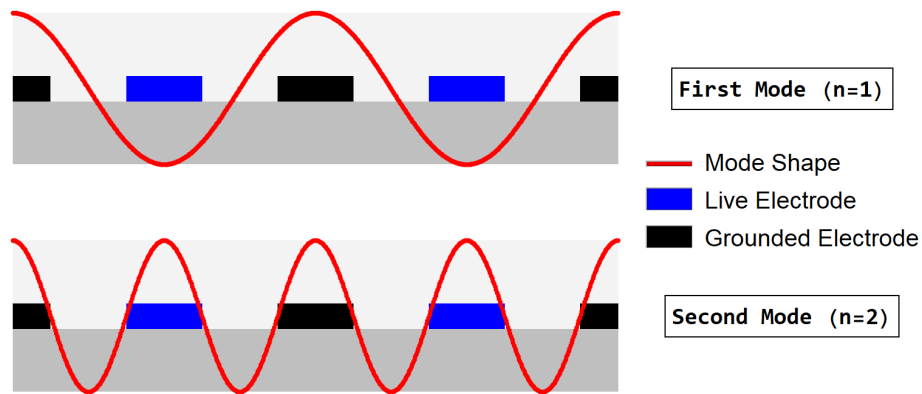


Figure 4.1: Excitation of the first and second modes, using 4 IDT fingers, including the two half-electrodes at the edges.

4.2 Sensor Sensitivity

Equation (4.15) promises a correlation between the resonance frequency of a Bleustein-Gulyaev wave propagating along a bare surface and the electric permittivity of the medium on top of it. However, the equation is highly nonlinear. The sensitivity of the resonance shift depends

on the permittivity of the medium and the piezoelectric. It can be calculated, such as:

$$\begin{aligned}
S_{\omega n} &= \frac{\partial \omega_n}{\partial \epsilon^u} \\
&= -n \frac{m\pi}{l} \frac{e^4 \epsilon \epsilon^u}{(\epsilon + \epsilon^u)^3 (e^2 + G\epsilon)^2} \frac{(1 + (\epsilon/\epsilon^u))(e^2 + G\epsilon)}{\sqrt{(1 + (\epsilon/\epsilon^u))^2 (e^2 + G\epsilon)^2 - e^4}} \sqrt{\frac{e^2 + G\epsilon}{\rho \epsilon}} \\
&= -n \frac{m\pi e^4 r^2}{l(1+r)^2 \sqrt{\rho \epsilon^3}} \frac{1}{\sqrt{(1+r)^2 (e^2 + G\epsilon)^3 - e^4 (e^2 + G\epsilon)}} \tag{4.16}
\end{aligned}$$

Figure 4.2 shows the sensitivity S_ω as a function of the medium relative permittivity $\epsilon_r^u = \epsilon^u/\epsilon_o$ for a sensor made of Lead Zirconate Titanate Navy Type I (PZT4), where ϵ_o is the free space permittivity. The figure shows the drop in the natural frequency for a unit change in the medium relative permittivity. We note that the relative permittivity of PZT4 at zero strain is $\epsilon_r = 718$. It can be seen that maximum sensitivity occurs in the vicinity of half the piezoelectric permittivity: $\epsilon^u \approx \frac{1}{2}\epsilon$

Common applications of permittivity sensors target gaseous or aqueous media, which usually have dielectric constants below 100. For the sensor to demonstrate optimal sensitivity in that ‘golden range’, the sensitivity curve needs to be shifted down. This can be achieved by selecting a piezoelectric with a lower relative permittivity. However, the sensor, in this case, will have optimal performance in a limited zone within the golden range.

Furthermore, there is a limited selection of piezoelectric materials with permittivities in that range, such as Zinc Oxide, Lithium Tantalate, and Lithium Tetraborate. This subset of piezoelectrics suffers from a low piezoelectric coefficient $e < 1$, see Table A.1. One promising candidate is Lithium Niobate, LiNbO_3 . LiNbO_3 has a low permittivity and a low, but yet acceptable, piezoelectric coefficient.

Therefore, we investigate an alternative approach that permits the tunability of the sensitivity of the sensor in real-time to tune the optimal sensitivity in the range of interest. As a first approximation, the effective parameters, equations (3.19) to (3.21), linearized around a bias point,

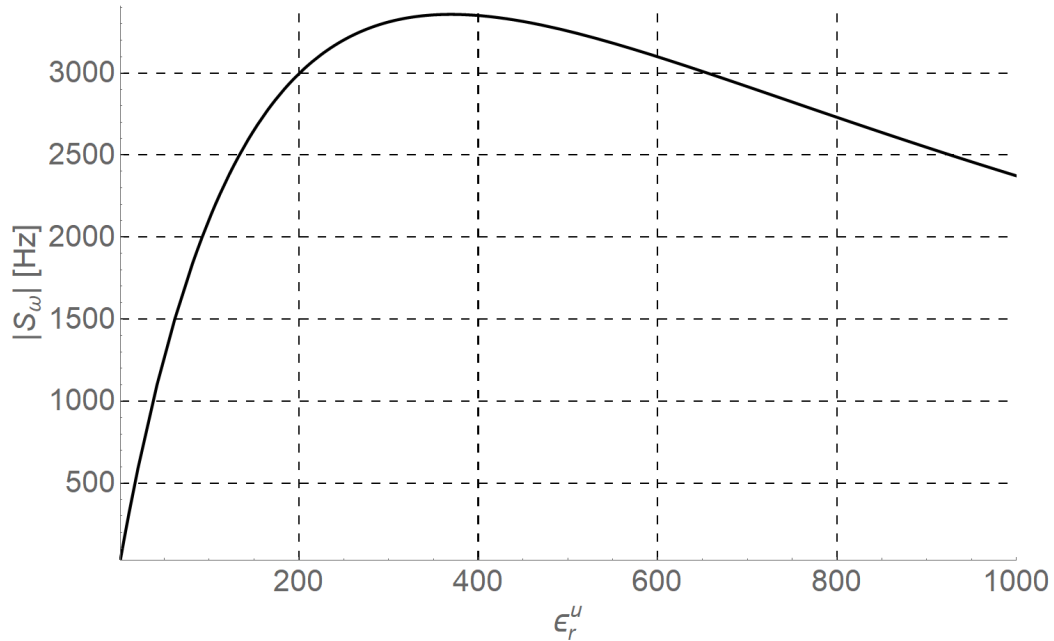


Figure 4.2: The sensitivity S_ω of a frequency-shift PZT4 sensor as a function of the medium relative permittivity ϵ_r^u .

can be used to estimate the effect of bias on the sensitivity. This is shown in Figure 4.3, where the biasing electric field is observed to tune the sensor operating range on the fly.

4.3 Eigenfunctions

The harmonic form of the displacement field was found from equation (2.35) to be:

$$u_z(x, y, t) = U_o \phi_n(x, y) e^{i\omega_n t} \quad (4.17)$$

where $\phi_n(x, y)$ is the mode shape and n is the mode number. Substituting equation (4.17) for the displacement into equation (2.24), yields:

$$\frac{G + e^2/\epsilon}{\rho} \nabla^2 \phi_n + \omega_n^2 \phi_n = 0 \quad (4.18)$$

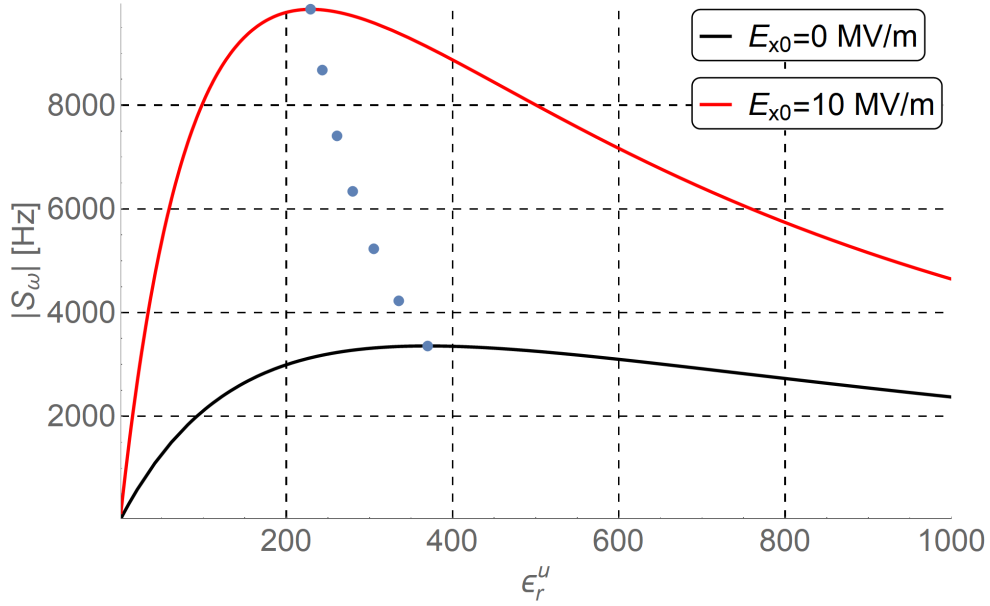


Figure 4.3: Biased sensitivity of PZT4, under applied biasing electric fields of $E_{x_0} = 0$ MV/m (black) and $E_{x_0} = 10$ MV/m (red). The blue markers track the position of maximum sensitivity.

Equation (4.18) is a Laplacian equation and can be solved similarly to the analysis in section 2.2. Therefore, the mode shapes can be written, such as:

$$\phi_n(x, y) = Ae^{-\kappa_n y} \cos(k_n x) \quad (4.19)$$

where $\kappa_n = \zeta k_n$, $k_n = \frac{nm\pi}{l}$, and n is an integer denoting the mode number. Additionally, they can be normalized by requiring that:

$$\int_0^\infty \int_0^l \phi_n^2(x, y) dx dy = 1$$

which is satisfied by setting: $A = \sqrt{\kappa_n/l}$. The first and second modeshapes $\phi_1(x, y)$ and $\phi_2(x, y)$, for $m = 4$, are plotted in Figure 4.1.

Under the quasi-static approximation, the mode shape for the potential takes the same form,

such as:

$$\psi(x, y, t) = \psi_0 \phi_n(x, y) e^{i\omega_n t} \quad (4.20)$$

4.4 Summary

In this chapter, the eigenvalue analysis for the resonator was carried out for the metallized and bare surfaces. The analysis proved that the resonator can be used as a permittivity sensor, and the sensor sensitivity was investigated. Finally, the linear mode shapes were formulated.

Additionally, the eigenvalue analysis shows that the BG wave speed is close to acoustic wave speeds and that the ratio $\frac{c_s}{c_l}$ is of the order $O(10^{-5})$. Since the higher (THz) frequencies of the electromagnetic wave are not directly excited, the system will not respond in that fast time scale. Moreover, the mechanical structure is too stiff to respond to THz excitations. This justifies the use of the quasistatic approximation.

Chapter 5

Sensor Design, Fabrication, and Characterization¹

In this chapter, the basic sensor structure is explained in detail. Then, the fabrication and post-fabrication steps are illustrated. Finally, the different experimental setups and configurations used in characterization are elucidated.

5.1 Sensor Prototypes

5.1.1 Sensor Design

The proposed design, shown in Figure 5.1, employs an inter-digitated transducer, or IDT, in order to excite the BG wave. The IDT is designed as an array of electrode “cells” with a spatial

¹Parts of this chapter are adapted from **Elhady, Alaa** and E. M. Abdel-Rahman, “Characterization of shear horizontal waves using a 1D laser Doppler vibrometer,” *Sensors*, vol. 21, no. 7, p. 2467, 2021

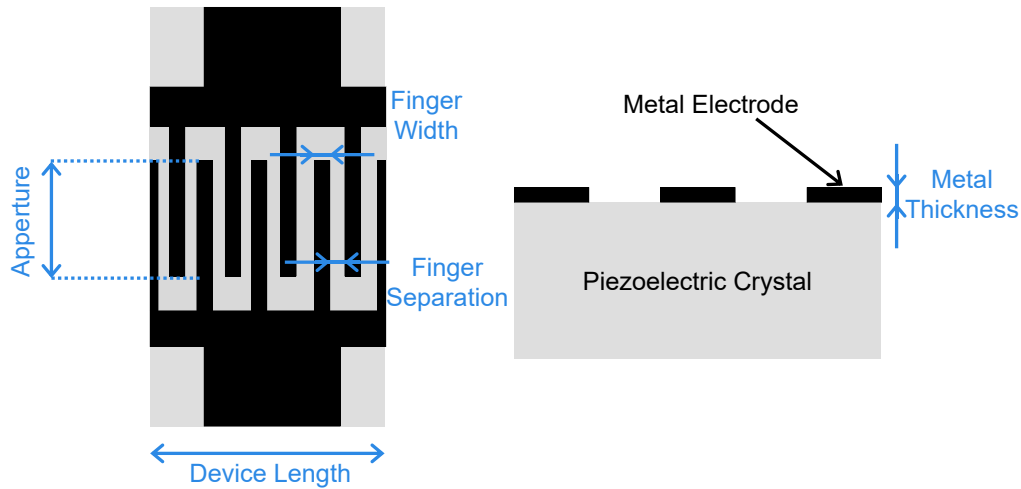


Figure 5.1: The BG sensor IDT structure

periodicity equal to the wavelength. Each cell has two metal electrodes, each with a width of $\lambda/4$, and separated by $\lambda/4$. The overlap of the fingers defines the aperture of the wave, where the wave propagates.

To realize the resonator, two methods can be used to achieve wave reflection at the resonator edges. The first and more traditional method [93] is using an array of shorted metal electrodes with both the width and the separation of the fingers set at $\lambda/4$. This array needs to consist of a large number of fingers [94] to achieve good reflectivity. Figure 5.2 shows the schematic of metal electrode reflectors as means to reflect the wave.

Another approach utilizes edge reflectors [21], which promises a compact size with a better resonant performance in terms of quality factor. The edge of the resonator is etched to create a piezoelectric-air interface. This creates a sudden change in acoustic impedance, which leads to acoustic reflection. Figure 5.3 shows the schematic of using trenches to reflect the wave.

One limitation in this design is the minimum feature of fabrication. It imposes a design

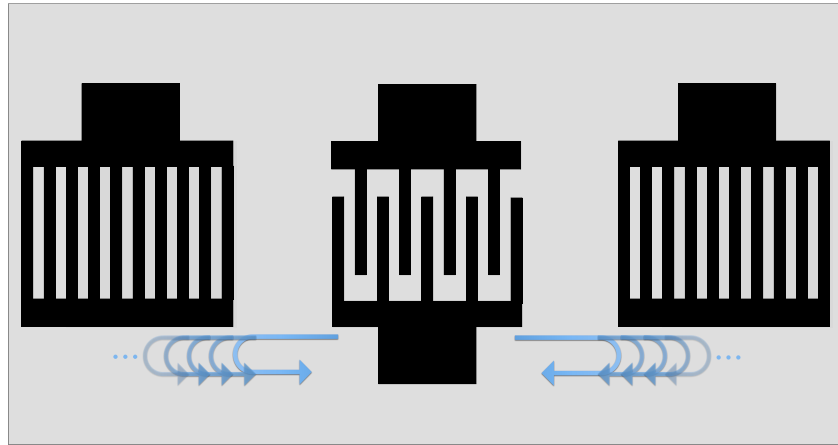


Figure 5.2: Schematic of the use of metal electrode reflectors to reflect the wave and create the resonator.

restriction on the minimum allowed wavelength. In edge reflectors, the smallest feature is $\lambda/8$ [21], and it occurs at the outermost (edge) electrodes, while electrode reflectors have $\lambda/4$ as their smallest feature. Therefore, edge reflection is limited by the minimum feature of fabrication, more than the traditional electrode reflection approach.

The number of fingers provides a trade-off between electric-to-acoustic energy coupling and impedance matching. A large number of fingers improves the chance of exciting/capturing the wave more efficiently, however, it also increases the resonator's capacitive impedance. Aperture size was reported to alter the effective region of transduction and thus the insertion loss. It was also found to affect the overall energy coupling and impedance matching [95], similar to the number of fingers. The general IDT design rule sets the aperture size to be several multiples of the wavelength [96].

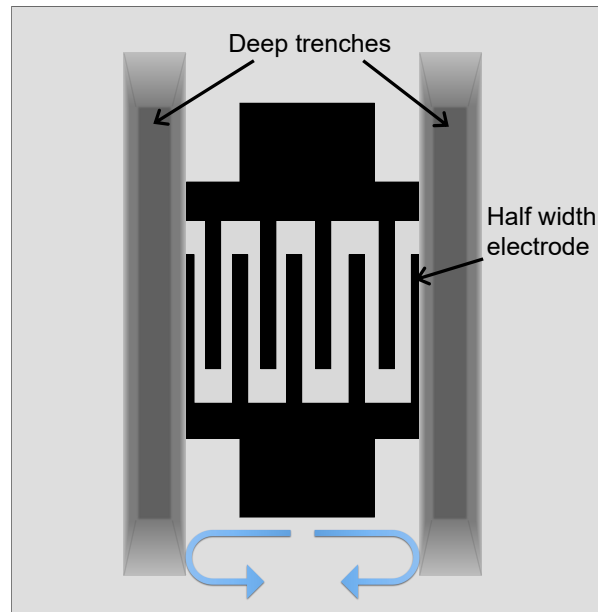


Figure 5.3: Schematic of the resonator using deep trench edges to reflect the wave.

5.1.2 PZT4 Sensors

The first choice for the substrate material was shear poled 15x15x1mm PZT4. It was purchased from APC International [97], poled but un-electroded. It was selected because of its high shear piezoelectric constant [98], $e = 12.7$, and high electromechanical coupling coefficient. The relation describing the shear coupling coefficient was found to be [99]:

$$K_{15}^2 = \frac{e^2}{e^2 + G\epsilon}$$

Using this formula, the coupling coefficient for PZT4 is approximately equal to 71%. The material constants collected during the literature survey are tabulated in Appendix A for reference, in Table A.1. PZT4 was selected because it scored the highest shear coupling coefficient and was conveniently available commercially in a shear-poled state.

Different designs were implemented using the edge reflection and the edge trenches techniques. Two designs, one set to resonate at 64.8 MHz, and the other at 161.9 MHz were implemented. However, during fabrication, the 161.9 MHz resonator was destroyed. This was because of unforeseen fabrication limitations on the minimum feature. Since the 161.9 MHz design had a minimum dimension (4 μm) smaller than that of the 64.8 MHz design (10 μm), it was completely etched.

One of the biggest fabrication issues that were found with this PZT4 chip was the grainy lattice structure. This caused the surface roughness to be in the order of few microns and thus had to be Chemically/Mechanically Polished (CMP) prior to fabrication. This was done using a commercial service outside of the country.

The chips were polished to few tens of nanometers, however, the grain boundaries were still visible. To further investigate, scanning electron microscopy, SEM, was used. Figures 5.4 show SEM images obtained for one of the defects of the polished PZT4. Figures 5.4b to 5.4d show successively increasing magnification of one of the defects visible in Figure 5.4a. The view in Figure 5.4d shows the individual grains. They can be seen to vary in size between 50 nm and 75 nm.

Since these defects were only one order of magnitude less than the wavelength, they may have interfered with the wave operation, reducing the coupling efficiency or distorting the frequency response.

5.1.3 LiNbO₃ Sensors

The grains and defects of PZT4 were a motivation to test another material, in parallel, as a prototype. Therefore, Lithium Niobate was selected as a second prototype. LiNbO₃ is a single crystal material, and thus it would not suffer from the issue of grains. Moreover, its linear and

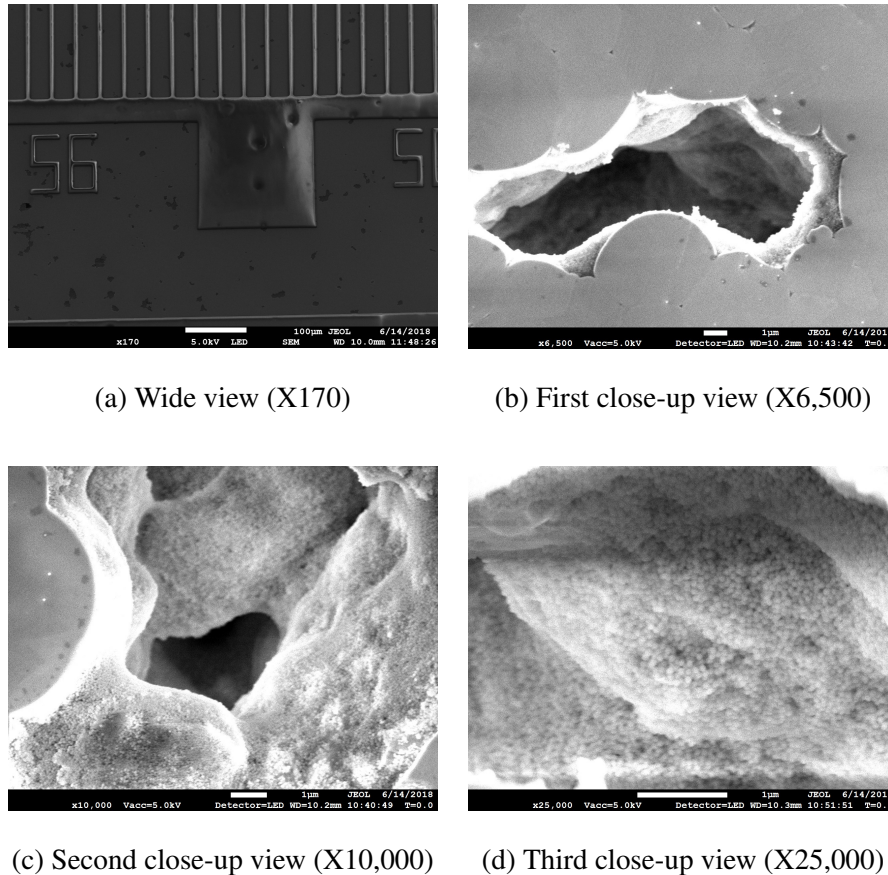
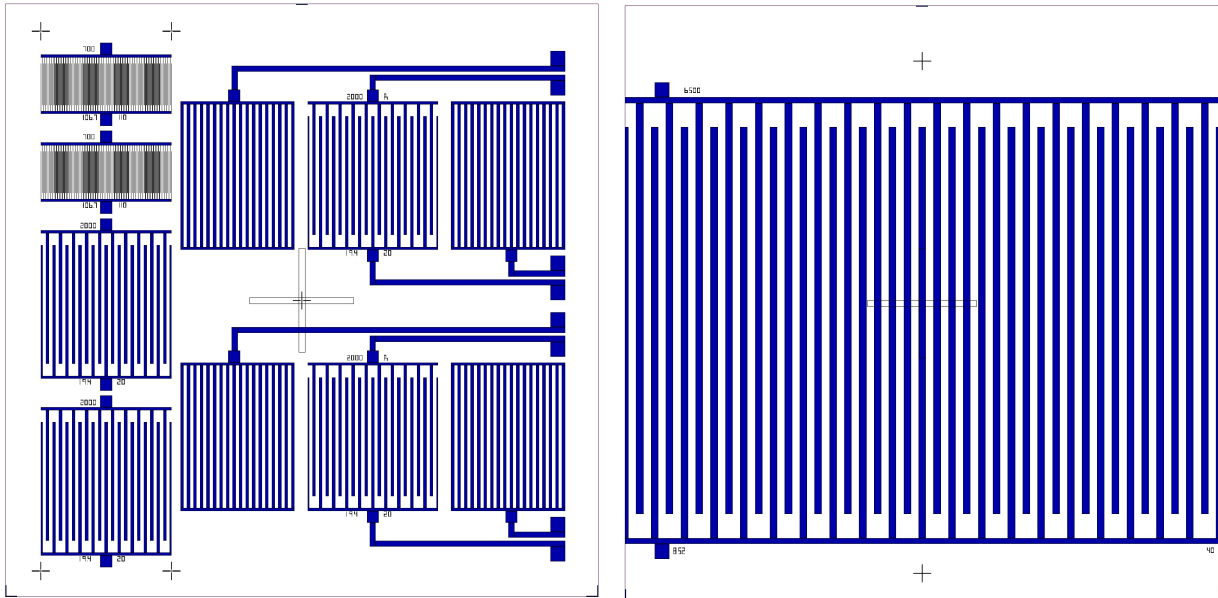


Figure 5.4: Post fabrication SEM photos for the PZT4. A grain defect was brought into focus and several close-up views were taken.

nonlinear coefficients are attractive, and its permittivity is close to that of aqueous media, and thus would be more sensitive as a sensor, as proven earlier in section 4.2. Although the permittivity of LiNbO_3 is much less than its counterpart in PZT4, LiNbO_3 is much stiffer than PZT4. That is why the coupling coefficient K_{15} for LiNbO_3 is approximately equal to 65%, which is close to PZT4 and is still considered quite high. The complete list of relevant material properties for LiNbO_3 are listed in Appendix A, Table A.1. A shear poled and electroded 10x10x3mm substrate

was purchased from Boston Piezo Optics [100], with a 41° X-cut.

Select design variations were implemented using the LiNbO_3 at different frequencies. Designs using the electrode reflection and the edge trenches techniques were implemented.



(a) Design of different sensors, on a single chip

(b) Design with wave reflection on chip's edges

Figure 5.5: Different LiNbO_3 designs

Figure 5.5a shows the first mask layout used in the LiNbO_3 -based sensors. This mask included sensors designed to operate at 21.4 MHz and others at 117.5 MHz. However, similarly to the 161.9 MHz PZT4 design, the 117.5 MHz LiNbO_3 design also did not survive the fabrication. The four sensors on the left column still required post-fabrication processing, namely using a high-power laser to cut the grooves needed for edge reflection. In an attempt to avoid this post-processing step, another design was implemented, close to the edges of the chip, as shown in figure 5.5b. This design, however, was done at a lower resonant frequency, at 9.4 MHz.

5.2 Fabrication

The fabrication took place in the cleanroom at the Quantum Nano Center, QNC, at the University of Waterloo. This was partially funded by the Micro/Nanotechnology, MNT, award from CMC Microsystems. The PZT4 mask was fabricated at Alberta University in the nanoFAB.

5.2.1 Fabrication Process

The fabrication process used was a single mask process. Figure 5.6 shows the PZT4 sample during and after different steps of preparation and fabrication, and Figure 5.7 shows the fabrication process recipe where details of the steps are described below. Figures 5.8 and 5.9 show the final electrodes patterned on the LiNbO_3 substrate.

The metal sputtering step was only necessary for PZT4 since LiNbO_3 was purchased pre-coated with 350 nm of gold/chromium on both sides. The minimum Al layer thickness needs to be 1% of the wavelength of the wave following the literature [101], which translates to 400 nm for the 64.8 MHz design. Moreover, this thickness must be kept below 5% of the wavelength to avoid mechanical loading, which in turn drops the coupling efficiency. Therefore, the aluminum thickness was set to 400 nm.

Additionally, the LiNbO_3 designs were implemented using the Heidelberg MLA150 Maskless Aligner, while the PZT4 was patterned using the SUSS Mask Aligner. During the PZT4 fabrication, the Maskless Aligner was not yet operational. Indeed, using the Maskless Aligner was considerably faster than waiting for the mask to be fabricated and then used.

Based on the wet etching process used to etch the thin deposited Al layer, an over-etch equal to the layer thickness is expected from both sides of the Aluminum layer. This over-etch is to be taken into consideration when designing the filter, and the dimensions on the mask are

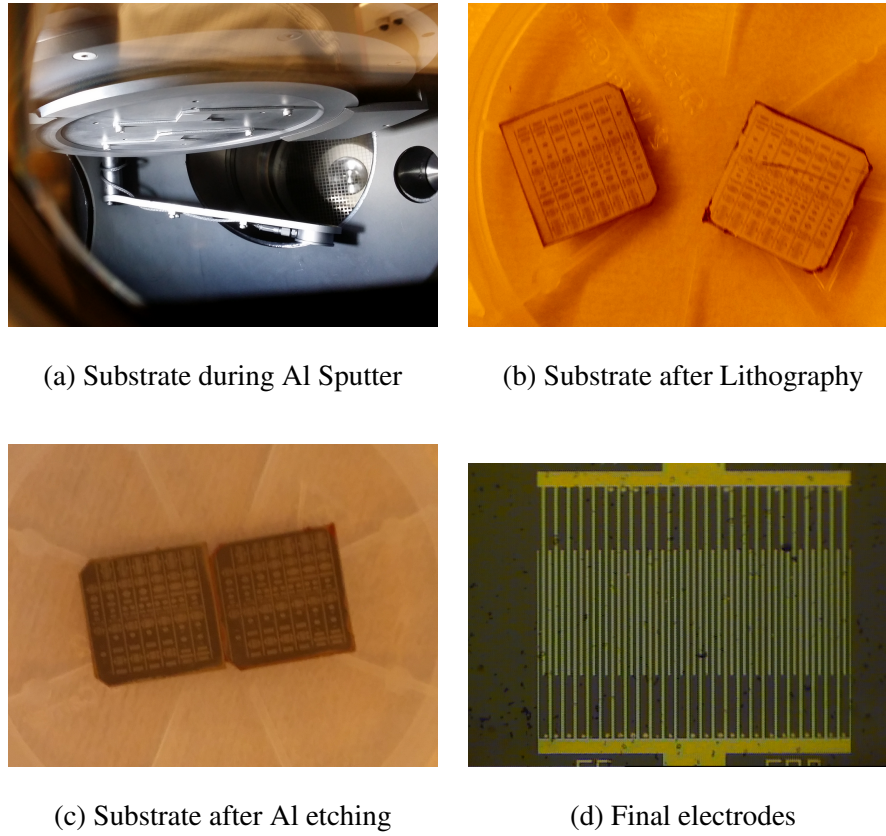


Figure 5.6: Photos for the PZT4 at different steps during fabrication

extended beyond the actual intended dimensions. However, it is also vital that the over-etch does not completely destroy the fingers. Figure 5.10 shows an image of the LiNbO_3 electrodes, with a close-up view of the outermost finger. This is where the smallest feature exists, and the figure shows that it is only minimally over-etched and therefore is expected to function properly. However, as mentioned at the beginning of this section, higher frequency designs did not survive. The details of the process recipe were as follows:

Process:

- Ultrasonic cleaning of the substrate in ultrasonic bath, while:
 - Immersed in Acetone for 10 Minutes
 - Immersed in Isopropyl alcohol (IPA) for 5 Minutes
 - Water rinsing
- (PZT4 Only) 400 nm Aluminum sputtering using the AJA Sputter Twin Chamber (48 minutes with 50W at 10mT). Strike was 27sccm Argon Gas with 200W sputter at 3mT.
- Spin coating of the Shipley-S1811 photoresist (PR) using REYNOLDSTECH twincoater on two steps (below), followed by a bake at 110 °C for 90 seconds.
 - 500 RPM, ramp of 100 RPM/s for 5 seconds
 - 5000 RPM, ramp of 500 RPM/s for 60 seconds
- Photolithography using:
 - (PZT4 Only) SUSS Mask Aligner, for 5 seconds and 25 mW/cm² intensity
 - (LiNbO₃ Only) Heidelberg MLA150 Maskless Aligner with a dose of 100 mW/cm²
- UV development using MF319 for 60 seconds.
- Wet etching of AL/AU layer using AL/AU-Etchant.
- Striping of PR using Acetone, followed by IPA.
- Surface profiling using profilometer and microscope

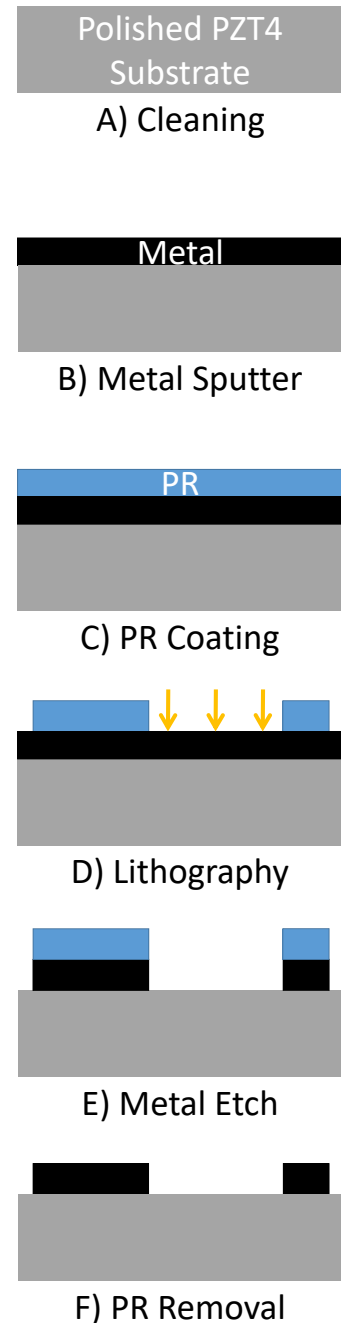


Figure 5.7: Process steps

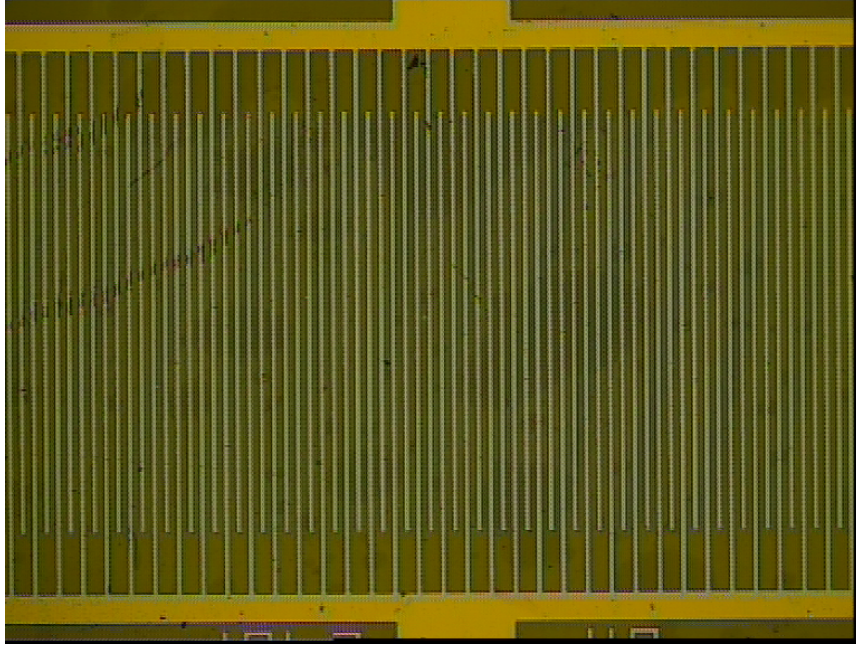


Figure 5.8: Microscopic image of the LiNbO_3 substrate with patterned IDT electrodes.

The fabricated IDTs were investigated under a white-light interferometry profilometer to assess the fabrication process. Figure 5.11 shows the readout of the profilometer, for the PZT4 sensor. The metalization thickness of the PZT4 IDT electrodes was measured at 510 nm. Since the sputtering was set at 400 nm, this indicates that the process could use finer tuning. However, for the purpose of this work, the extra 110 nm do not pose any risk and is not expected to affect operation. Therefore, the fabrication process was not repeated.

Figure 5.12 shows the profilometer readout of the IDT electrodes of the LiNbO_3 sensor. The manufacturer-provided specifications state that the metalization layer is 350 nm, however from Figure 5.12, it can be seen that the value is approximately 1.14 μm . This large difference creates a limitation on the smallest BG wavelength possible on LiNbO_3 . The metal thickness should be

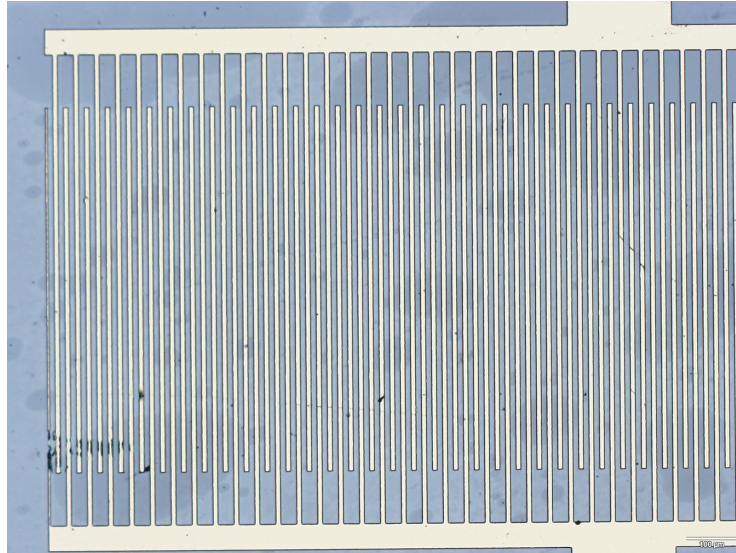


Figure 5.9: Microscopic image of the LiNbO_3 substrate with patterned IDT electrodes using a different illumination method. LiNbO_3 is semitransparent.

less than 5% of the BG wavelength [101] to avoid mechanically loading the surface. Therefore, the smallest BG wavelength possible is limited to $24\ \mu\text{m}$. This was smaller than the smallest wavelength designed on LiNbO_3 sensors and therefore should not create any issues with the fabricated designs.

The profilometer was also used to assess the minor scratch-looking defects, Figures 5.8 and 5.9, and check if these scratches are deep enough to hinder operation. Figure 5.13, shows that the scratches are superficial, at less than 15% of the metalization layer depth. This can also be seen in Figure 5.12. Therefore, they do not affect electrical connectivity and are much smaller than the BG wavelength to affect the sensor operation.

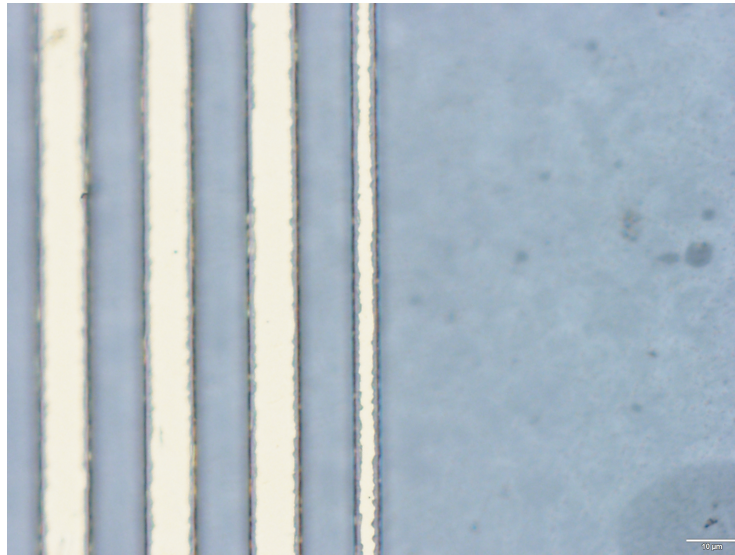


Figure 5.10: Microscopic image of the LiNbO_3 substrate with a close-up view of the edge electrode. The electrode shows minimal over-etching.

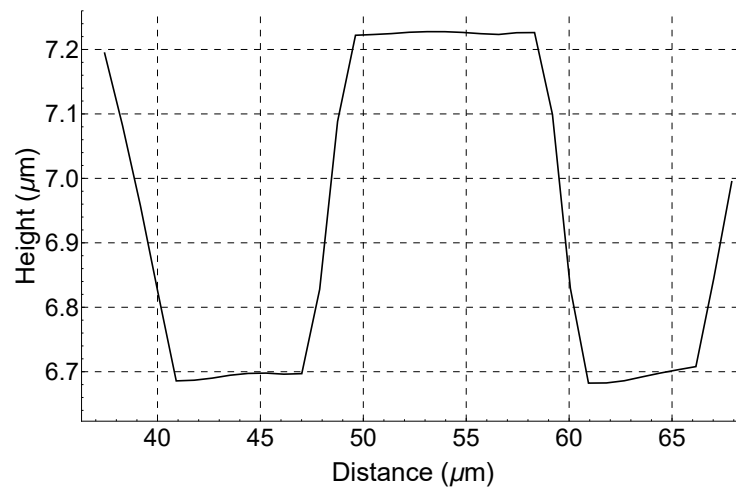


Figure 5.11: Profilometer measurement of the IDT fingers on the PZT4 sensor.

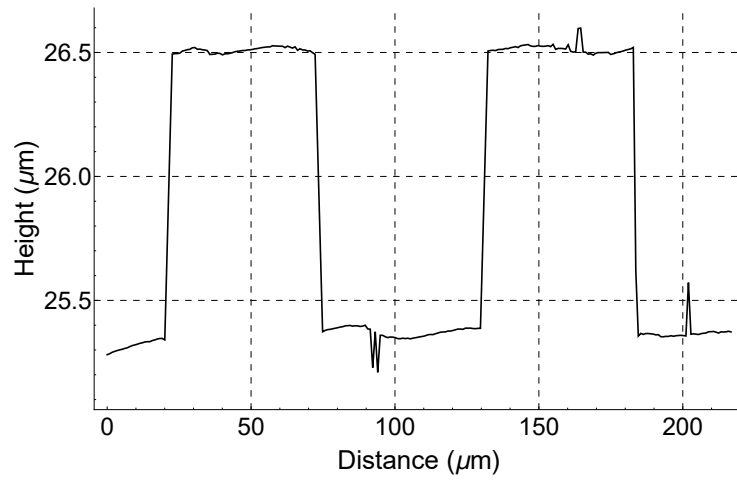


Figure 5.12: Profilometer measurement of the IDT fingers on the LiNbO_3 sensor. The measured metal thickness does not match the manufacturer provided specifications.

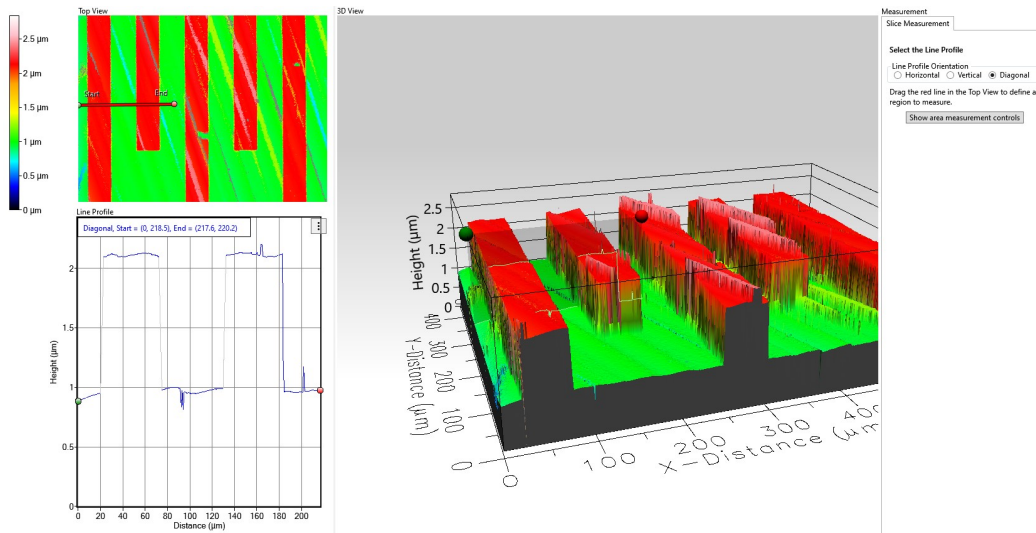


Figure 5.13: Profilometer screenshot during the measurement of the LiNbO_3 sensor. The scratches on the surface are superficial and do not pose a problem.

5.2.2 Post-Processing

Post-processing of the sample was performed using the QuickLaze-50 Laser Trimmer to create vertical trenches, Figure 5.14. They created the sharp edge required to achieve edge

reflection. The trenches were aligned at the edges of the outermost electrodes for each individual sensor.

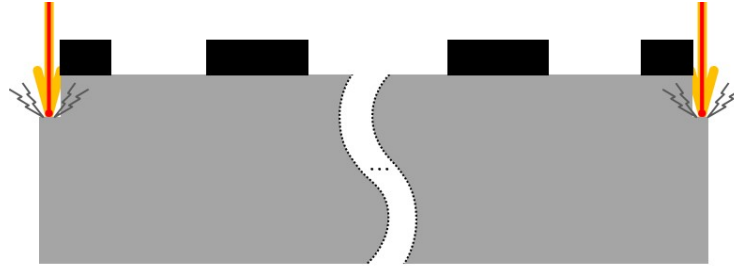


Figure 5.14: Laser trimming at resonator edges.

The trench depth created by the Laser trimmer depends on the etch rate of the laser. This is a function of two fixed characteristics and other variable ones. The fixed factors affecting the etch rate are the material (substrate to be etched) type and the laser wavelength. Although the latter is sometimes variable, it is often just a choice between two (or more) pre-set values. For instance, in the QuickLaze-50, there were two options; a green laser and an ultraviolet UV one. UV laser usually packs more energy density, however, it depends on how it will interact with the material. For LiNbO_3 , UV laser seemed to cause excessive heat damage in the region surrounding the trench, and thus it was avoided.

The variable options are; power p , number of passes n , pulse repetition frequency f , speed s , and spot size. The spot size can also control the width of the trench but was kept constant since it also affects the trench width. The depth can, thus, be formulated such as:

$$d = n \frac{kpf}{s} \quad (5.1)$$

where k is a constant defined by the fixed characteristics, as well as the spot size. The spot size was set to $50 \mu\text{m}$, and the green laser was chosen. The remaining variables were tuned to obtain the desired depth.

The trench depth should be enough to completely reflect most of the wave. The BG wave is a surface wave that attenuates rapidly into the substrate, following the term $e^{-\kappa_u y}$ from equation (2.35), where the value of κ_u was found to depend on the device wavelength and substrate type, equation (4.5). However, this trench should not go all the way into the substrate to facilitate handling the die after the cutting is complete. It would also take a huge time (tens of hours) using the available laser trimmer.

Using Finite Element Analysis, FEA, the wave was simulated to investigate the minimum trench depth needed. The wavelength used was $40\mu m$, and the material was PZT4. Figure 5.15 shows the effect of different groove depths on the wave. From the figure, it is clear that at $50\mu m$ deep, the wave is well contained, and no visible leakage is observed. Therefore, the depth should be set to be larger than the BG wavelength. Shallower trenches can still work but would suffer from lower edge reflectivity, and therefore a lower resonant quality factor.

Using the profilometer to directly characterize the trench depth was proven unsuccessful. Figure 5.16 shows that the surface roughness at the bottom of the trench was extremely high. This stopped the light from reflecting back to the sensor, and the software attempted to interpolate the results. The width of the trench was found to be between $50\mu m$ and $70\mu m$. The laser spot size was set to $50\mu m$, however, the nature of light diffraction caused the edges to experience a lower non-zero dose of laser radiation.

In order to characterize the depth, a low-tech approach was used. Using the metered microscope belonging to the Laser Doppler Vibrometer, the laser was focused on the surface of the substrate, and the microscope focus reading was recorded. Then the laser was focused on the bottom surface, and the focus knob on the microscope was manually scanned until the spot came into focus in the viewfinder. The microscope focus reading was recorded again, and the difference in the readings indicated an approximate value for the depth.

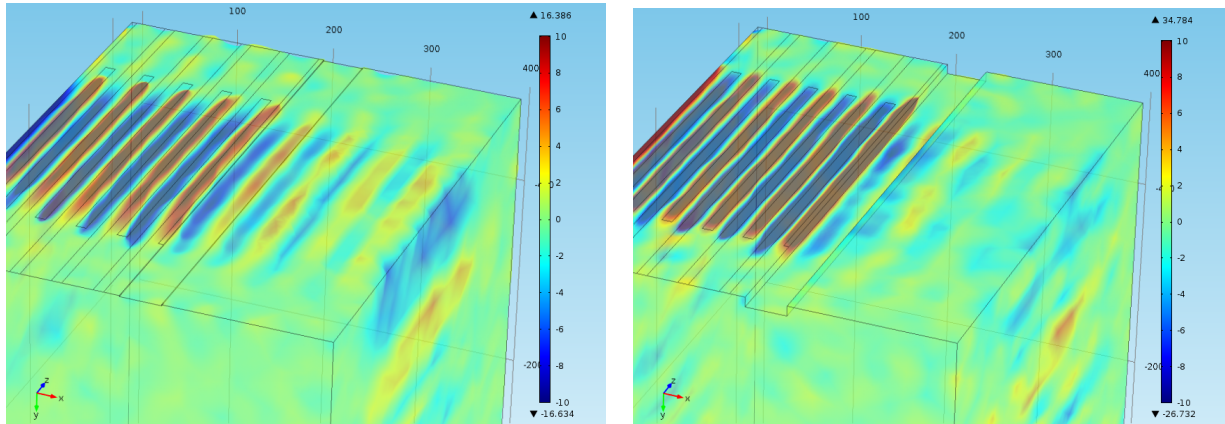
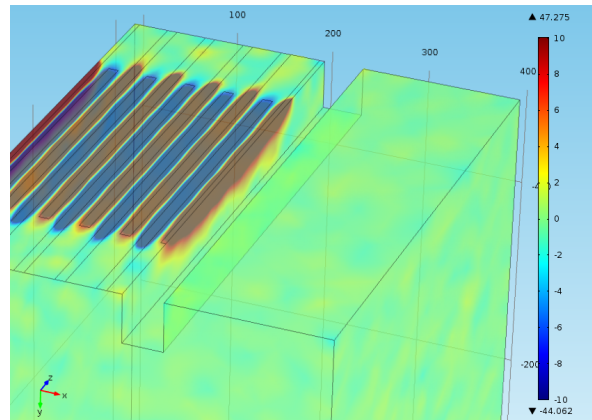
(a) At a depth of $1\mu m$, almost all of the wave leaks.(b) At a depth of $10\mu m$, the wave still leaks.(c) At a depth of $50\mu m$, the wave does not appear to leak.

Figure 5.15: FEA COMSOL simulations of the effect of trench depth on containment of the BG wave. The wave was excited at resonance.

After several iterations of trimming and depth measurement, the PZT4 sensor was laser-etched until it was approximately $94.5\mu m$ while the LiNbO_3 sensor was etched approximately $76.3\mu m$. Table 5.1 shows the parameters used in equation (5.1).

The heat damage around the trenches due to the laser trimmer was kept at a minimum by

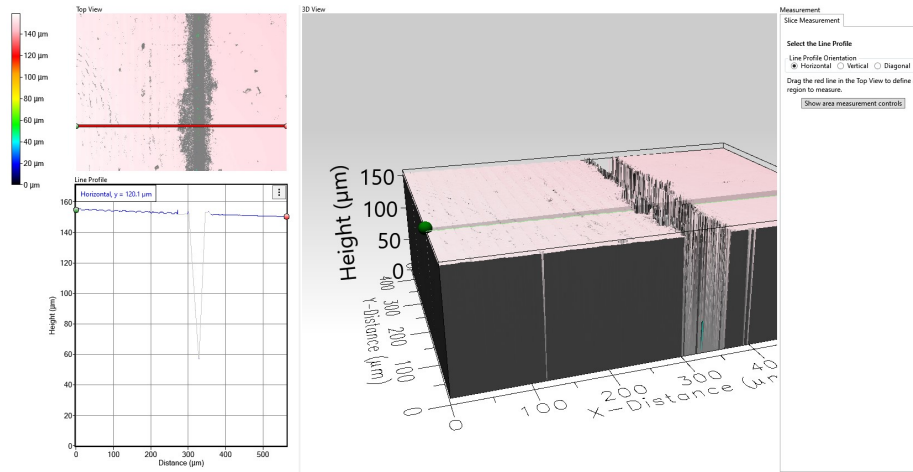


Figure 5.16: Profilometer screenshot during trench depth measurement on the PZT4 sensor. The gray line (lower left plot) represents interpolation by the profilometer software. The blue line indicates true measurement. The bottom of the trench was not captured by the profilometer sensor.

Table 5.1: Laser trimmer settings used and the corresponding depths etched.

Substrate	k ($\mu\text{m}^2/\text{MW}$)	p (MW)	s ($\mu\text{m} / \text{s}$)	f (Hz)	n	d (μm)
PZT4	5.9 (fitted)	0.32	10	10	20	94.5
LiNbO ₃	4.77 (fitted)	0.32	10	10	20	76.3

reducing the pulse repetition frequency and increasing the scan speed. To compensate, the entire scan was repeated 20 times at each trench. Figure 5.17 shows that the heat damage was kept local to the vicinity of the trench. The figure shows the edge of the LiNbO₃ resonator after laser trimming was completed.



Figure 5.17: Localized heat damage near the trench due to the laser trimmer.

5.3 Optical Detection

Two experimental setups were used for the sensor prototype characterization and model validation. The first setup involved using the Polytec UHF-120 Laser Doppler Vibrometer, LDV, to characterize the shear horizontal BG surface wave. Figure 5.18a shows the proposed setup. This technique was also adapted for characterizing the DC response of the sensor. The method was published [1] as a part of this Ph.D. work.

In the following section, the sensor is electrically characterized using a Vector Network Analyzer, VNA. This is a practical approach that resembles a reliable and compact end product. The VNA can measure the S_{11} parameter of the resonant sensor. Figure 5.18b shows the proposed setup for this stage in testing. In both approaches, the sensor pads were directly probed, under the microscope, Figure 5.19.

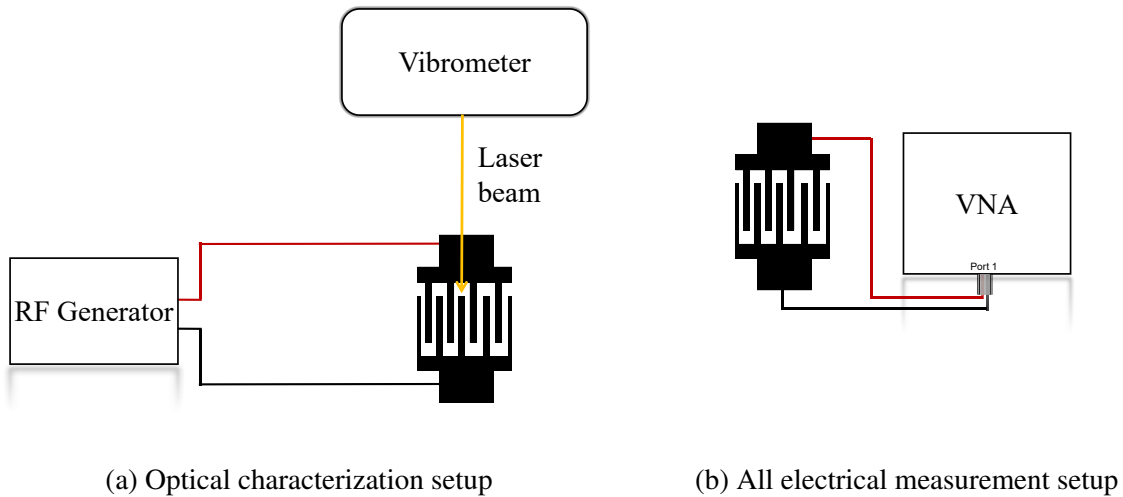


Figure 5.18: Experimental setups

Characterization of surface acoustic waves is integral to SAW technology and research. The most common method involves the use of LDVs to measure out-of-plane vibrations [102, 103].

However, the optical detection of pure shear horizontal waves, SH-SAW, has proven to be a considerable challenge since SH-SAWs often exhibit no out-of-plane components within the wave aperture [99]. Few approaches were found in the literature detailing possible techniques that can be used, however, they included nonstandard test rigs and/or expensive three-dimensional vibrometers.

For SH-SAW on the surface of semi-transparent substrates, such as lithium tantalate, one approach involves observing shear strain-induced polarization variation of a laser beam passing through the substrate [104]. However, this method would not work with opaque substrates, nor would it work with semi-transparent substrates covered with opaque films. It is therefore not applicable for materials such as PZT4.

A second procedure tilts the orientation of the substrate with respect to the incident laser

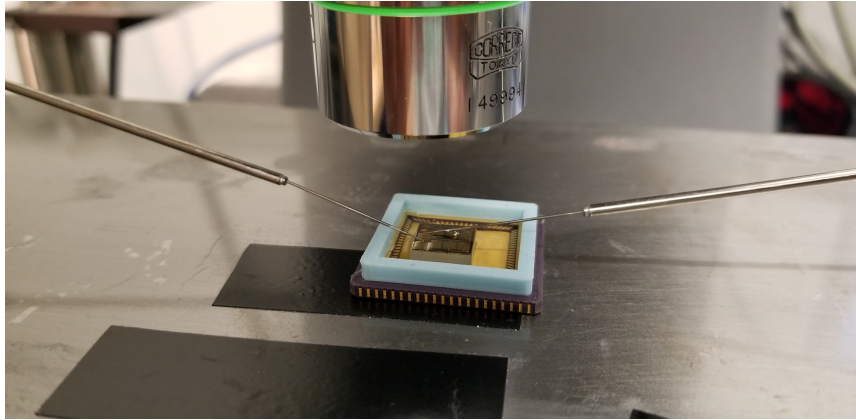


Figure 5.19: LiNbO₃ sensor directly probed, under the microscope.

beam [105, 106]. The beam lands on the edge of an erected structure on the substrate surface and in-plane vibration are captured through the vertical component of the motion using the LDV. This tilt angle creates numerous challenges, increasing the experimental setup complexity. More importantly, it is not applicable for SH-SAWs, since they have few or no erect structures on the substrate surface other than the usually sub-micrometer thin IDT [107, 108]. This is much smaller than the LDV laser spot size, and thus this method is not applicable with SH-SAW.

Another approach involves using more than one laser beams [109, 110] simultaneously. The lasers would be aligned at different angles with respect to the substrate. Therefore, the in-plane and out-of-plane motions are both captured. Conversely, a single laser beam can be used while the angle of the substrate is mechanically changed [111]. These techniques come at a significantly increased experimental setup complexity and cost, and therefore, a simpler solution was required.

A more common approach is full-field vibrometry. These utilize very fast cameras [112] along with 3D digital image correlation (3D-DIC) [113]. The images are processed, and in-plane motion is deduced. For high-frequency applications, a high-speed camera is required with

a framerate considerably larger than the application frequency. This grossly inflates both the complexity and cost of 3D-DIC-based systems.

In this section, we present a novel approach to detect SH-SAWs using traditional 1D vibrometers. The proposed technique is verified using FEA, and it was published [1] with experimental validation.

5.3.1 Optical Characterization of SH Wave

SH waves, such as BG waves, propagate within an aperture, defined by the IDT geometry. The aperture of the wave is confined to the area where the IDT fingers overlap. Typically, the overlap is assumed to be large enough for the wave to be considered invariant along that direction. Beyond this aperture, the behavior is usually not of interest to researchers and engineers.

However, just outside of the wave aperture at the fingertip, there is an area that can be of great value. SH waves act as a boundary load on this area and result in out-of-plane surface strains and deformations. Since this deformation is directly related to the SH wave's time history, it is ripe for exploitation as a measure of the SH wave. We propose to use the LDV to measure those deformations by using an incident laser beam focused on this area.

Figure 5.20a shows a schematic of the proposed experimental configuration. In this section, the origin of the coordinate system is taken on the surface of the substrate directly below the intersection of the finger's mid-line and its tip. The wave propagates along the x-axis, creating a displacement field $u(x, y, z, t)$ along the z-axis. A laser beam, incident along the y-axis, is used to measure the out-of-plane surface deformation $w(0, 0, z_o, t)$ at the point on the z-axis where the deformation reaches a maximum.

Figure 5.20b shows the top view of the IDT, the SH wave, and the allowable locations of the laser beam spot on the substrate. Any of those positions can be used in the proposed detection

has Young's modulus equal to $E = 63$ GPa, and Poisson ratio equal to $\nu = 0.32$. The thickness was set to $H = 3$ mm to match the fabricated substrate. This region was meshed in the Finite Element Model using 60,344 tetrahedral elements with 20,230 mesh vertices.

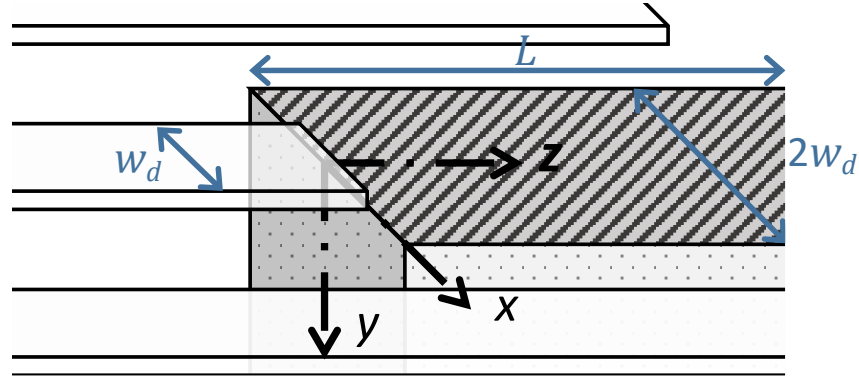


Figure 5.21: Interdigitated electrode (IDT) fingers and the piezoelectric substrate. The highlighted section represents the sector under study.

By assuming a wave frequency that is away from structural resonances of the sector under study, we could analyze its quasi-static (forced) response under the in-plane displacement. The term “quasi-static” should not be confused with the quasi-static approximation of electromagnetic fields. It refers to forced actuation, that is away from any resonances, and thus is slow enough with respect to the wave that it may be considered DC. The in-plane displacement can be written as:

$$u(x, y, 0) = u_o e^{-\zeta \frac{2\pi}{\lambda} y}; \quad -\frac{1}{2}w_d \leq x \leq \frac{1}{2}w_d \quad \& \quad 0 \leq y \leq H. \quad (5.2)$$

This prescribed displacement was applied by the finger to the left face ($z = 0$) of the sector, where $u_o = u_o(t)$ is the instantaneous value of the displacement field at the fingertip, λ is the

wavelength, and ζ is the wave decay rate. To preclude rigid body motions, the bottom plane of the substrate was held fixed at $u(x, H, z) = 0$, while the substrate faces at $y = 0$, $x = \pm w_d$, and $z = L$ were left free.

Figure 5.22 shows the resulting surface deformation under compressive (positive) and tensile (negative) prescribed in-plane displacements of $u_o = \pm 100$ nm, where the wavelength and decay rate were set to $\lambda = 40 \mu\text{m}$ and $\zeta = 0.5$. Varying the prescribed displacement u_o within this range, the relationship between u_o and the peak surface deformation $w_o = w(0, 0, z_o)$ was found to be linear.

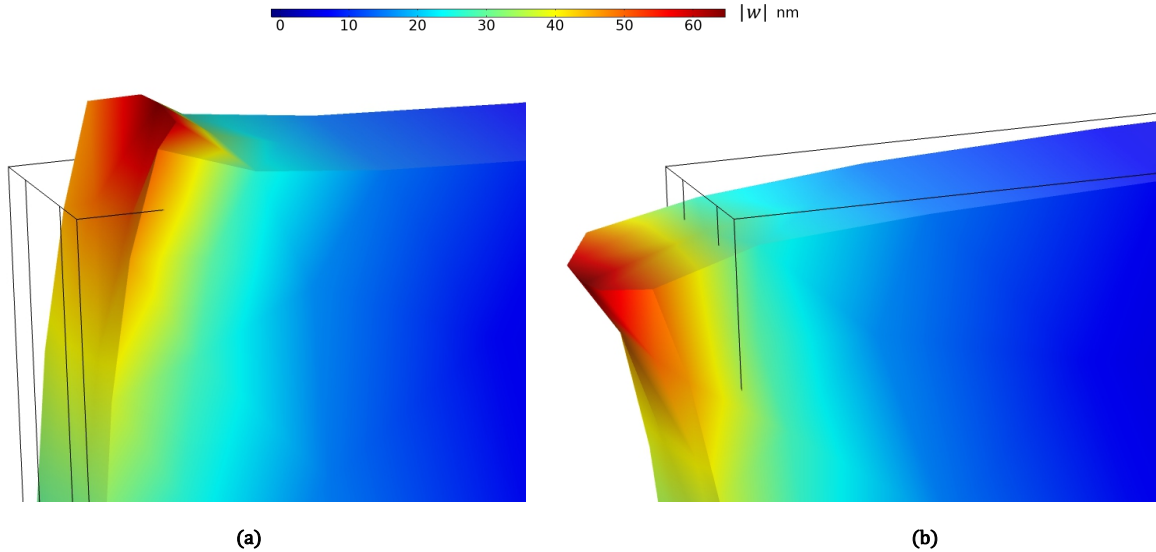


Figure 5.22: Finite element analysis (FEA) of the out-of-plane deformation under **(a)** positive and **(b)** negative in-plane displacement, u .

We investigated the variation in the surface deformation along the mid-line of the finger (z -axis) beyond the tip $w(0, 0, z)$ to determine the maximum point's offset distance from the fingertip z_o and, therefore, the optimal location of the laser spot. Figure 5.23 shows $w(0, 0, z)$ normalized with respect to the maximum in-plane displacement u_o . The out-of-plane displace-

ment decays exponentially away from the fingertip, and therefore, the optimum position to place the laser beam is at the fingertip with $z_o = u_o$.

Most SH waves have sub-micron shear displacements, while the LDV laser spot is typically between 1 and 10 μm . Therefore, the translation of the fingertip would not interrupt measurement, and the laser spot can keep the optimal point z_o within focus. However, achieving optimal positioning would require an infinitesimal spot size. Since the spot size is finite and the deformation field decays exponentially, we propose the location of the spot's indirect “contact” with the fingertip.

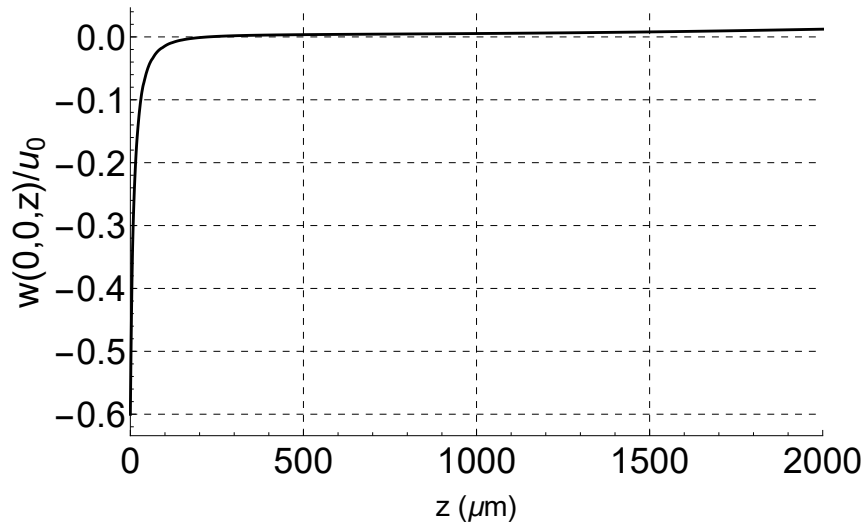


Figure 5.23: The normalized surface deformation simulated by COMSOL.

The decay rate of the deformation field depends on the type of SH-SAW, the substrate properties, and the boundary conditions. This rate determines the degree of the SH wave’s localization to the substrate surface. To determine whether variation in the decay rate may impose further limits on the proposed experimental technique, we compare in Figure 5.24 the normalized deformation along the fingertip mid-line $w(0,0,z)/u_o$ for a range of $\zeta = 0.005$ to 0.5 of decay rates. It was found that the surface deformation resulting from less-confined shear waves decays at a

slower rate. For $\zeta = 0.005$, the surface deformation drops to half value at $z = 370 \mu\text{m}$, which is marked with an asterisk in Figure 5.24. The linear relationship between the peak in-plane displacement u_o and the peak surface deformation w_o also changes from $w_o = -0.6u_o$ at $\zeta = 0.5$ to $w_o = -0.4u_o$ at $\zeta = 0.005$. Highly confined surface waves exhibit a higher deformation ratio α_o but require a smaller laser spot.

As expected, the relationship between in-plane displacement and out-of-plane deformation was found to be independent of Young's modulus and linearly dependent on Poisson's ratio. Specifically and for a decay rate of $\zeta = 0.5$, the deformation ratio varied from $\alpha_o = -0.45$ for $\nu = 0.1$ to $\alpha_o = -0.63$ for $\nu = 0.5$.

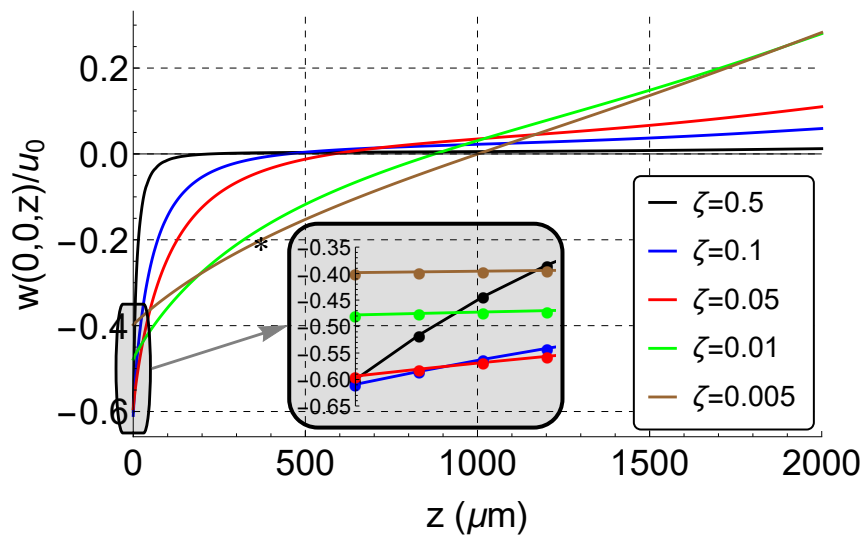


Figure 5.24: Variation in the normalized surface deformation as a function of surface wave confinement.

Validation

Validation of the FEA results was performed on two fronts, both using the microscope-based Polytech MSA-600 Laser Doppler Vibrometer, LDV. First, the LDV laser was used to scan the area in front of one of the fingertips. It was moved sequentially to draw a grid, while the PZT4 BG sensor was actuated at resonance, using direct probing of the IDT under the microscope. Figure 5.25 shows the result of this LDV scan. The outline of the aluminum electrode fingers can be seen in white, while the PZT4 surface is black. The out-of-plane bending is visualized by the Vibrometer software. This is in agreement with both the theoretical and FEA predictions and validates the proposed optical detection approach. For further clarification, Figure 5.26 shows the FEA model of the entire sensor. The color map describes the out-of-plane displacements, and the black square box resembles the portion scanned experimentally in Figure 5.25.

The second validation approach involved comparing the measured linear static response with theoretical predictions. It is discussed in detail in the following sub-section.

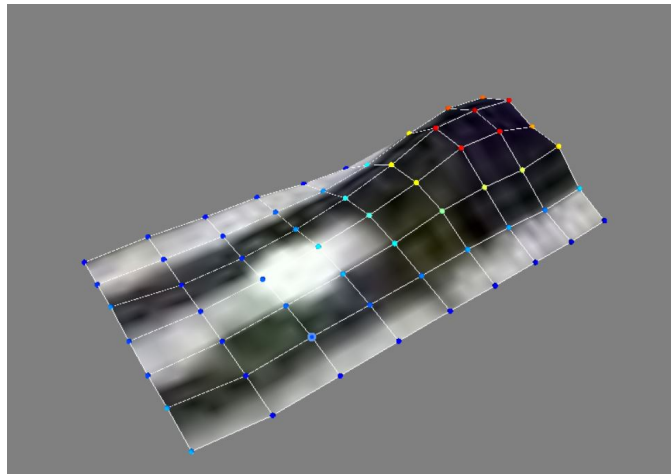


Figure 5.25: Laser Doppler Vibrometer scan, showing the out-of-plane deflection in front of the finger tip, when the PZT4 sensor was excited at resonance.

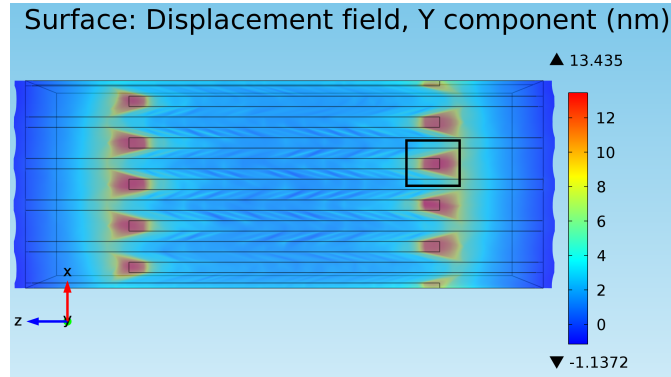


Figure 5.26: FEA of out-of-plane motion in a BGW Sensor. The black box is the area scanned experimentally.

5.3.3 Linear Static Response

Experimental Setup

The proposed technique was deployed to characterize the DC response of the BG resonator. The resonator was placed under the LDV, and direct probing of the IDT under the microscope was again employed to supply the drive voltage $V(t)$. BGWs were excited quasi-statically via a ramp waveform with a frequency of 30 kHz—far away from the 64.8 MHz resonance—using the B&K Precision-4054 function generator.

The behavior of BGWs in PZT4 is well documented [23, 98]. The response to a potential field imposed by applying the voltage waveform $V(t)$ to the substrate surface via an IDT is the displacement field given by [2]:

$$u_o(t) = d_{15}V(t), \quad (5.3)$$

where $d_{15} = 0.496 \text{ nm/V}$ [98] is the shear stress piezoelectric constant. This relationship can be expressed in terms of the measured out-of-plane deformation, such as:

$$w_o(t) = 0.496\alpha_o V(t)(nm). \quad (5.4)$$

Therefore, for a known applied voltage and away from resonance, this equation can be used to identify the parameter α_o . The proposed method was experimentally validated. Figure 5.27 shows the fabricated resonator under the microscope, with the laser position highlighted.



Figure 5.27: A microscopic image of the fabricated IDT for the BG wave resonator, showing the location of the Laser Doppler Vibrometry (LDV) laser spot.

Results

The LDV laser beam spot was located directly in front of the fingertip, Figure 5.27. The sensor was directly probed and excited using a ramp waveform. The measured response to the rising side of the ramp was averaged 30 times. Figure 5.28 compares the experimental results (black circles) to the values predicted by Equation (5.4) (blue line), where the displacement ratio was set to $\alpha_o = -0.56$.

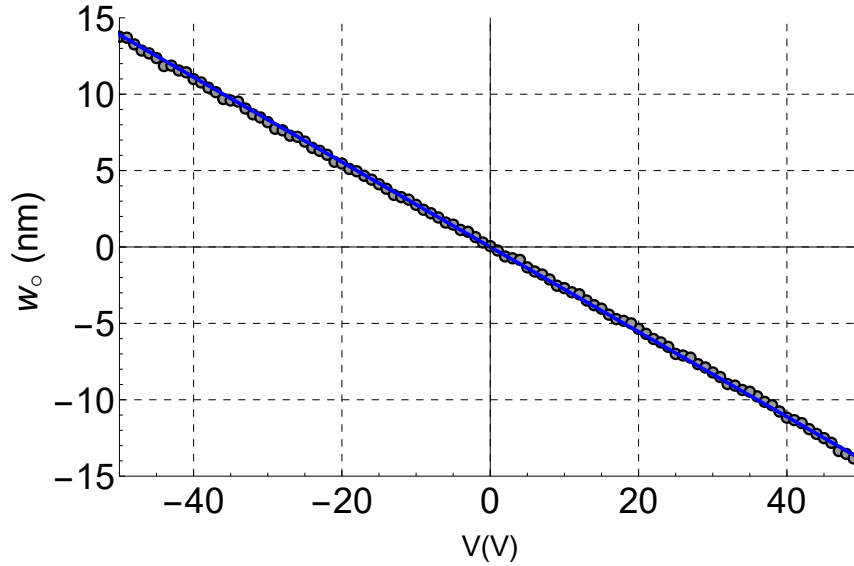


Figure 5.28: Experimental validation for the proposed technique. Experimental measurements are shown as black circles, and the model prediction line is shown as a solid blue line.

Assuming that the Vibrometer-measured displacement represents the average surface deformation within the field illuminated by the spot, Figure 5.24 can be used to estimate the decay rate ζ , given the spot size. In our case, the laser beam spot size was measured as $9\ \mu\text{m}$. A FEM simulation was employed to identify the decay rate ζ , where the average of the deformation ratio α_0 over the initial $9\ \mu\text{m}$ along the z -axis was the same as that evaluated experimentally. Using this method, it was found to be $\zeta = 0.078$.

For the BG-resonator in air, this value is given by equation (4.13), such as $\zeta = 0.007$. The discrepancy in experimental and theoretical values for ζ is attributed to the effect of partial metalization on the surface boundary condition. The IDT's partial metalization of the substrate surface enhances wave confinement to the surface [20], thereby modifying the resonator response in the y -direction. A fully metalized surface will have an effective $r = 0$, equation (4.11), while a bare surface has $r = \frac{\epsilon}{\epsilon^u}$, equation (4.13). Therefore, a partially metalized surface will have $r = \frac{\epsilon}{l\epsilon^u}$,

where ι is a constant that depends on the percentage of surface metalization. Comparing the theoretical and measured values of ζ allows the constant to be experimentally identified as $\iota = 11.4$. This is a reasonable value that is close to the literature [20], and the value is applied in further numerical analysis.

The relationship between displacement and applied voltage was found to be linear for PZT4, as shown in Figure 5.28. This is in agreement with the literature on the small-displacement response of piezoelectric materials [114], thereby further validating the proposed technique. It is also in agreement with the linear relationship, equation (5.4), predicted through FEA. It is important to note that in this experiment, the actuation was kept below 50 V to avoid any electrostrictive nonlinearity.

The proposed technique can, therefore, be used to characterize the instantaneous amplitude of the shear displacement $u_o(t)$ of SH-SAWs. It can also be used to estimate wave confinement ζ to the surface. As a result, it can be used to characterize the time history and frequency response of SH-wave-based sensors and actuators. However, the excitation frequency must be restricted to a frequency range away from the resonances of the substrate sector in front of the fingertip. This restriction does not represent an onerous limitation, since those resonances occur in a much higher frequency range than resonances of the IDT due to the respective sizes of the IDT and the sector.

Moreover, once the displacement ratio α_o has been determined under forced excitation conditions, away from the IDT resonances, the IDT can be excited at resonance in order to determine its frequency response and identify its quality factor. The quality factor can be calculated as the ratio of the response at resonance to the static response or using the half-power bandwidth method.

5.4 Electrical Detection

5.4.1 Experimental Setup

The deposition of any medium-under-test on top of the sensor impedes optical detection. Therefore, the use of Vector Network Analyzers, VNAs, provides an electrical characterization measurement and can be used to test the sensor operation. VNAs can identify key parameters, called the S-Parameters, about high-frequency filters and resonators.

For a 1-port resonator, only the S_{11} exists. It defines the reflectivity of the resonator as a function of frequency. Since the BG sensor is designed as a 1-port resonator, therefore S_{11} is enough to fully characterize the sensor. Moreover, the only modes allowed inside the resonator are resonant modes and, thus, the sensor is expected to reflect all frequencies except resonant ones.

Figure 5.29 shows the experimental setup used. The sensor was characterized electrically using the Agilent E5061B Vector Network Analyzer, VNA. The power level of the VNA was set to 10 dBm, and the intermediate frequency bandwidth, IF-BW, was set to 30 kHz. Each measurement was averaged 10 times. Port 1 of the VNA was directly connected to the probe station using a short coaxial cable. The probes landed directly on the sensor ports, Figures 5.18b and 5.19. The probe station was operated under a microscope and was placed above two-dimensional motorized positioners or micromanipulators. The microscope-positioner system appearing in Figure 5.29 is a subsystem of the Polytech MSA-600 Laser Doppler Vibrometer.

The calibration process was performed to compensate for the probes and cables. Calibration also compensates for any source mismatch, directivity, or cross-talk. Mismatch refers to impedance mismatch between the VNA and cables, cables and probes, or probes and the sensor. Reflections due to the probes are called directivity, and interference between ports is referred to

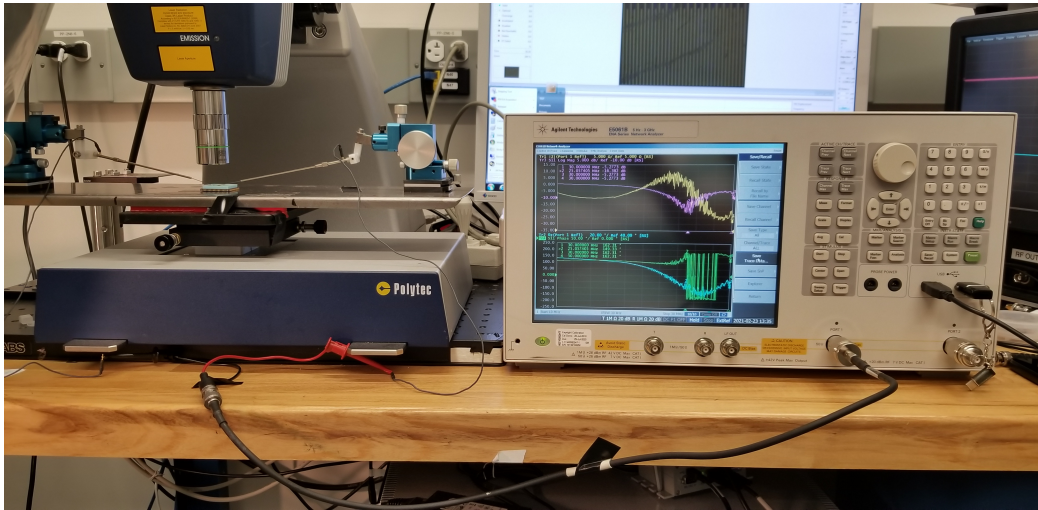


Figure 5.29: Experimental setup using the Agilent E5061B VNA.

as cross-talk. Calibration can track the reflectivity as frequency changes within the defined start and stop frequencies. Therefore, measurement is only valid within this band. Changing the start and stop frequencies, the number of points, or the IF-Bandwidth of the VNA voids the current calibration and, thus, warrants a new calibration step.

Calibration was performed in three stages, as shown in Figure 5.30. The first stage was the “open” calibration, Figure 5.30a. The probes were positioned in a similar orientation to when measurement would take place but left unconnected or electrically open. Then, the “short” calibration was performed, Figure 5.30b, similarly to the open case, but after touching the probe tips to create an electrical short circuit. Lastly, a “load” calibration step was executed, Figure, 5.30c, by placing a $50\ \Omega$ load between the probes. This step, which is not necessary for S_{11} measurements, is still recommended to compensate for all mismatch errors. All the cables used were rated as $50\ \Omega$.

The VNA can also measure the Z-Parameters, specifically Z_{11} for a 1-port network resonator. Z_{11} measurements are redundant to S_{11} measurements, as the transformation is well known, and

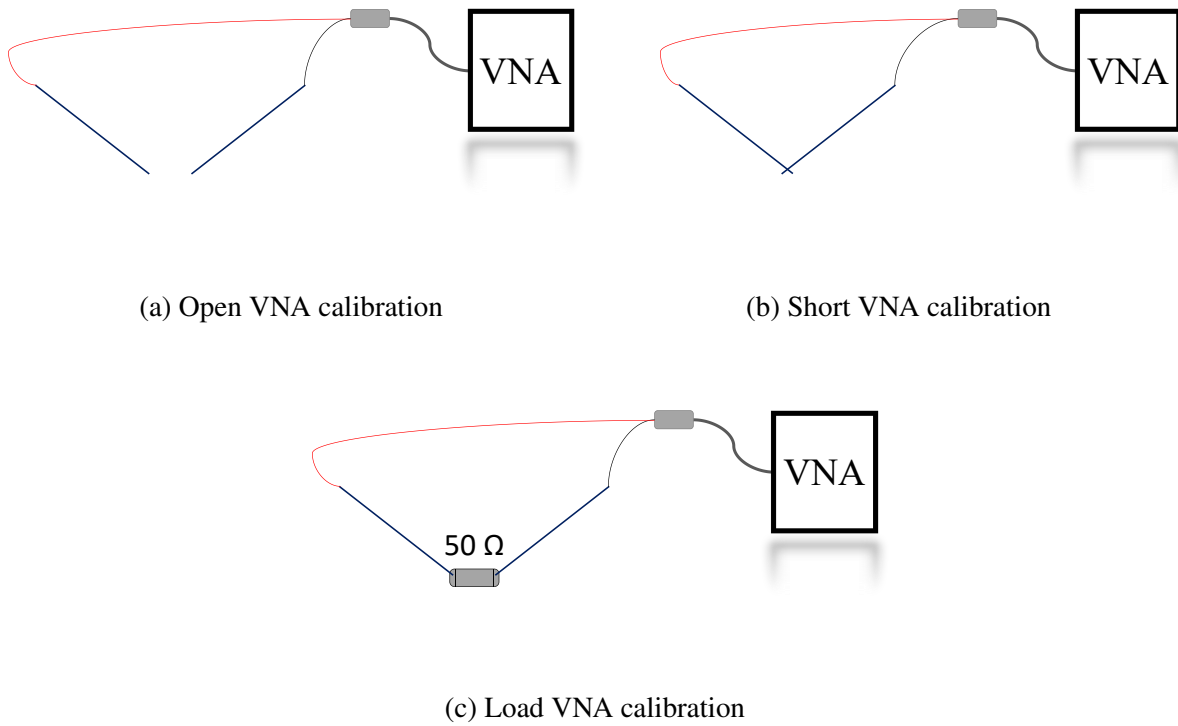


Figure 5.30: Measurement calibration stages for the vector network analyzer.

is given by [115]:

$$\mathbf{Z}_{11} = Z_{11}/\theta_z = \mathbf{Z}_o \frac{1 + S_{11}/\theta_s}{1 - S_{11}/\theta_s} \quad (5.5)$$

where $\mathbf{Z}_o = 50 \Omega$. However, a parasitic capacitance or inductance can cause the Z_{11} measurement to appear deformed, with a shifted peak frequency from its resonance.

5.4.2 Modeling of S-Parameters

The scattering parameter S_{11} measures how much of the signal is reflected as a function of frequency. From equation (5.5), it is a function of the impedance mismatch and can be written

as:

$$S_{11} = \frac{Z_{11} - Z_o}{Z_{11} + Z_o}$$

The resonator can thus be modeled using an R-L-C circuit however, the model must also account for the parasitic capacitance of the IDT, Figure 5.31. This can be modeled, such as:

$$Z_{11} = \frac{X_c Z}{X_c - Z} \quad (5.6)$$

where $X_c = (2\pi f c_p)^{-1}$, c_p is the parasitic capacitance, $Z = R + (2\pi f c)^{-1} + 2\pi f \ell$, and R , ℓ , and c are the equivalent RLC parameters of the resonator. The RLC parameters were extracted from the experimental measurements, following [116]. However, it is important to note that the parasitic capacitance varies when the medium-under-test is changed, and thus the analysis requires a more involved approach.

The parasitic capacitance of the IDT is affected by the permittivities of both the substrate and the medium-under-test. Since the IDT thickness is usually very small in comparison to its length, width, and gap, the capacitor is considered to be dominated by the fringing effects [117]. Therefore, the effective permittivity of the parasitic capacitor can be approximated as the average of that of the piezoelectric and the medium-under-test. The ratio of the parasitic capacitance of a specific medium-under-test, c_{p_m} , to that when no medium is present, c_{p_o} , can thus be approximated, such as:

$$\frac{c_{p_m}}{c_{p_o}} = \frac{\epsilon + \epsilon^u}{\epsilon + 1}$$

Therefore, the theoretical S_{11} response can be modeled, with only three experimentally identifiable unknowns, namely f_o , $S_{11}(f_o)$, and c_{p_o} , where f_o is the natural frequency of the resonator. The value of f_o can be obtained from the theoretically modeled values, Figures 7.5 or 7.6, and the profile of $S_{11}(f_o)$ can be characterized by the quality factor, Q . In this work, Q was initially set to 10, and this was found to agree with the experimentally measured value later on. It is important

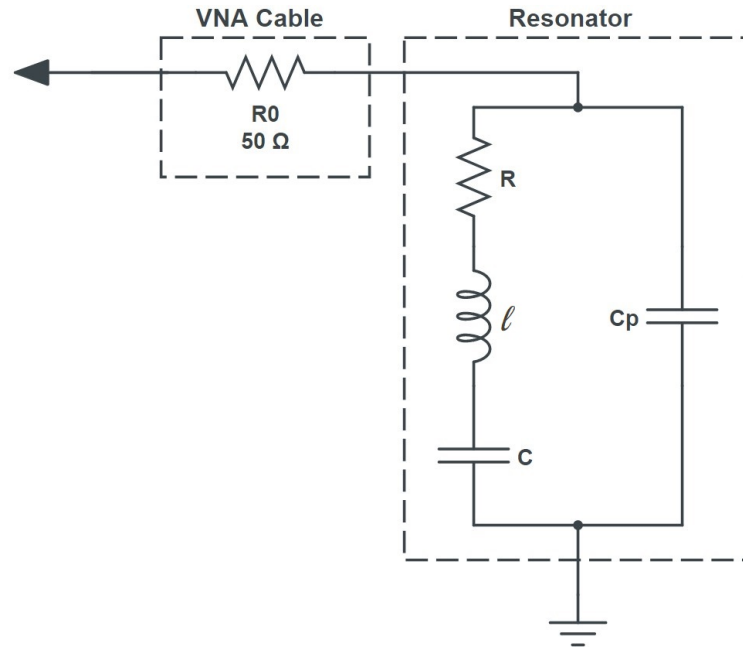


Figure 5.31: RLC equivalent circuit for the IDT BG resonator and the VNA cable.

to note that the value of Q is low compared to the literature [118, 119] due to challenges in the last fabrication step of laser patterning. The trench depth directly affects the edge reflectivity, and thus the quality factor. Therefore, to improve the quality factor, the depth of the trench needs to be increased.

The values of f_o and Q can then be used to identify the RLC parameters [116]. Next, the parasitic capacitance is identified by fitting the experimental and theoretical S_{11} responses.

The effect of the media-under-test on the parasitic capacitance enhances the observed sensitivity of the sensor and thus is desirable. However, on its own and without the BGW equations, it is not nearly sufficient to explain the experimentally observed frequency shifts under different media-under-test.

5.5 Summary

In this chapter, the sensor prototypes were presented. Two substrates were chosen for the sensor, PZT4 and LiNbO_3 based on the shear coupling coefficients. The fabrication process, including post-processing, was presented in detail, and the process recipe was provided.

Additionally, the experimental setups and techniques used to characterize the sensor were discussed. An novel optical detection scheme for the BG wave using a 1D Laser Doppler Vibrometer was developed and the method was published. Moreover, the electrical detection scheme using the VNA was outlined to allow for the validation of the permittivity sensor.

Chapter 6

Non-Resonant Excitation²

In this chapter, the mechanism of excitation for the BG wave is first discussed, along with the different sources of damping. Then the linear forced DC response of the BG wave sensor is investigated, followed by the nonlinear response. Finally, the numerical and experimental results are presented and discussed.

6.1 Excitation and Damping Mechanisms

6.1.1 Charge Excitation

Excitation of the BG wave is accomplished using the IDT. This can be modeled through the charge distribution created by the IDT geometry and the potential difference applied between its electrodes. The governing equations for the BG wave, equations (2.9) and (2.10), can be

²This chapter is adapted from **Elhady, Alaa**, M. Basha, and E. M. Abdel-Rahman, “Analysis of tunable Bleustein-Gulyaev permittivity sensors,” *Journal of Applied Physics*, vol. 129, no. 16, p. 164501, 2021

rewritten for a non-zero net charge, such as:

$$\rho \ddot{u}_z = \frac{\partial T_{xz}}{\partial x} + \frac{\partial T_{yz}}{\partial y} \quad (6.1)$$

$$\nabla \cdot \mathbf{D} = \zeta \quad (6.2)$$

where ζ is the charge distribution density. The free charges term, ζ , is typically assumed to be negligible. However, this assumption is not valid in our case due to the IDT excitation of BG waves on the surface. The electrodes of the IDT can be used to apply a DC voltage distribution $V(x, y)$ to the piezoelectric substrate that results in a charge distribution with the steady-state form:

$$\zeta(x, y) = \epsilon_T \beta_n^2 V(x, y) \quad (6.3)$$

where $\epsilon_T = \epsilon + \frac{e^2}{G}$ is the zero-stress permittivity of the piezoelectric and β_n^2 is a constant dependent on the IDT geometry and the substrate losses.

6.1.2 Damping

Since the BG wave couples acoustic and electromagnetic fields, it will suffer two types of damping. Dielectric losses can be modeled by the conductivity, σ , while mechanical losses can be lumped into the viscous damping constant, c . Therefore, the governing equations, equations (2.9) and (2.10), can be further expanded, such as:

$$\rho \ddot{u}_z + c \dot{u}_z = \frac{\partial T_{xz}}{\partial x} + \frac{\partial T_{yz}}{\partial y} \quad (6.4)$$

$$\nabla \cdot \mathbf{D} = \zeta - \sigma \int \nabla \cdot \mathbf{E} dt \quad (6.5)$$

Substituting with nonlinear constitutive equations (3.8)–(3.11) into equations (6.4) and (6.5),

the governing system of equations is obtained, such as:

$$\rho \ddot{u}_z = G \nabla^2 u_z - e \nabla \cdot \mathbf{E} + ML_1(E_x, E_y) \quad (6.6)$$

$$\zeta - \sigma \int \nabla \cdot \mathbf{E} dt = e \nabla^2 u_z + \epsilon \nabla \cdot \mathbf{E} + ML_2(u_z, E_x, E_y) \quad (6.7)$$

Since the time constant of the electromagnetic component of the wave, appearing in equation (3.16), is five orders-of-magnitude smaller than that of the elastic component, the quasistatic approximation, section 2.3, is assumed. Substituting with equation (2.43) in equations (6.6) and (6.7) and accounting for the mechanical viscous damping, the governing equations reduce to:

$$\rho \ddot{u}_z + c \dot{u}_z = G \nabla^2 u_z + e \nabla^2 \psi + MGL_1(\psi) \quad (6.8)$$

$$\zeta + \sigma \int \nabla^2 \psi dt = e \nabla^2 u_z - \epsilon \nabla^2 \psi + ML_2(u_z, \psi) \quad (6.9)$$

6.2 Linear Static Response

The linear static response is evaluated by dropping the electrostriction operators, setting the time derivative and accumulation terms, and substituting the charge by equation (6.3), thereby reducing the equilibrium equations, equations (6.8) and (6.9), to:

$$G \nabla^2 u_z + e \nabla^2 \psi = 0 \quad (6.10)$$

$$e \nabla^2 u_z - \epsilon \nabla^2 \psi = \epsilon_T \beta_n^2 V \quad (6.11)$$

Adding and subtracting equations (6.10) and (6.11), results in:

$$\nabla^2 u_z = \frac{e}{G} \beta_n^2 V \quad (6.12)$$

$$\nabla^2 \psi = -\beta_n^2 V \quad (6.13)$$

Summing these two equations results in a Laplace equation of the form:

$$\nabla^2(u_z + \frac{e}{G}\psi) = 0 \quad (6.14)$$

The mode shapes from (4.19) for both the displacement and the potential fields are substituted, to observe that the equation has two solutions, the trivial solution $u_z = 0$ and $\psi = 0$ when $k_n = \kappa_n$ and

$$u_z = -\frac{e}{G}\psi$$

which means that the displacement field is enslaved to the potential field and the system of equations (6.12) and (6.13) reduces to equation (6.13) only.

The voltage distribution imposed by the IDT can be approximated as a first order approximation, such as:

$$V(x, y) = V_o e^{-\kappa_n y} \cos(k_n x) \quad (6.15)$$

Since the homogeneous solution of equation (6.13) is trivial, the particular solution is obtained by substituting the form:

$$\psi(x, y) = \psi_o e^{-\kappa_n y} \cos(k_n x)$$

which yields:

$$(\kappa_n^2 - k_n^2)\psi_o = -\beta_n^2 V_o \quad (6.16)$$

We set $\beta_n^2 = k_n^2 - \kappa_n^2$ and $\psi_o = V_o$, to write the field response as:

$$\psi(x, y) = V(x, y) \quad (6.17)$$

$$u_z(x, y) = -\frac{e}{G} V_o e^{-\kappa_n y} \cos(k_n x) \quad (6.18)$$

6.3 Nonlinear Static Response

We can observe the forced DC nonlinear response to the charge distribution, by setting the time derivative and accumulation terms in equations (6.8) and (6.9) equal to zero to obtain:

$$G \nabla^2 u_z + e \nabla^2 \psi + MGL_1(\psi) = 0 \quad (6.19)$$

$$e \nabla^2 u_z - \epsilon \nabla^2 \psi + ML_2(u_z, \psi) = \zeta \quad (6.20)$$

Similarly, rearranging equations (6.19) and (6.20), and using equation (6.3) yields:

$$\nabla^2 u_z + \frac{\epsilon M}{\epsilon_T} L_1(\psi) + \frac{eM}{G\epsilon_T} L_2(u_z, \psi) = \frac{e}{G} \beta_n^2 V \quad (6.21)$$

$$\nabla^2 \psi + \frac{eM}{\epsilon_T} L_1(\psi) - \frac{M}{\epsilon_T} L_2(u_z, \psi) = -\beta_n^2 V \quad (6.22)$$

We follow the nondimensionalization approach defined in section 2.4 and replace the differential operator L_i with the nondimensional version \hat{L}_i . Introducing those variables into equations (6.19) and (6.20), yields:

$$\nabla^2 u_z + \nabla^2 \psi + \hat{M}L_1(\psi) = 0 \quad (6.23)$$

$$\nabla^2 u_z - \frac{G\epsilon}{e^2} \nabla^2 \psi + \hat{M}L_{2A}(u_z, \psi) + \hat{M}^2 L_{2B}(u_z, \psi) = \left(1 + \frac{G\epsilon}{e^2}\right) \hat{\zeta} \quad (6.24)$$

where $\hat{M} = \frac{MG}{eL}$ and $\hat{\zeta} = \zeta \frac{l^2}{\epsilon_T}$. The hats on the nondimensional nonlinear operators are dropped for convenience.

This system of partial differential equations can be converted into a system of algebraic equations using the Galerkin residuals method [120]. First, the system states are expanded in terms of the unforced mode shapes, then the residuals are evaluated and set to vanish. The resulting system of algebraic equations is solved numerically. Therefore, the displacement and potential

fields in terms of the linear mode shapes $\phi_n(x, y)$ are given by:

$$u_z(x, y) = \sum_{n=1}^N q_{sn} \phi_n(x, y) \quad (6.25)$$

$$\psi(x, y) = \sum_{n=1}^N p_{sn} \phi_n(x, y) \quad (6.26)$$

where q_{sn} and p_{sn} are the modal coordinates and N is the number of modes.

The voltage distribution imposed on the substrate by the IDT can be approximated by a Fourier series in terms of the mode shapes:

$$V(x, y) = V_o \sum_{n=1}^N C_{(2n-1)} e^{-\kappa(2n-1)y} \cos((2n-1)m\pi x) \quad (6.27)$$

where V_o is the DC voltage applied to the electrodes, C_{2n-1} are empirically fitted constants. The constants for the first four terms are listed in Table 6.1, and the resulting empirical voltage distribution at the surface is shown in Figure 6.1. The x axis is normalized with respect to the wavelength.

Table 6.1: Coefficients of the empirical fit for the spatial voltage distribution.

$C_1 = 1.115$	$C_5 = -0.019$
$C_3 = -0.103$	$C_7 = 0.005$

Substituting the modal expansion of equations (6.25) and (6.26) into equations (6.23) and (6.24), multiplying the result by the individual mode shapes, and setting the integral over the

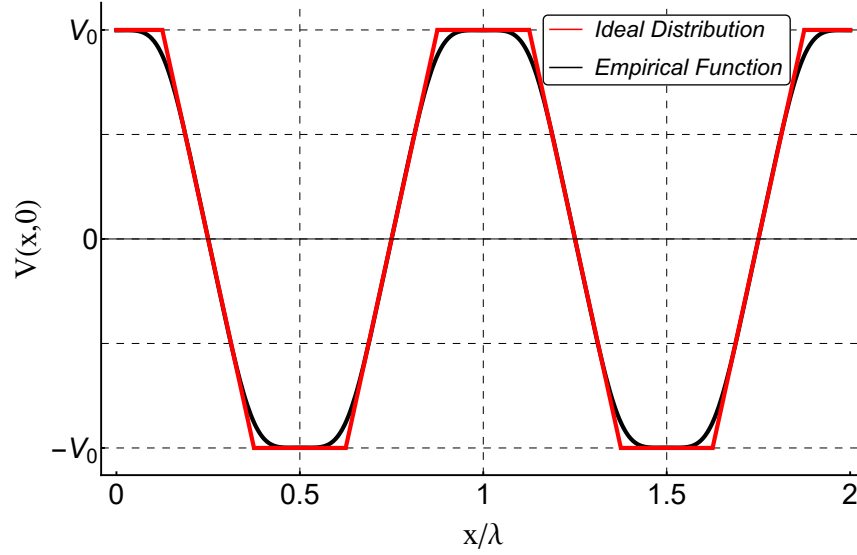


Figure 6.1: Comparison of the ideal voltage distribution, generated by the geometric shape of the IDT, and the empirical function $V(x, y)$ used to represent it.

domain equal to zero, such as:

$$\int_0^{\infty} \int_0^1 \phi_n \left(q_{sn} \nabla^2(\phi_n(x, y)) + p_{sn} \nabla^2(\phi_n(x, y)) + \hat{M} L_1(p_{sn} \phi_n(x, y)) \right) dx dy = 0 \quad (6.28)$$

$$\int_0^{\infty} \int_0^1 \phi_n \left(q_{sn} \nabla^2(\phi_n(x, y)) - \frac{G\epsilon}{e^2} p_{sn} \nabla^2(\phi_n(x, y)) + \hat{M} L_{2A}(q_{sn} \phi_n(x, y), p_{sn} \phi_n(x, y)) \right. \\ \left. + \hat{M}^2 L_{2B}(q_{sn} \phi_n(x, y), p_{sn} \phi_n(x, y)) - \left(1 + \frac{G\epsilon}{e^2}\right) \zeta \right) dx dy = 0 \quad (6.29)$$

where $n = 1, 2, \dots, N$, yields a system of nonlinear algebraic equations, equations (C.7) to (C.14), in Appendix C.2.

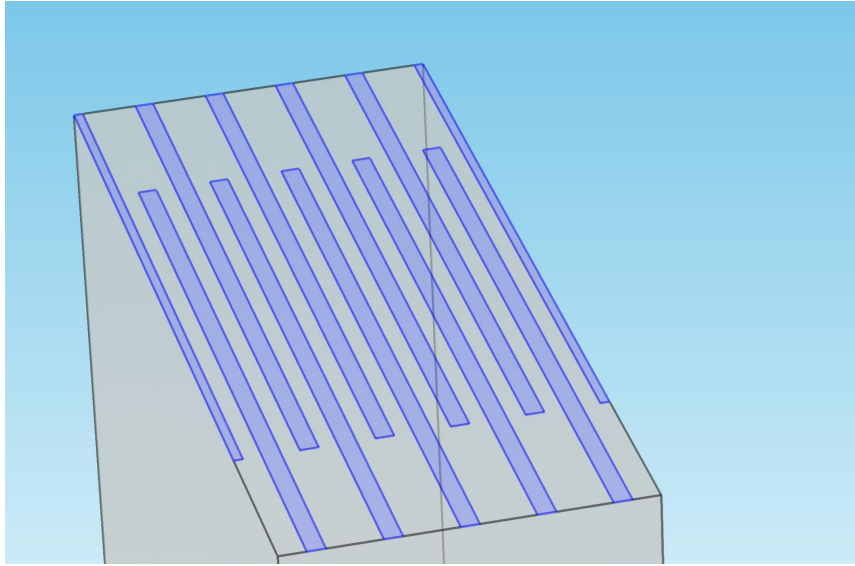


Figure 6.2: FEA model geometry showing the PZT4 box, and a 2D metal surface with the IDT shape.

6.4 Simulation Results

6.4.1 Finite Element Model

The sensor was fabricated using a shear-poled Lead Zirconate Titanate Navy Type-I (PZT4) substrate [98] selected because of its high shear piezoelectric constant ($e = 12.7$) and high electromechanical coupling coefficient [99]: $\frac{e^2}{e^2 + G\epsilon} = 0.71$ to promote efficient wave generation, where the shear modulus is $G = 25.6$ GPa and the zero-strain relative permittivity is $\epsilon_r = 718$. The COMSOL Finite Element Model (FEM), Figure 6.2, was created to validate the linear sensor model. A DC voltage of $V_0 = 100$ V was applied to the IDT electrodes, and the static response was calculated. The potential field was grounded, and the displacement field was set to zero at the bottom surface of the substrate.

Figure 6.3 shows the potential $\psi(x, 0, z)$ and displacement $u_z(x, 0, z)$ field distributions on the top surface. The (spatial) peak-to-peak displacement was 49.7 nm realized in the sensor aperture, which is in close agreement with that predicted by the static model as per equation (6.18):

$$(u_z)_{pp} = \frac{e}{G} V_o = 49.6 \text{ nm}$$

thereby validating the linear model.

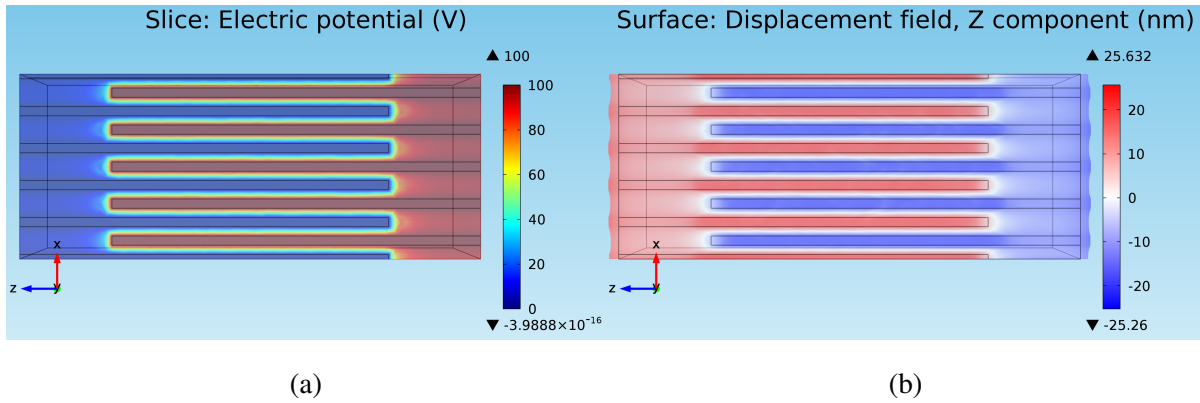


Figure 6.3: FEM predicted potential and displacement field distributions under 100 V applied across the IDT electrodes. (a) Electric potential and (b) displacement field distribution.

6.4.2 Reduced-Order Model

The system of nonlinear algebraic equations, equations (C.7) to (C.14) represents a reduced-order model of the static response. It was solved numerically using a Mathematica algebraic solver [121] that implements the secant method to search for the roots, static equilibria.

In this work, the nonlinear electrostriction coefficient of PZT4 was set to $M = 12.7 \times 10^{-18} \text{ m}^2/\text{V}^2$. This value was experimentally identified and is similar to values reported by others in the literature [122].

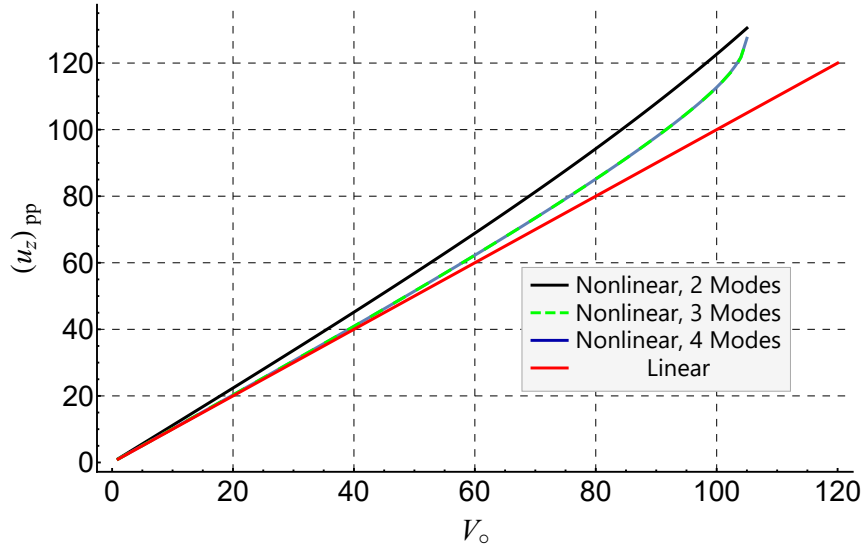


Figure 6.4: Convergence plots showing the peak-to-peak displacement $u_{z(pp)}$ as a function of electrode voltage V_0 for PZT4 with air as the medium-under-test: linear static response (red), nonlinear static response using 2 modes (black), 3 modes (green), and 4 modes (blue).

Convergence analysis was carried out to determine the number of modes N required for a convergent solution. Figure 6.4 compares the nondimensional peak-to-peak static displacement at the substrate surface $(u_z)_{pp}$, when the upper half-space was occupied by air, obtained from two, three, and four-mode reduced-order models as functions of the DC voltage V_0 between the IDT electrodes. We find that the difference between three- and four-mode expansions is negligible, less than 1%. Therefore, we adopt four-mode ($N = 4$) approximations of the potential and displacement fields.

Differences between the linear and nonlinear models are negligible up to 50 V, Figure 6.4. Beyond that point, a softening electrostrictive nonlinearity predicts progressively larger displacements, compared to those predicted by the linear model, as the voltage increases.

Accounting for electrostriction in the nonlinear model allows us also to elucidate the impact

of the medium in the upper half-space, represented by permittivity ratio r , on the electric and displacement fields. The thickness of the medium-under-test was assumed to be more than several wavelengths λ and, therefore, can be approximated to occupy the upper half-space.

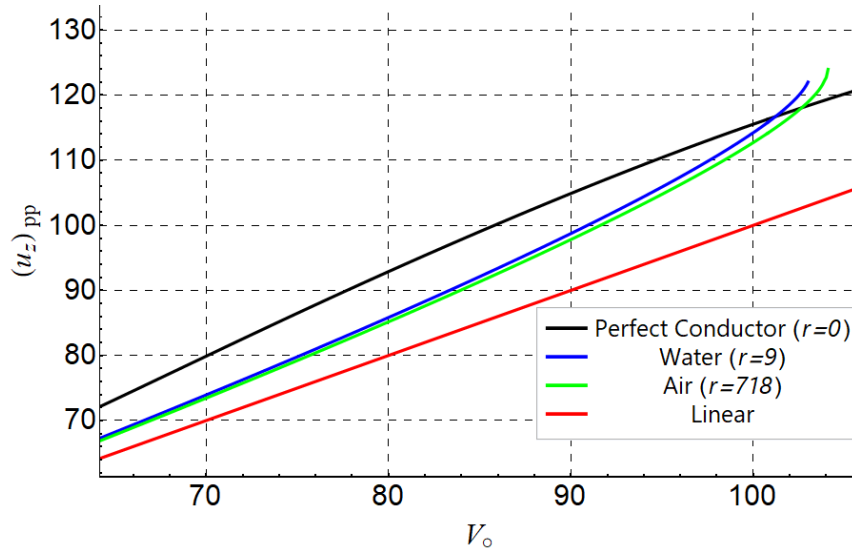


Figure 6.5: The peak-to-peak displacement $u_{z(pp)}$ as a function of electrode voltage V_0 for a PZT4 sensor with the medium-under-test set as air (green), deionized water (blue), and with a metallized surface (black). The linear solution (red) is shown for reference.

Figure 6.5 shows the static displacement $(u_z)_{pp}$ under higher applied voltages, where the impact of the electrostriction nonlinearity is significant. It compares the static response of the PZT4 substrate when the medium-under-test is air $r = 718$ (green line) or deionized water $r = 9$ (blue line) to the case when the substrate surface is covered with a perfect conductor $r = 0$ (black line). The latter case corresponds to the metallization of the substrate surface. It also represents the limiting case for a conductive liquid medium-under-test as $\epsilon^u \rightarrow \infty$. The linear response is also shown as a red line for reference.

Metallization shields the wave in the substrate from the medium in the upper half-space,

thereby disabling the sensor. Since metallization provides better wave confinement to the substrate surface, electrostriction results in a larger displacement for a given voltage compared to the linear case, as shown in Figure 6.5. For dielectric media with finite permittivity $\epsilon_o < \epsilon^u \ll \infty$, the displacement field is limited between a lower bound when the upper-medium is a vacuum (or air) and the metallization case. Further, no solution was obtained for voltage values in excess of 104 V for media with finite permittivity. The Figure also shows that perturbations in the permittivity of the upper-half-space result in larger changes in the displacement field at higher DC voltages. Therefore, the sensor is more sensitive under a higher DC bias.

We employed a numerical solver based on the pseudo-arc-length method [123] to find the equilibria of the PZT4 sensor with deionized water serving as the medium-under-test. This is the relevant medium for biological applications, such as blood plasma. Figure 6.6 shows the peak-to-peak displacement $(u_z)_{pp}$ at the substrate surface ($y = 0$). Stable equilibria are shown in solid black lines, and unstable equilibria are shown in dashed red lines. The stability of each equilibrium point was determined by numerically evaluating the eigenvalues corresponding to it.

The branch of equilibria passing by the origin, corresponding to those shown in Figures 6.4 and 6.5, extends across both positive and negative polarity. The continuation solver revealed that it ends at two turning points $V_o = \pm 103.1$ V where it meets another branch of larger unstable equilibria. Beyond these bifurcation points ($V_o > 103.1$ V), no equilibria exist.

The quadratic electrostriction nonlinearity results in response asymmetry since any electric field yields a constrictive displacement regardless of its polarity. While this asymmetry is negligible along the primary branch, it is more pronounced along the larger unstable branch, with the positive polarity side of that branch evincing larger displacements than those of the negative polarity side.

The equilibria lose stability for voltage values larger than ± 81 V. To explore the underlying

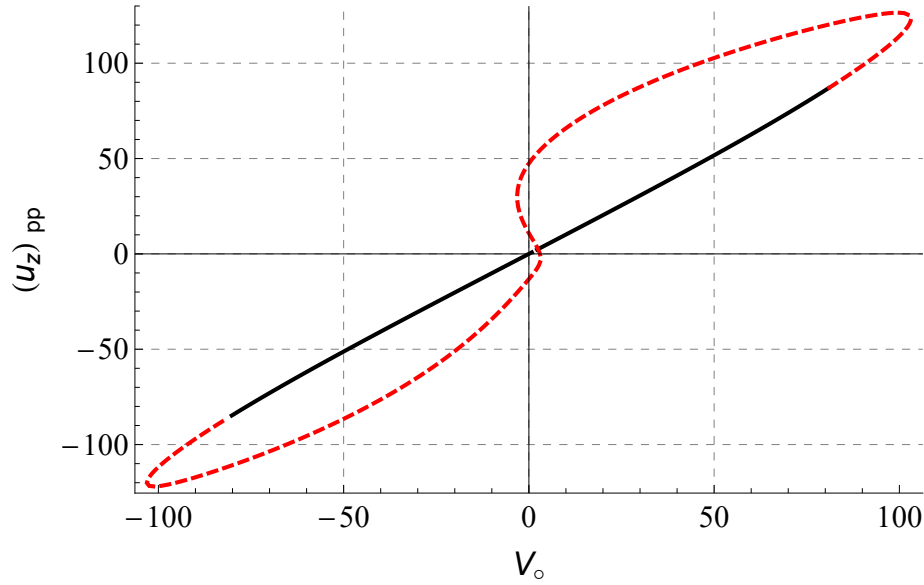


Figure 6.6: The peak-to-peak displacement $u_{z(pp)}$ as a function of electrode voltage V_o for the PZT4 sensor with deionized water as a medium-under-test. Stable equilibria are shown as solid black lines, and unstable equilibria are shown as dashed red lines.

reasons, we linearized the discretized equations of motion, corresponding to equations (6.8) and (6.9), around each equilibrium point and evaluated the linear system eigenvalues Λ . The conductivity of PZT4 was set to $\sigma = 0.0517$ [124] and the mechanical quality factor was set to $Q = 300$. The eigenvalues are shown in the complex plane in Figure 6.7. The arrows appearing along the eigenvalue traces indicate the direction of increasing voltage.

Along the primary branch of equilibria, two pairs of complex conjugate eigenvalues exit the left-half of the complex plane simultaneously at ± 81 V. A pair of complex eigenvalues, corresponding to the fourth mode $\phi_4(x, y)$, crosses the imaginary axis transversely while another pair of complex eigenvalues, corresponding to the third mode $\phi_3(x, y)$, exits the complex plane via $-\infty$ and re-enters via $+\infty$. The behavior of the latter pair explains the reason underlying loss of stability: at this voltage, the effective permittivity of the third mode $p_{3d}(t)$ vanishes, leading

to electrical breakdown. These points, therefore, represent the limits of the sensor operating range. We note that omitting the third and fourth modes from the model would have led to false conclusions about the sensor operating range.

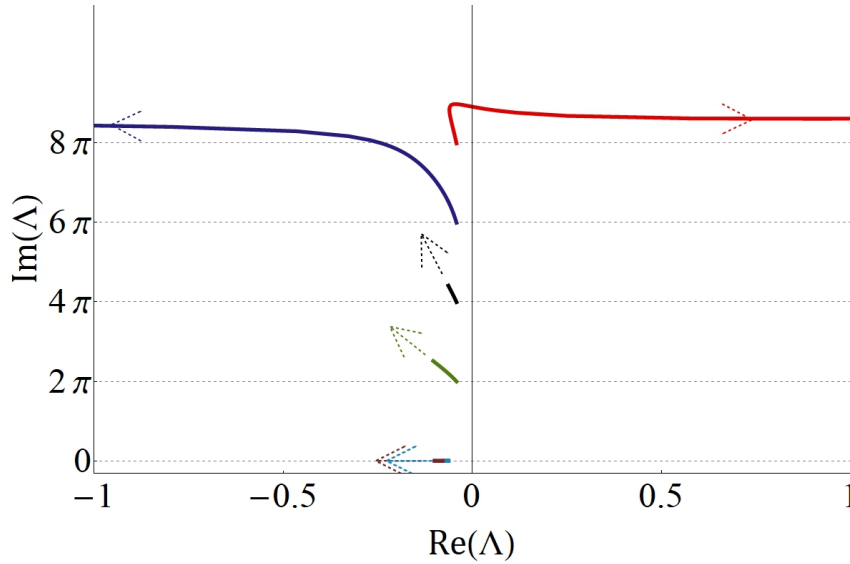


Figure 6.7: The eigenvalues of the equilibria appearing along the lower branch in the voltage range $[0, 85]$ V for a PZT4 sensor with deionized water as the medium-under-test.

As indicated by equation (4.13), lower permittivity samples (larger r) reduce the field confinement to the surface, thereby reducing the electrostrictive contribution to the displacement field. To investigate the impact of field confinement on the sensor response, we show in Figure 6.8 the peak-to-peak displacement $(u_z)_{pp}$ as a function of applied voltage V_o for an air sample, which represents the limiting case for relative permittivity $r_{max} = 718$.

Compared to the displacement field for deionized water, Figure 6.6, it can be seen that the lower permittivity of air leads to a smaller displacement field (see also Figure 6.5). While the sensor also loses stability via voltage breakdown, it occurs at a higher voltage $V_o = \pm 92$ V and the turning points along the primary branch appear at a higher voltage $V_o = 104$ V. In addition,

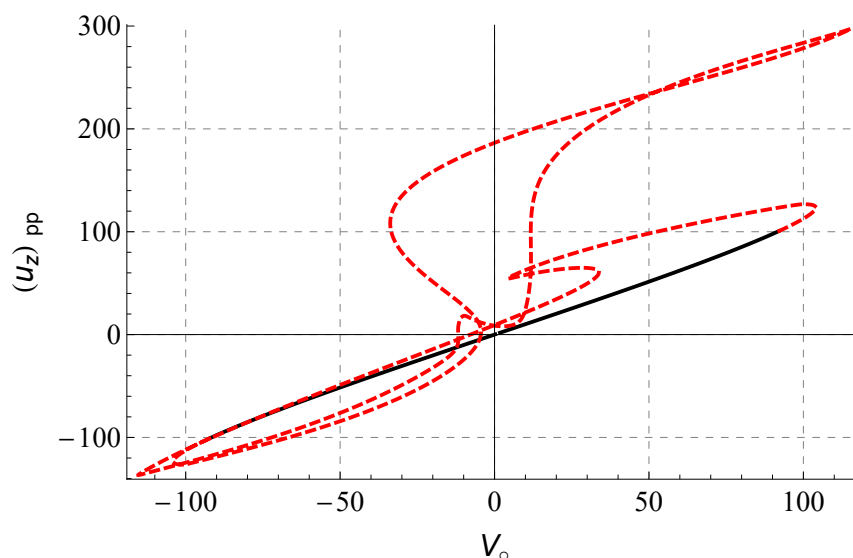


Figure 6.8: The peak-to-peak displacement $u_{z(pp)}$ as a function of electrode voltage V_o for the PZT4 sensor with air as a medium-under-test. Stable equilibria are shown as solid black lines, and unstable equilibria are shown as dashed red lines.

multiple secondary branches of unstable equilibria appear in the sensor response, Figure 6.8, with asymmetry becoming more pronounced for the branches corresponding to larger displacement.

The eigenvalues of the equilibria along the primary branch are shown in Figure 6.9 for the voltage range $[0, 92]$ V. They reveal that in the presence of an air sample, the sensor loses stability when the pair of eigenvalue corresponding to the third mode exits the complex plane via $-\infty$ and re-enters via $+\infty$. However, the complex pair corresponding to the fourth mode does not cross the imaginary axis. The eigenvalues of the equilibria along all branches are shown in Figure 6.10. They indicate that voltage breakdown underlies the loss of stability along the secondary branches of solutions. Additionally, the fourth eigenvalue (red line) in Figure 6.9 appears to interact with the fifth mode in the voltage range from 50 V to 90 V.

We conclude that the limit on the sensor voltage varies with the sample permittivity from a

maximum of 92 V DC in air to lower values in the range of 81 V for aqueous (water-like) media. It is possible to retard voltage breakdown by choosing a softer substrate with a lower modulus of rigidity G , thereby increasing the electromechanical coupling coefficient.

We also note that the static response of the sensor, even at high voltages, is rather small on the order of a few nanometers. Therefore, it is advantageous to operate the sensor dynamically, in order to exploit the high-quality factors of shear acoustic waves to generate larger displacement and electric fields (signal-to-noise-ratio). In this case, the measurand used to estimate the sample properties is the sensor resonant frequency.

Comparing Figures 6.7 and 6.9 it is clear that the sensor's eigenvalues (natural frequencies) are sensitive to the medium-under-test. It can be seen from equation (4.15) that, aside from the substrate properties, the natural frequencies of the sensor are a function only of the sample permittivity.

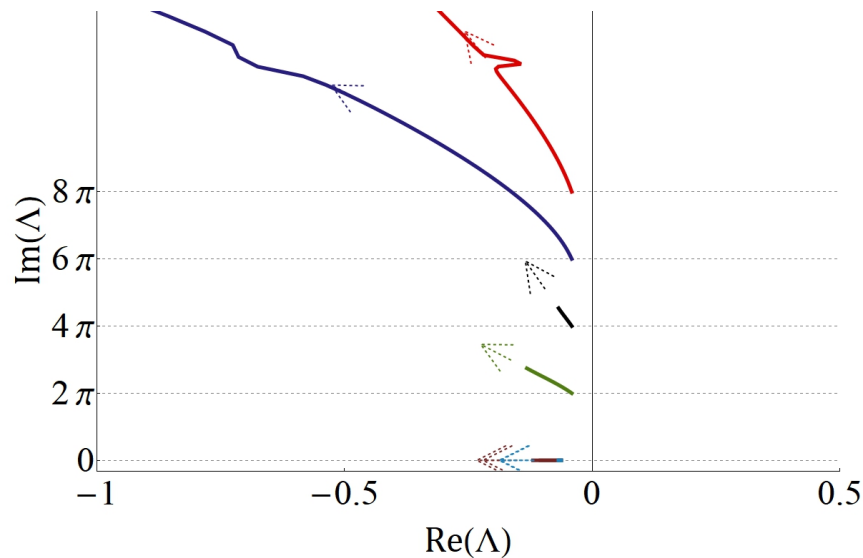


Figure 6.9: The eigenvalues of the equilibria along the primary branch of the PZT4 sensor for an air sample and the voltage range $[0, 92]$ V. Arrows indicate the direction of increasing voltage.

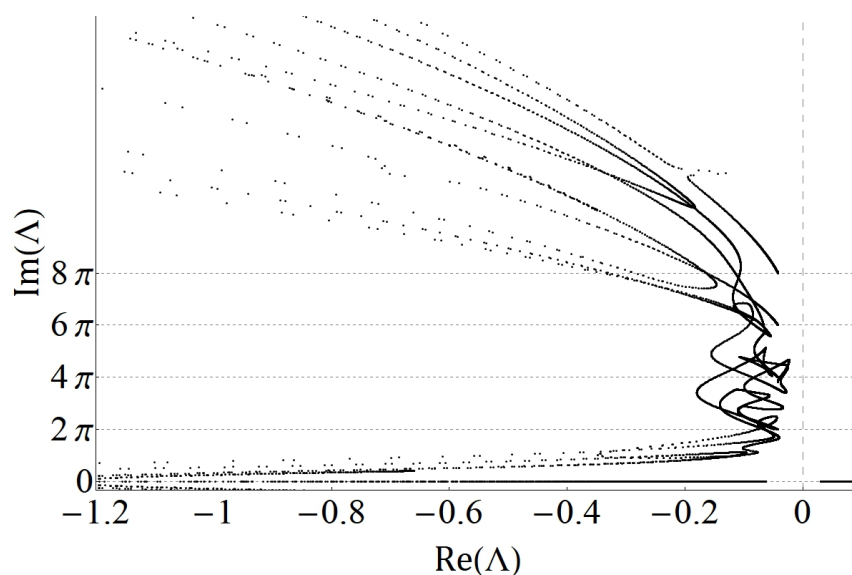


Figure 6.10: Eigenvalues of all equilibria of a PZT4 sensor for an air sample.

6.5 Experimental Verification

The sensor tested was designed as an IDT with $m = 100$ electrodes and a wavelength of $\lambda = 40 \mu m$, shown in Figure 6.11 prior to laser trimming. Two substrates with four identical sensors on each of them were fabricated. The final experimental results shown below were obtained from one of those sensors and found to be in agreement with those of a second sensor.

Using direct probing, a voltage bias was applied across the electrodes and the displacement at the fingertip was measured optically using a laser Doppler vibrometer [1], as outlined in section 5.3. Figure 6.12 compares the experimentally measured peak-to-peak static displacement (gray dots) in air to those predicted using the linear model (blue line), equation (6.18), and nonlinear model (black line for stable equilibria and red dashed line for unstable equilibria), equations (6.21) and (6.22), and shown previously in Figure 6.8. It is important to note that the experimental results diverge from the linear model prediction to match those of the nonlinear model within

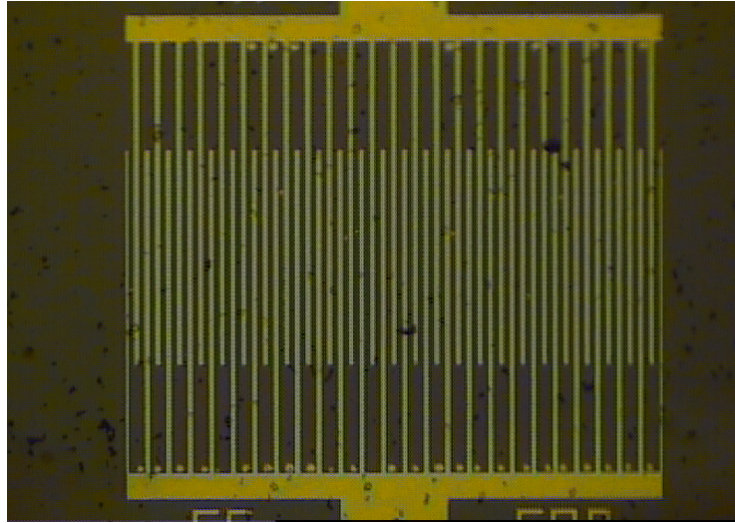


Figure 6.11: A prototype of the fabricated PZT4 sensor, prior to laser patterning.

measurement error, thereby validating the latter model.

The electrostrictive constant was experimentally identified by matching the measured displacement to the nonlinear model predictions as $M = 12.7 \times 10^{-18} \text{ m}^2/\text{V}^2$, which lies in the range of values reported in the literature [122]. As the DC voltage was increased, electrical breakdown damage was observed on the electrodes at $V_o = 96 \text{ V}$. This is in good agreement with the model predicted voltage breakdown of $V_o = 92 \text{ V}$. Figure 6.13 shows the sensor before 6.13a and after 6.13b breakdown.

6.6 Summary

In this chapter, the response of the BG wave to forced non-resonant and static excitation was investigated. The effect of different kinds of damping in the system and the method of wave excitation were also studied. Both the linear and the nonlinear forced damped sensors were

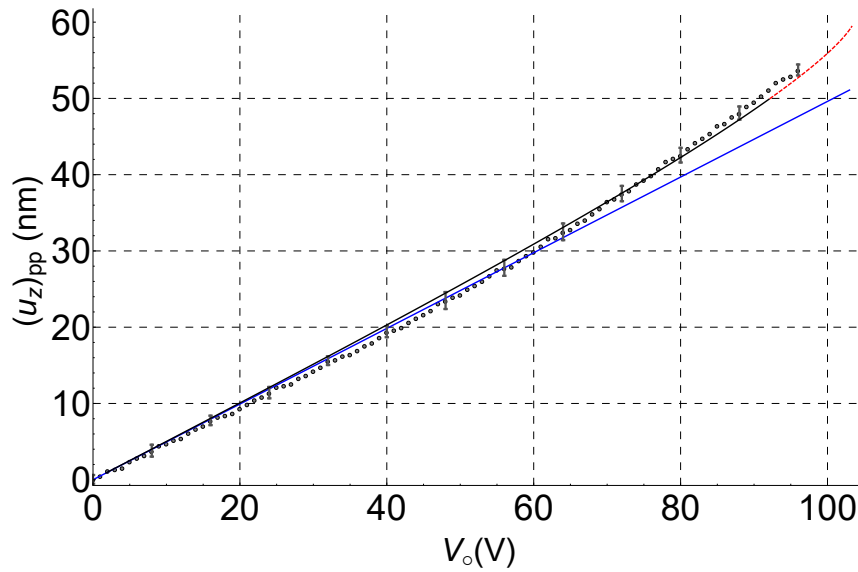


Figure 6.12: Comparison of experimentally measured peak-to-peak displacement of the PZT4 sensor in air (gray line) as a function of DC voltage V_0 to those predicted by linear (blue line) and nonlinear models (black and red dashed lines). The error bars show the standard deviation.

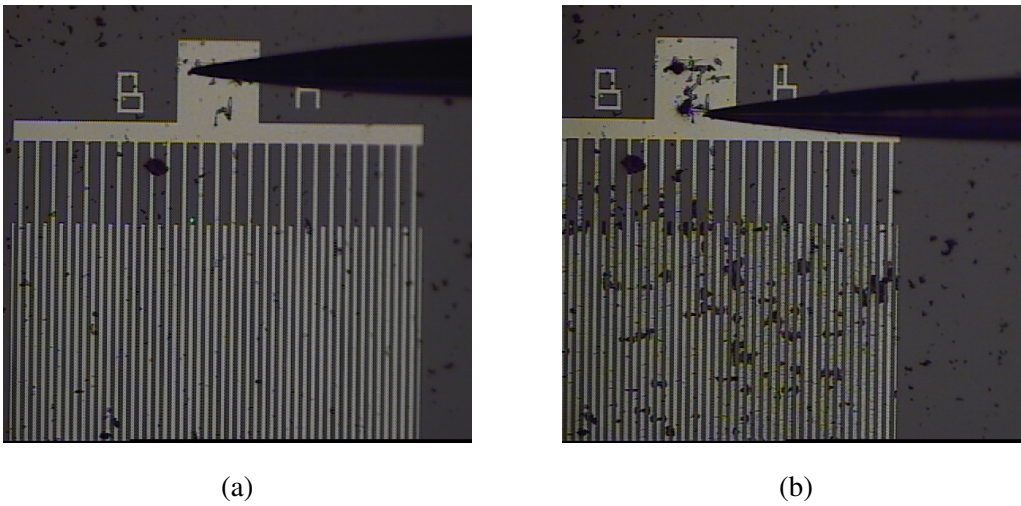


Figure 6.13: The sensor before (a) and after (b) breakdown.

solved for the static response. The numerical model was validated experimentally, and the results were published.

Additionally, the eigenvalue analysis predicted an electrical instability that was validated experimentally when electrical breakdown was observed.

Chapter 7

Resonant Excitation³

In this chapter, linear and nonlinear resonant excitations of the BG wave resonator are investigated. The response is analyzed numerically and then validated experimentally. Lastly, the impact of different media-under-test on the BG resonator response is experimentally investigated, and the sensor operation is demonstrated.

7.1 Linear BG Resonator

It is useful to initially investigate the linear response in order to understand the basic operation of the sensor. The linear resonator equations of motion can be obtained by dropping the nonlinear

³This chapter is adapted from **Elhady, Alaa**, M. Basha, and E. M. Abdel-Rahman, “Measurement of electric permittivity using Bleustein-Gulyaev wave sensors,” *Journal of Micromechanics and Microengineering*, 2021. In progress

terms from equations (6.8) and (6.9), which yields:

$$G \nabla^2 u_z + e \nabla^2 \psi = \rho \ddot{u}_z + c \dot{u}_z \quad (7.1)$$

$$e \nabla^2 u_z - \epsilon \nabla^2 \psi = \zeta + \sigma \int \nabla^2 \psi dt \quad (7.2)$$

These equations can be rewritten, after lumping the dielectric and mechanical loss terms into the viscous damping term, multiplying the second equation by e/ϵ , and adding them, as:

$$\rho \ddot{u}_z + c \dot{u}_z - \left(G + \frac{e^2}{\epsilon}\right) \nabla^2 u_z = -\frac{e}{\epsilon} \zeta \quad (7.3)$$

The equation represents a simple forced damped harmonic oscillator.

Similar to the static case, section 6.1.1, the IDT will be used to excite the n th mode of the BG resonator by applying the time-varying voltage distribution

$$V(x, y, t) = V_0 e^{-\kappa_n y} \cos(k_n x) \cos(\Omega t) \quad (7.4)$$

across its fingers, where Ω is the excitation frequency. Recalling that:

$$\mathbf{D} = \epsilon_T \nabla V$$

and using equation (6.5), the charge distribution can be written as:

$$\begin{aligned} \zeta(x, y, t) &= \epsilon_T \nabla^2 V(x, y, t) \\ &= \epsilon_T \beta_n^2 V(x, y, t) \end{aligned} \quad (7.5)$$

where $\beta_n = k_n^2 - \kappa_n^2$ and n is the mode number. The displacement field can be assumed to take the harmonic form given by equation (4.19):

$$u_z(x, y, t) = e^{-\kappa_n y} \cos(k_n x) u(t)$$

Substituting with the charge distribution and displacement fields into equation (7.3) yields:

$$\rho \ddot{u} + c \dot{u} + \left(G + \frac{e^2}{\epsilon}\right) \beta_n^2 u = \frac{e \epsilon_T}{\epsilon} \beta_n^2 V_0 \cos(\Omega t) \quad (7.6)$$

This equation can be rewritten as:

$$\ddot{u} + \frac{\omega_n}{Q}\dot{u} + \omega_n^2 u = \frac{f_o}{\rho} \cos(\Omega t) \quad (7.7)$$

where $\omega_n = \beta_n \sqrt{\frac{G+e^2/\epsilon}{\rho}}$ is the natural frequency, $Q = \frac{\rho\omega_n}{c}$ is the quality factor, and

$$\begin{aligned} f_o &= \frac{e\epsilon_T}{\epsilon} \beta_n^2 V_o \\ &= \frac{e\omega_n^2}{G} V_o \end{aligned} \quad (7.8)$$

is the forcing amplitude imposed by the charge density.

For an under-damped system ($Q > \frac{1}{2}$), the solution of this equation is given by [125]:

$$\begin{aligned} u(t) &= \frac{f_o}{\sqrt{(\omega_n^2 - \Omega^2)^2 + (\frac{\omega_n \Omega}{Q})^2}} \cos(\Omega t) \\ &= \frac{\frac{e}{G} V_o}{\sqrt{(1 - \frac{\Omega^2}{\omega_n^2})^2 + (\frac{\Omega}{\omega_n Q})^2}} \cos(\Omega t) \end{aligned} \quad (7.9)$$

Therefore, the displacement field is given by:

$$u_z(x, y, t) = \frac{\frac{e}{G} V_o}{\sqrt{(1 - \frac{\Omega^2}{\omega_n^2})^2 + (\frac{\Omega}{\omega_n Q})^2}} e^{-\kappa_n y} \cos(k_n x) \cos(\Omega t)$$

7.2 Nonlinear BG Resonator

7.2.1 Problem Statement

To better capture the detailed dynamic response and exploit it to enhance the sensor sensitivity, we retain the electrostrictive nonlinearity in the equations of motion and account explicitly for the damping present in the dielectric loss term. The quasi-static approximation of

the nonlinear forced and damped system of equations (6.8) and (6.9) is an index-1 system of Differential-Algebraic Equations (DAE). In fact, this is a nontraditional DAE form due to the integral term on the right-hand side. We reduce the system to an index-0 differential system by differentiating equation (6.9) once with respect to time, thereby disbanding with the integral term to obtain:

$$\rho \ddot{u}_z + c \dot{u}_z - G \nabla^2 u_z - e \nabla^2 \psi - MGL_1(\psi) = 0 \quad (7.10)$$

$$\dot{\zeta} + \sigma \nabla^2 \psi - e \nabla^2 \dot{u}_z + \epsilon \nabla^2 \dot{\psi} - M\dot{L}_2(u_z, \psi) = 0 \quad (7.11)$$

This system is nondimensionalized following the scheme described in section 3.4 and using the nondimensional variables:

$$\begin{aligned} \hat{x} &= \frac{x}{l}, & \hat{y} &= \frac{y}{l}, & \hat{t} &= \frac{c_s t}{\lambda} \\ \hat{u}_z &= \frac{u_z}{u_o}, & \hat{\psi} &= \frac{\psi}{\psi_o}, & \hat{\zeta} &= \zeta \frac{l^2}{\epsilon_T \psi_o} \end{aligned}$$

where $u_o = \frac{e}{G} \psi_o$ and $\psi_o = 1$ V. Therefore equations (7.10) and (7.11) can be written as:

$$\Lambda_A \triangleq \alpha \ddot{\hat{u}}_z + \hat{c} \dot{\hat{u}}_z - \nabla^2 \hat{u}_z - \nabla^2 \hat{\psi} - \hat{M} \hat{L}_1(\hat{\psi}) = 0 \quad (7.12)$$

$$\hat{\Lambda}_B \triangleq \left(1 + \frac{G\epsilon}{e^2}\right) \dot{\hat{\zeta}} + \frac{G\epsilon}{e^2} \chi \nabla^2 \hat{\psi} - \nabla^2 \dot{\hat{u}}_z + \frac{G\epsilon}{e^2} \nabla^2 \dot{\hat{\psi}} - \hat{M} \hat{L}_2(\hat{u}_z, \hat{\psi}) = 0 \quad (7.13)$$

where:

$$\alpha = \frac{l^2}{\lambda^2} \left(1 + \frac{e^2}{G\epsilon}\right), \quad \hat{c} = c \sqrt{\frac{\alpha}{\rho G}} l, \quad \hat{M} = \frac{MG}{el}, \quad \chi = \frac{\lambda}{c_s} \sigma$$

\hat{L}_1 and \hat{L}_2 are nondimensional versions of the differential operators, and Λ_A and Λ_B are operators that encase the left-hand sides of the nondimensional system of equations.

7.2.2 Discretization

The system is discretized using the Galerkin residuals method [120]. Under the proportional damping assumption, modes that are not directly, or indirectly, excited will undergo damping and

vanish in the steady-state response. This leaves directly and indirectly excited modes to carry the energy in the system. Therefore, the Galerkin residuals method is valid, provided enough modes are taken in the expansion. Towards that end, the displacement and electric fields are rewritten in terms of static and dynamic components, such that:

$$u_z(x, y, t) = u_z^s(x, y) + u_z^d(x, y, t) \quad (7.14)$$

$$\psi(x, y, t) = \psi^s(x, y) + \psi^d(x, y, t) \quad (7.15)$$

where the superscripts s and d denote the static and dynamic components, respectively. Based on the convergence analysis carried out in section 6.4.2, the number of modes was set to $N = 4$. Thus, for a four-mode expansion, the static equilibrium can be evaluated as

$$u_z^s(x, y) = \sum_{n=1}^4 q_{sn} \phi_n(x, y) \quad (7.16)$$

$$\psi^s(x, y) = \sum_{n=1}^4 p_{sn} \phi_n(x, y) \quad (7.17)$$

where the modal coordinates q_{sn} and p_{sn} are obtained by solving the algebraic system of equations (C.7) to (C.14). Likewise, the dynamic components are discretized in terms of the unforced linear mode shapes, equation (4.19), as:

$$u_z^d(x, y, t) = \sum_{n=1}^4 q_n(t) \phi_n(x, y) \quad (7.18)$$

$$\psi^d(x, y, t) = \sum_{n=1}^4 p_n(t) \phi_n(x, y) \quad (7.19)$$

where $q(t)$ and $p(t)$ are modal coordinates.

Excitation

The forcing term in this system is the charge distribution ζ imposed by the IDT, equation (7.5). As shown in Chapter 6, it can be approximated by a Fourier series expansion as:

$$V(x, y, t) = \sum_{n=1}^4 C_{2n-1} e^{-\kappa(2n-1)y} \cos\left((2n-1)m \frac{\pi x}{l}\right) (V_{DC} + V_{AC} \cos(\Omega t)) \quad (7.20)$$

where C_{2n-1} are the empirically fitted constants listed in Table 6.1 and V_{DC} and V_{AC} are the bias and amplitude of the voltage waveform.

Dynamic Conductive Losses

The conductivity of the dielectric substrate σ is strongly dependent on the excitation frequency. Jonscher's power law relates conductivity to the frequency of the electric field by [126]:

$$\sigma = \sigma_{DC} + \sigma_{AC}$$

where σ_{DC} is a frequency invariant component, σ_{AC} is proportional to the s power of the excitation frequency $\sigma_{AC} \propto \Omega^s$, and s is a constant such that $0 \leq s \leq 1$. At room temperature, $s \approx 1$. It decreases as the temperature increases [126]. As a result, AC conductivity is much larger than its DC counterpart for frequencies in the MHz range. Therefore, in this work, DC conductivity is neglected and total conductivity is approximated as:

$$\sigma \approx \epsilon \Omega \tan \delta \quad (7.21)$$

where $\tan \delta$ is an electrical dissipation factor called the loss tangent of the piezoelectric substrate. The loss tangent for PZT4 is $\tan \delta = 0.02$ [124] and that for LiNbO₃ is $\tan \delta = 0.004$ [127].

7.2.3 Numerical Solution

The system of equations (7.12) and (7.13) is discretized by substituting for the displacement and electric potential fields with equations (7.14) to (7.19), substituting for the forcing and damping terms with equations (7.20) and (7.21), respectively, multiplying by the left eigenfunction, and setting the integral over the domain equal to zero. The residuals can thus be written as:

$$R_{1n} = \int_0^\infty \int_0^l \phi_n(x, y) \Lambda_A(q_n, p_n) dx dy \quad (7.22)$$

$$R_{2n} = \partial_t \int_0^\infty \int_0^l \phi_n(x, y) \Lambda_B(q_n, p_n) dx dy \quad (7.23)$$

where ∂_t denotes the time derivative and $n = 1$ to N , where $N = 4$. The order of integration and differentiation was reversed in equation (7.23) in order to reduce the complexity of carrying out the integration. The integration process was carried out symbolically in Mathematica [121]. Setting the residuals R_{1n} and R_{2n} to vanish, yields the discretized system of ordinary differential equations, (C.15) to (C.22).

7.3 Simulation Results

The resulting system of ordinary differential equations was numerically solved in Mathematica. First, the equilibrium equations, (C.7) to (C.14), are solved for the static modal coordinates q_{sj} and p_{sj} . Next, they are substituted into the dynamic system, equations (C.15) to (C.22), which is, then, integrated over time to obtain the dynamic modal coordinates $q_j(t)$ and $p_j(t)$. Finally, the system response is obtained by substituting the modal coordinates into equations (7.14), and

(7.15), as:

$$u_z(x, y, t) = u_z^s(x, y) + u_z^d(x, y, t) = \sum_{j=1}^N (q_{sj} + q_j(t)) \phi_j(x, y) \quad (7.24)$$

$$\psi(x, y, t) = \psi^s(x, y) + \psi^d(x, y, t) = \sum_{j=1}^N (p_{sj} + p_j(t)) \phi_j(x, y) \quad (7.25)$$

where $N = 4$. Figure 7.1 compares the time evolution of the potential field at the left edge of the PZT4 resonator surface $\psi(0, 0, t)$ to that of the LiNbO₃ resonator. The resonators were excited at their respective natural frequencies, $\Omega = 64.8$ and 21.4 MHz, respectively, with the voltage waveform an $V_{AC} = 0.5$ V and $V_{DC} = 0$ V. In both cases, the mechanical quality factor was set to $Q = 10$, whereas the dielectric loss was set as per equation (7.21).

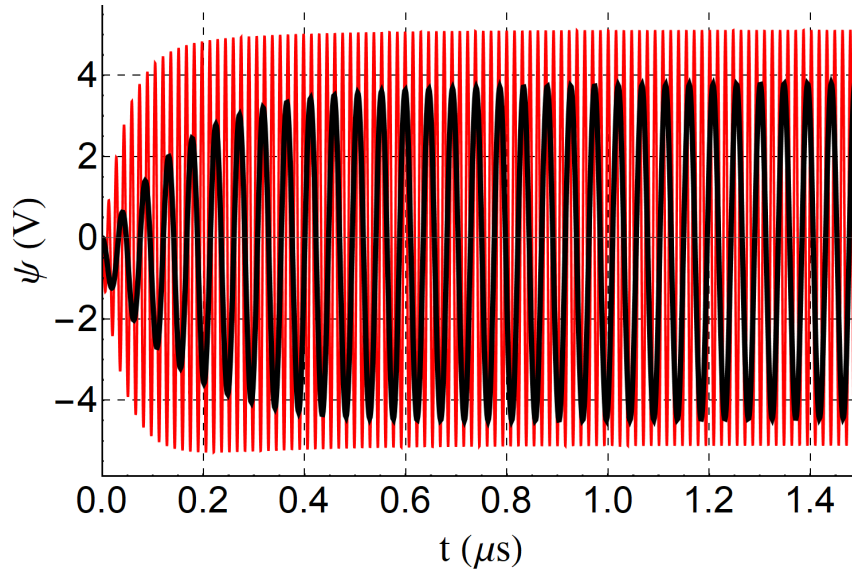


Figure 7.1: The time evolution of the potential field $\psi(0, 0, t)$ for the PZT4 (red line) and LiNbO₃ (black line) resonators under a pure AC excitation of 1 V_{pp} at the excitation frequencies $\Omega = 64.8$ MHz and 21.4 MHz, respectively.

Since PZT4 is more conductive than LiNbO₃, it exhibits larger electrical losses and a lower

total quality factor than LiNbO_3 . As a result, its response, red line in Figure 7.1, has a shorter settling time than that of LiNbO_3 (black line). On the other hand, even though the LiNbO_3 resonator has a higher effective quality factor, its steady-state potential is lower than that of PZT4 due to a lower electromechanical coupling coefficient $\sqrt{e^2/(G\epsilon + e^2)}$ [99]. PZT4 is more efficient in coupling the excitation voltage to the potential field with a coupling coefficient of 70.6%, compared to 64.8% for LiNbO_3 . The same trends are also evident in comparing the displacement fields, Figure 7.2, of the PZT4 and LiNbO_3 resonators at $u_z(0, 0, t)$.

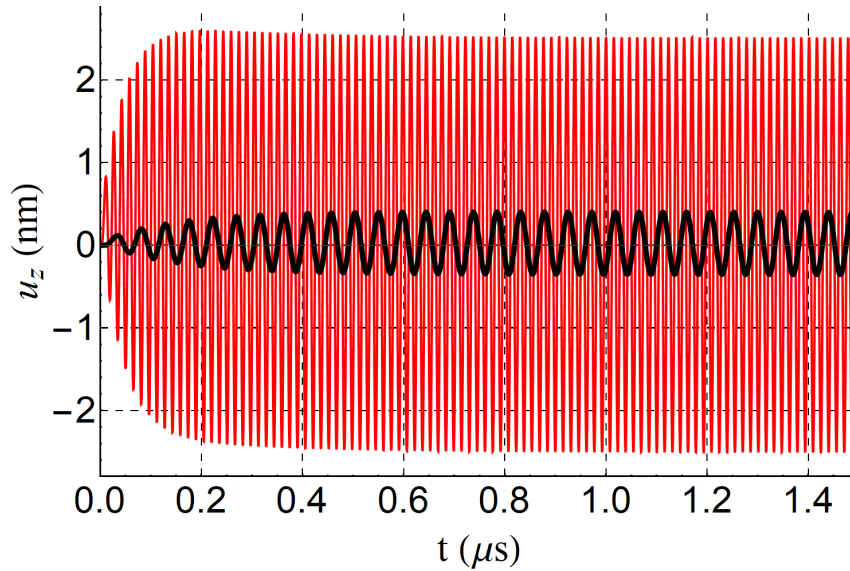


Figure 7.2: The time evolution of the shear displacement field $u_z(0, 0, t)$ for the PZT4 (red line) and LiNbO_3 (black line) resonators under a pure AC excitation of 1 V_{pp} at the frequencies $\Omega = 64.8 \text{ MHz}$ and 21.4 MHz , respectively.

Three different media were tested, namely, air, ethanol, and deionized (DI) water. Although BG waves have been previously used to sense viscosity, they were deployed in a line-delay configuration rather than a resonator. When used in a resonant configuration, the medium-under-test viscosity would not affect the natural frequency [10]. However, as a precaution, this was

taken into consideration. At room temperature, ethanol and DI water have similar viscosities but different relative permittivities at 24 and 78, respectively [128, 129]. Therefore they present good candidates for the characterization of a permittivity sensor.

The frequency-response curves of the displacement and potential fields are shown in Figures 7.3 and 7.4, respectively, for the PZT4 sensor with air (black), ethanol (red), and DI water (blue) media-under-test. The curves show the peak-to-peak displacement $u_{z(pp)}$ and potential $\psi_{(pp)}$ at the origin, point $(0, 0)$. The frequency sweep was carried out numerically by solving equations (C.15) to (C.22) subject to a voltage waveform with a constant amplitude $V_{AC} = 0.5$ V and with the frequency varying in the range $\Omega = [13, 265]$ MHz. The steady-state response was obtained by carrying long-time integration for 300 excitation periods and recording the peak-to-peak response during the last 10 periods of the time history. The excitation frequency was increased in steps varying in size from 20 kHz, close to resonance, to 500 kHz away from resonances. After each frequency step, the initial conditions were taken as the modal coordinates of the last point in the time-history of the previous excitation frequency.

The response curves show evidence of primary resonance in the vicinity of the first and third modes. This reflects the fact the IDT geometry, described in equation (7.20), represents direct excitation for both modes. The effective quality factors of the first ($f_1 = 64.8$) and third ($f_3 = 194.4$) modes were calculated from the response curves using the half-power bandwidth method and found to be $Q_1 = 8.5$ and $Q_3 = 27$. It is interesting to note that the potential response curves exhibit evidence of anti-resonance, Figure 7.4, but not those of the displacement field, Figure 7.3, indicating lower electric losses.

Both resonant peaks, Figures 7.3 and 7.4, shift to lower frequencies as the permittivity of the medium-under-test increases. The sensitivity of the third mode towards changes in permittivity is more than that of the lower mode as evidenced by a larger frequency shift. Specifically, the resonant frequency of the first mode shifts down by $\Delta f_1 = 0.65$ MHz in the presence of ethanol and

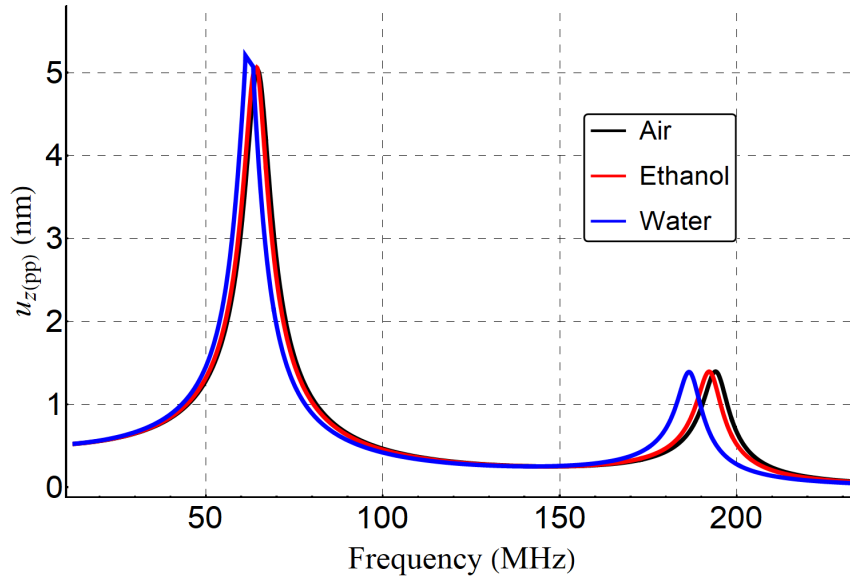


Figure 7.3: The frequency-response curves of the shear displacement field u_z at the origin $(0, 0)$ of the PZT4 sensor under a voltage waveform with an amplitude of $V_{AC} = 0.5$ V for three media-under-test.

by $\Delta f_1 = 2.5$ MHz in the presence of water compared to $\Delta f_3 = 1.84$ MHz and $\Delta f_3 = 7.5$ MHz for the third mode. The drop in the resonant frequency with increased medium-under-test permittivity is expected as per equation (4.15). Higher permittivity leads to stronger coupling between BG waves and the medium-under-test represented by a larger capacitance of that medium. The elevated sensitivity of the third mode compared to the first mode is also expected since the sensitivity, equation (4.16), is linearly proportional to mode number n .

The amplitude of the higher mode is less than that of the lower mode because the direct excitation of the IDT to the higher mode is smaller than that to the lower mode, see Table 6.1. Further, higher modes are stiffer, therefore requiring larger forcing to realize similar amplitudes. This presents a trade-off between modal sensitivity and their signal-to-noise ratio (SNR).

The frequency-response curves of the LiNbO_3 sensor were obtained numerically using the

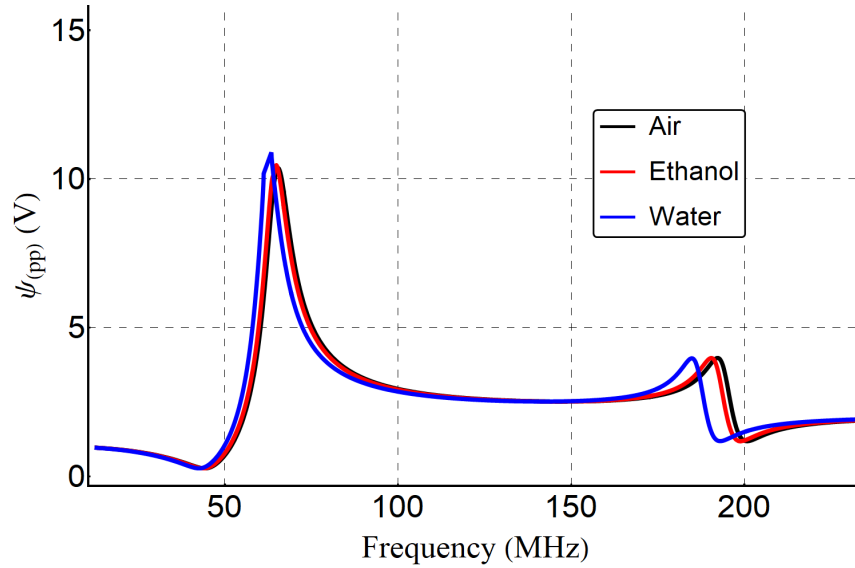


Figure 7.4: The frequency-response curves of the potential field ψ at the origin $(0, 0)$ of the PZT4 sensor under a voltage waveform with an amplitude of $V_{AC} = 0.5$ V for three media-under-test.

same procedure and voltage waveforms except that the frequency of excitation was swept in the range $\Omega = [4, 88]$ MHz to capture the primary resonance of the first ($f_1 = 21$ MHz) and third ($f_3 = 63$ MHz) modes. The frequency steps varied in size from 6.8 kHz, close to resonance, to 170 kHz away from the resonances. The frequency-response curves of the peak-to-peak displacement $u_{z(pp)}$ and potential $\psi_{(pp)}$ at the origin $(0, 0)$ are shown in Figures 7.5 and 7.6, respectively, for air (black), ethanol (red), and DI water (blue) media-under-test. The sensor was designed using a larger wavelength λ specifically in order to reduce its natural frequencies, thereby simplifying the experimental setup.

Similar to the PZT4 sensor, both resonant peaks shift to lower frequencies as the permittivity of the medium-under-test increases. Further, the third mode was also found to be more sensitive than the first mode. Specifically, the resonant frequency of the first mode shifts down by $\Delta f_1 = 1.38$ MHz in the presence of ethanol and by $\Delta f_1 = 1.72$ MHz in the presence of water compared

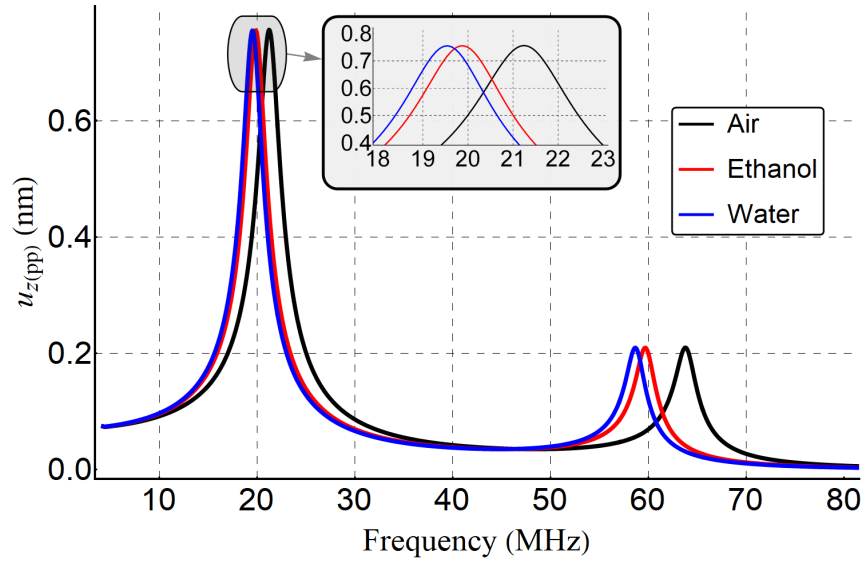


Figure 7.5: The frequency-response curves of the shear displacement field u_z at the origin $(0, 0)$ of the LiNbO_3 sensor under a voltage waveform with an amplitude of $V_{AC} = 0.5$ V for three media-under-test.

to $\Delta f_3 = 4.11$ MHz and $\Delta f_3 = 5.12$ MHz for the third mode.

The ratio of the frequency shift to the first natural frequency in LiNbO_3 sensor is 6.5% for ethanol and 8% for DI water, while for the PZT4 sensor, it is 1% for ethanol and 3.8% for DI water. Therefore, the LiNbO_3 sensor is more sensitive to changes in permittivity than the PZT4 sensor. This is in agreement with the findings of section 4.2, namely that sensitivity improves as the permittivity of the medium-under-test approaches half the permittivity of the sensor substrate, Figure 4.2. However, this comes at the expense of a smaller SNR, weaker potential and displacement fields, for the LiNbO_3 sensor, and thus presents a trade-off between sensitivity and SNR.

To investigate the impact of the electrostrictive nonlinearity, the frequency response of the sensor was evaluated under biased and unbiased voltage waveforms. Figures 7.7 and 7.8 show the

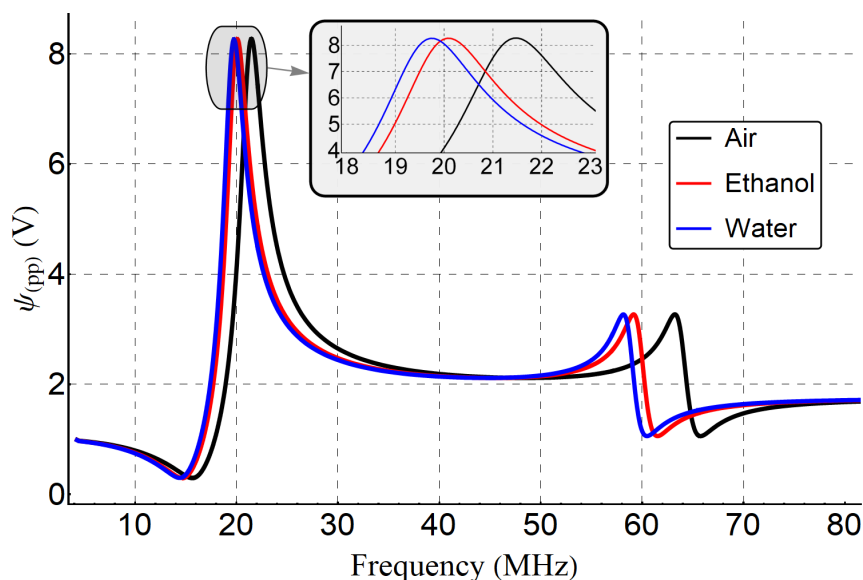


Figure 7.6: The frequency-response curves of the potential field ψ at the origin $(0, 0)$ of the LiNbO_3 sensor under a voltage waveform with an amplitude of $V_{AC} = 0.5$ V for three media-under-test.

frequency-response curves of the PZT4 sensor's peak-to-peak displacement $u_{z(pp)}$ and potential $\psi_{(pp)}$ at the origin $(0, 0)$, respectively, in the vicinity of the second mode natural frequency ω_2 . Both waveforms had the same AC amplitude $V_{AC} = 0.5$ V, one was unbiased with $V_{DC} = 0$ V, shown in solid lines, and the other was biased with $V_{DC} = 40$ V, shown in dashed lines.

The impact of the quadratic electrostrictive nonlinearity can be clearly seen in activation of the second mode. While the biased voltage waveform excites primary resonance of that mode, the unbiased voltage waveform fails to excite it. The resonant peak of the second mode does not only shift to lower frequencies, like the first and third modes, but also increases in magnitude as the permittivity of the medium-under-test increases. However, the use of DC voltage with electrolytic test media, such as water, presents a challenge since it will result in electrolysis. This issue will be further investigated in future work.

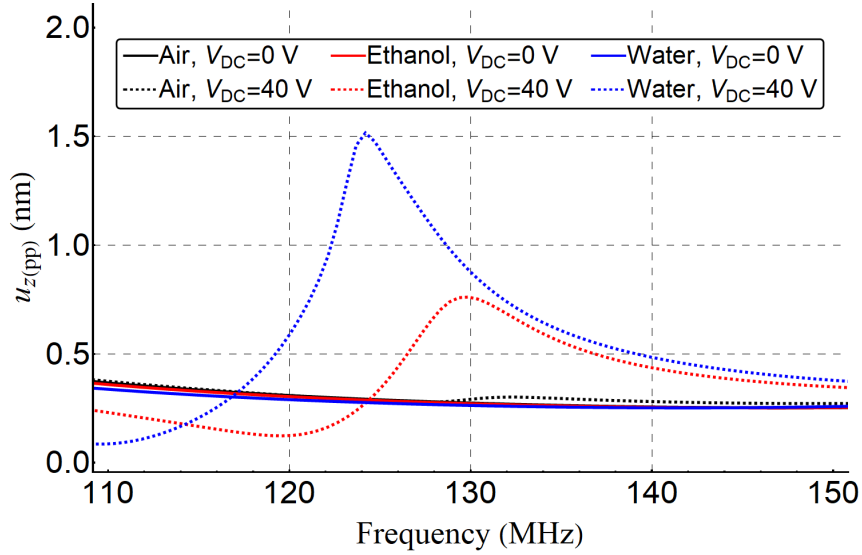


Figure 7.7: The frequency-response curves of the shear displacement field u_z at the origin $(0, 0)$ of the PZT4 sensor in the vicinity of the second mode natural frequency ω_2 for three media-under-test. The sensor is excited with an unbiased voltage waveform (solid lines) and a waveform biased with $V_{DC} = 40$ V (dashed lines). The AC amplitude for both waveforms is $V_{AC} = 0.5$ V.

7.4 Experimental Validation

The designed IDT were limited by trenches on either side, as per the schematic shown in Figure 2.1b, to reflect generated BG waves, thus creating resonant standing waves. To test the operation of the permittivity sensor, two prototypes were fabricated using LiNbO_3 and PZT4 substrates. They were designed to have first natural frequencies of $f_1 = 21.4$ MHz, and $f_1 = 64.8$ MHz, respectively. The specification of the prototypes are summarized in Table 7.1. The linear material constants, as specified by the manufactures and confirmed by comparison to the literature, are listed in Table A.1. The electrostrictive constant of PZT4 was identified by matching the model predictions to the experimentally measured out-of-plane displacement, Figure 6.12, and found to be $M = 12.7 \times 10^{-18} \text{ m}^2/\text{V}^2$ [2]. Following a similar procedure, the electrostrictive constant of

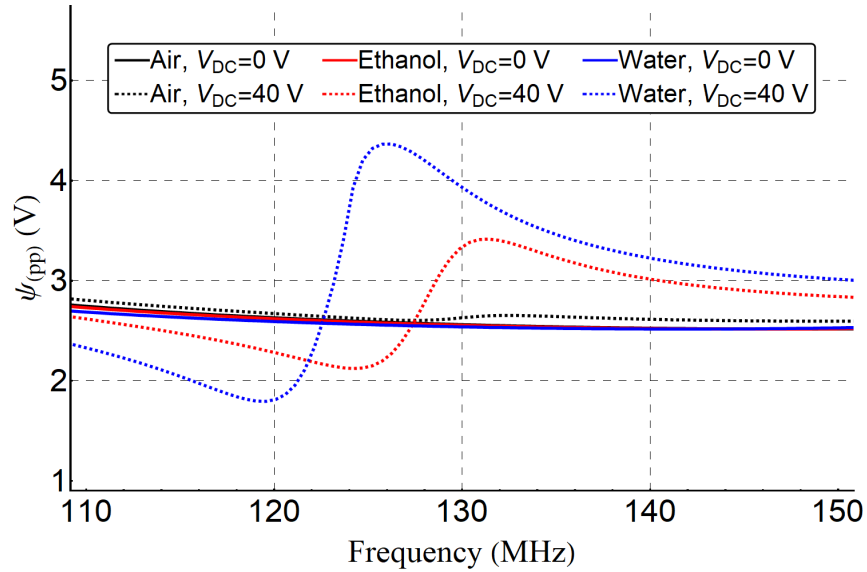


Figure 7.8: The frequency-response curves of the potential field ψ at the origin $(0, 0)$ of the PZT4 sensor in the vicinity of the second mode natural frequency ω_2 for three media-under-test. The sensor is excited with an unbiased voltage waveform (solid lines) and a waveform biased with $V_{DC} = 40$ V (dashed lines). The AC amplitude for both waveforms is $V_{AC} = 0.5$ V.

LiNbO_3 was experimentally identified to be $1.3 \times 10^{-20} \text{ m}^2/\text{V}^2$.

Table 7.1: Specification of the fabricated prototypes.

Substrate Material	λ [μm]	Aperture [μm]	Resonance Freq. [MHz]	Purchased From
PZT4	40	400	64.8	APC International [97]
LiNbO_3	220	2000	21.4	Boston Piezo Optics [100]

7.4.1 Experimental Setup

As discussed earlier, ethanol and DI water are suitable for validating the operation of the permittivity sensors. Therefore, the characterization of the sensor was performed using the two aforementioned media-under-test, in addition to the case where no medium, except air, was present. The sensor was characterized electrically using the Agilent E5061B Vector Network Analyzer, VNA, as discussed in Section 5.4. Calibration of the VNA was performed using the short-open-load approach.

The parasitic capacitance was identified by fitting the experimental and theoretical S_{11} responses, and the values of f_o and Q were experimentally measured and then used to identify the RLC parameters [116]. This was previously explained in detail, in Section 5.4.2. Figure 7.9 shows the modeled S_{11} of the LiNbO₃ resonator as a function of the frequency. The empirically fit parasitic capacitance, in that case, was found to be $c_{p0} = 794$ pF.

7.4.2 Permittivity Sensor Validation

The results of using the VNA to characterize the PZT4 based sensor are shown in Figure 7.10. This PZT4 sensor did not show promising results, as the minimum S_{11} recorded did not drop below -10 dBm. Indeed, Figure 7.10 shows a return loss of only 5.5 dB. Additionally, the recorded resonance frequency was 44.7 MHz, which was much lower than the designed value of 64.8 MHz. This deviation can be attributed to parasitics as well as uncertainty in the fabricated IDT dimensions, and it was found to exist for other tested PZT4 based sensors.

The S_{11} vs. frequency measurements using the PZT4 sensor, with the medium-under-test set as air (black), ethanol (red), and water (blue) are shown Figure 7.11. However, due to the aforementioned challenges, it was concluded that further testing and analysis of the PZT4 is suspended due to fabrication issues.

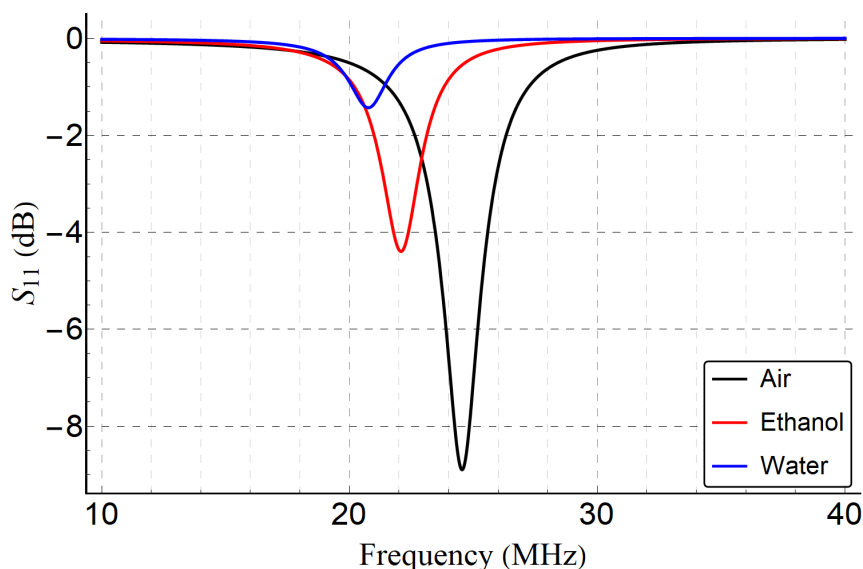


Figure 7.9: Modeled S-parameters based on the RLC equivalent circuit for the LiNbO_3 sensor. The model includes parasitic capacitors for the different media-under-test.

On the other hand, the LiNbO_3 based sensor showed promising results, Figure 7.12. The Figure shows the S_{11} vs. frequency with the medium-under-test set as air (black), ethanol (red), and water (blue). The ethanol and DI water were deposited using a pipette, Figure 7.13, on the entire surface of the sensor and the IDT. The insertion loss observed for all the tests was well above 15 dB.

The measurements in Figure 7.12 were repeated several times, and the statistical mean and standard deviation were recorded in Table 7.2. Additionally, measurements of ethanol, diluted to 50 % using DI water, were performed, and the results are included in the table.

The frequency response of using either air or ethanol as the medium-under-test, Figure 7.12 is in good agreement with the modeled S-parameters, Figure 7.9, in terms of the position of the S_{11} minima on the frequency axis. However, the values of the S_{11} minima on the y-axis do not match. Such values depend on two factors, the electrical matching and the damping effect of

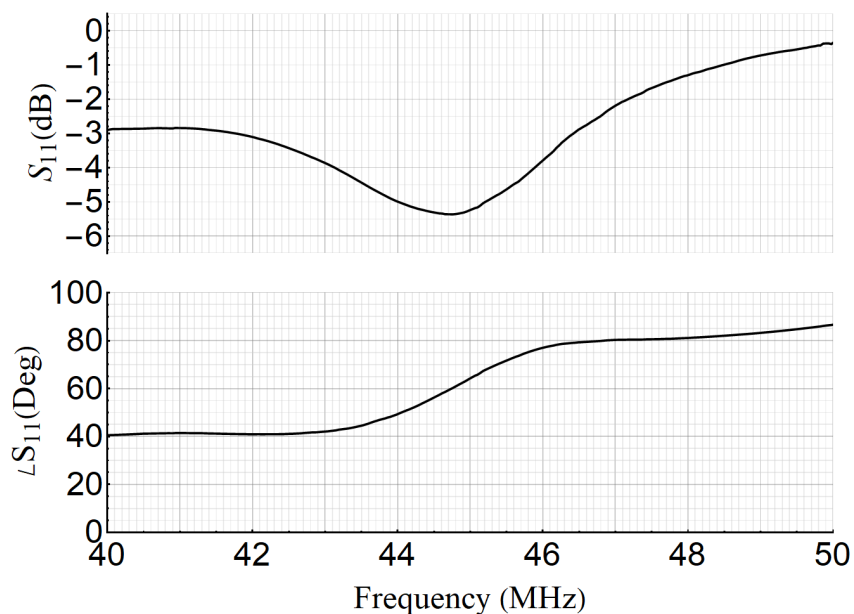


Figure 7.10: Experimental S_{11} measurements for the PZT4 sensor in air.

the viscous loading of liquids on the surface, and they would not interfere with the operation of the sensor. The error in the position of the S_{11} minima was found to be smaller than 3% when compared with the numerical results, Table 7.3. However, the DI water was found to have an enhanced frequency shift. This enhanced shift can be attributed to non-zero ionic concentrations in the DI water used or variations in its temperature while in operation and warrants further investigation in future work.

The results show a clear relation between the permittivity of the medium-under-test and the resonance frequency of the BG wave sensor. Furthermore, the shift due to the permittivity of medium-under-test from the natural frequency with the sensor in air is not linear. It depends on the sensitivity of the eigenvalue of the BG wave sensor, equation (4.16), to the ratio of the permittivity of the substrate to that of the medium-under-test, r . Moreover, the electrostrictive nonlinearity in the substrate affects the sensitivity. This could be further exacerbated under DC

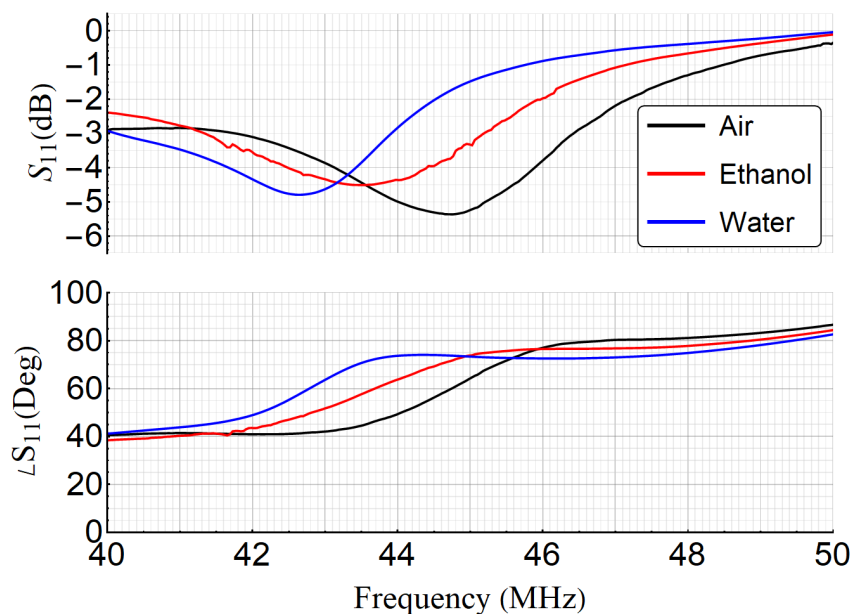


Figure 7.11: Experimental S_{11} measurements for the PZT4 sensor for different media-under-test.

Table 7.2: Statistical results of the experimental measurements of the resonances for the LiNbO_3 based sensor for different media-under-test.

Medium-under-test	Air	Ethanol	Diluted Ethanol (50%)	DI Water
Mean (MHz)	25.27	21.76	18.89	17.78
Standard deviation (MHz)	0.09	0.48	0.28	0.49

bias, as outlined in chapter 6.

It is also influenced by several other factors, and they must all be taken into consideration. The first factor is the effect of the partial metalization imposed by the IDT on the surface, which directly affects the wave confinement to the surface. The confinement degree can be charac-

Table 7.3: Comparison of theoretical with experimental natural frequencies for the LiNbO_3 sensor under different media-under-test.

Medium-under-test	Air	Ethanol	DI Water
Model (MHz)	24.54	22.09	20.73
Experiment (MHz)	25.27	21.76	17.78
Error	2.9%	-1.5%	-16.6%

terized using a Laser Doppler Vibrometer, as discussed in Section 5.3, in order to estimate the surface metalization constant ι . The second factor is the parasitic capacitance, which influences electrical measurements, such as S_{11} . The parasitic capacitance acts in parallel to the resonator

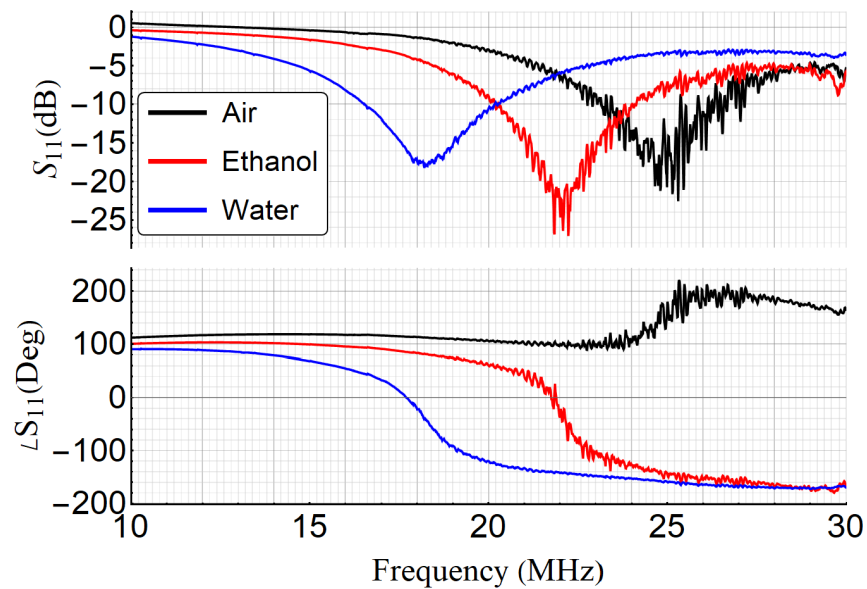


Figure 7.12: Experimental S_{11} measurements for the LiNbO_3 sensor for different media-under-test.

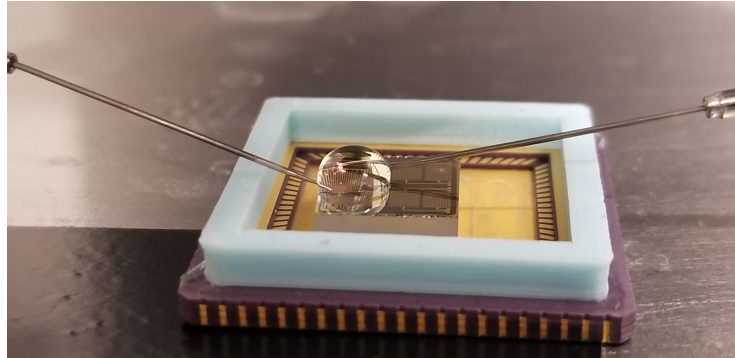


Figure 7.13: Probing of the LiNbO_3 sensor, with a DI water droplet covering its surface.

and must be considered, equation (5.6), in order to correctly predict the frequency response of the S_{11} parameter. Finally, the effect of the medium-under-test on the parasitic capacitor must be taken into consideration.

7.5 Summary

The full dynamic linear and nonlinear equations were solved after the expansion of the dynamic solution around the equilibrium solution, using the Galerkin Residuals method. The numerical time domain and frequency response of the model were presented and discussed. Finally, the experimental validation of the permittivity sensor was presented. The sensor operation was validated by comparing the frequency response of the sensor with air, ethanol, and DI water as media under test.

Chapter 8

Conclusion and Future Work

8.1 Conclusion

A novel frequency-shift permittivity sensor based on the Bleustein-Gulyaev wave resonator was proposed. The effective BG wave speed is close to acoustic speeds, and therefore the wave presents an attractive option to acoustically sense an electric property. This reduces both device size and operating frequencies by several orders of magnitude, allowing for a low-cost and compact sensor. The sensor prototypes were fabricated using both PZT4 and LiNbO₃ substrates, and the fabrication was performed by the author, in-house, at the QNC-Cleanroom.

The sensor was numerically modeled to include electrostrictive nonlinearities, and the simulation results were presented. Additionally, a linearized-parameters-approach was implemented as an approximate alternative. Sensitivity tuning of the sensor is achieved by tapping into the nonlinearities of the material. This can be done by applying a large DC voltage, driving it towards the electrostriction nonlinear regime. This affects the effective constants of the piezoelectric and thus the overall sensor sensitivity profile.

Towards that end, the static non-resonant response was analyzed, and the eigenvalues were investigated. The results were verified experimentally and published [2]. The nonlinear equilibrium equations were derived and solved under DC excitation using the Galerkin residuals method, a pseudo-arclength continuation method, and a secant predictor. The excitation voltage imposed by the IDT was empirically modeled through the charge distribution function.

The dynamic response of the sensor was also modeled and solved, and the frequency response curves were plotted. The nonlinear equations of motion of the sensor were derived using the Galerkin residuals method. The resulting differential-algebraic system of equation was reduced to index-0 and then solved using long-time integration. Numerical results show a clear dependence of the natural frequency of the resonator on the permittivity of the medium-under-test.

These results were experimentally validated through S-parameter measurements using a Vector Network Analyzer. Three materials were compared, namely, air, ethanol, and deionized water. It was found that the permittivity of the sample on top of the substrate surface influences the sensor eigenvalues and shifts the primary resonance frequency.

Finally, a novel detection scheme for shear-horizontal (in-plane) surface acoustic waves, SH-SAW, using a single degree of freedom Laser Doppler Vibrometer was theorized, simulated, and experimentally verified. The technique exploits the out-of-plane deformation appearing on the boundaries of the wave aperture as it propagates within. This out-of-plane motion is usually a fraction of the maximum shear displacement and can be detected using the vibrometer. This approach was also published [1]. This technique provides researchers with a quick and effective method to characterize shear-horizontal surface acoustic waves. It was also successful in estimating the in-plane displacement field decay rate into the substrate.

This work was completed with full-time involvement and was carried out solely by the author, under the supervision of the academic supervisors.

8.2 Future Work

The S-parameters of using deionized water as the medium-under-test with the BG wave sensor were found to have an enhanced frequency shift. This enhanced shift is attributed to contamination in the deionized water used. Even clean DI water will still be contaminated by the surface of the sensor. Moreover, variations in the DI water temperature while in operation will affect the measured permittivity. The first step is to obtain highly purified deionized water from another source and clean the sensor before each use. If the enhanced shift persists, then another approach is to build a setup that allows for temperature control and observe the resonance shift versus temperature. This must be compared to the temperature dependence of water permittivity from the literature.

DC voltage has been shown to enhance and tune the sensitivity of the BG wave permittivity sensor. However, aquatic-based media-under-test presents a challenge, as water tends to experience electrolysis. This is an open research challenge and would need to be further investigated. One proposal is to actuate the device far away from resonance, but not at DC, and consider the RMS value of the actuation signal as an equivalent to the DC effect. This approach holds promise, but is yet to be proven experimentally.

The quality factor measured experimentally for the sensors was 10, while typical BG-filters usually have quality factors in the order of few hundreds [20]. This was due to issues with the post-processing step in the microfabrication, where the laser trimmer was used to create the vertical trenches. The depth of the trenches must be increased to fully reflect the wave. However, the process must be done slowly to avoid any heat damage that may occur at the edges. An alternative solution is to develop a Deep Reactive Ion Etching (DRIE) recipe for PZT4 and LiNbO_3 to create the trenches while avoiding the heat damage resulting from laser trimmers.

Additionally, packaging for the sensor, including a fluidic enclosure, needs to be design and

built. The packaging needs to allow for fluids and/or gases to be applied to the sensitive sensor area without damaging the wiring or electronics. Moreover, the printed circuit board, PCB, must be designed with the circuit required to derive and read the output of the sensor. The sensor can be driven by a PLL [130], that can drive and track the resonance frequency of the resonant sensor. The circuit must give a readout indicating the tracked resonance frequency.

Finally, the approach described in section 5.3 and published in [1] for characterization of SH-SAW has been successfully used to identify the nonlinear shear-electrostrictive constant, $M = M_{14}$. Shear-electrostrictive constants are seldom reported in the literature, therefore, this technique can be used to identify such constants for an array of materials.

Bibliography

- [1] **Elhady, Alaa** and E. M. Abdel-Rahman, “Characterization of shear horizontal waves using a 1D laser Doppler vibrometer,” *Sensors*, vol. 21, no. 7, p. 2467, 2021.
- [2] **Elhady, Alaa**, M. Basha, and E. M. Abdel-Rahman, “Analysis of tunable Bleustein-Gulyaev permittivity sensors,” *Journal of Applied Physics*, vol. 129, no. 16, p. 164501, 2021.
- [3] **Elhady, Alaa**, M. Basha, and E. M. Abdel-Rahman, “Measurement of electric permittivity using Bleustein-Gulyaev wave sensors,” *Journal of Micromechanics and Microengineering*, 2021. In progress.
- [4] A. Safari and E. K. Akdogan, *Piezoelectric and acoustic materials for transducer applications*. Springer Science & Business Media, 2008.
- [5] J. L. Bleustein, “A new surface wave in piezoelectric materials,” *Applied Physics Letters*, vol. 13, no. 12, pp. 412–413, 1968.
- [6] Y. V. Gulyaev, “Electroacoustic surface waves in solids,” *ZhETF Pisma Redaktsiiu*, vol. 9, p. 63, 1969.

- [7] R. C. Rosenfeld, *Excitation and propagation of Bleustein-Gulyaev waves*. PhD thesis, Iowa State University, 1971.
- [8] R. F. Milsom, N. H. C. Reilly, and M. Redwood, "Analysis of generation and detection of surface and bulk acoustic waves by interdigital transducers," *IEEE Transactions on Sonics Ultrasonics*, vol. 24, pp. 147–166, 1977.
- [9] K.-y. Hashimoto, *Surface acoustic wave devices in telecommunications*, vol. 116. Springer, 2000.
- [10] F. L. Guo and R. Sun, "Propagation of Bleustein–Gulyaev wave in 6mm piezoelectric materials loaded with viscous liquid," *International Journal of Solids and Structures*, vol. 45, no. 13, pp. 3699–3710, 2008.
- [11] F. L. Guo, G. Q. Wang, and G. A. Rogerson, "Inverse determination of liquid viscosity by means of the Bleustein–Gulyaev wave," *International Journal of Solids and Structures*, vol. 49, no. 15, pp. 2115–2120, 2012.
- [12] P. Kielczyński, W. Pajewski, M. Szalewski, and A. Balcerzak, "Measurement of the shear storage modulus and viscosity of liquids using the Bleustein–Gulyaev wave," *Review of Scientific Instruments*, vol. 75, no. 7, pp. 2362–2367, 2004.
- [13] C. Zhang, J. J. Caron, and J. F. Vetelino, "The Bleustein–Gulyaev wave for liquid sensing applications," *Sensors and Actuators B: Chemical*, vol. 76, no. 1, pp. 64–68, 2001.
- [14] P. Kielczyński, M. Szalewski, A. Balcerzak, A. J. Rostocki, and D. B. Tefelski, "Application of SH surface acoustic waves for measuring the viscosity of liquids in function of pressure and temperature," *Ultrasonics*, vol. 51, no. 8, pp. 921–924, 2011.

- [15] B. D. Zaitsev, I. E. Kuznetsova, S. G. Joshi, and I. A. Borodina, "Acoustic waves in piezoelectric plates bordered with viscous and conductive liquid," *Ultrasonics*, vol. 39, no. 1, pp. 45–50, 2001.
- [16] I. Kuznetsova, V. Kolesov, V. Anisimkin, Z. Qian, F. Zhu, and A. Gorbunova, "Study of shear-horizontal waves in structure "piezoelectric-viscous and conductive liquid"," in *23rd International Congress on Acoustics*, 2019.
- [17] P. Kiel/czyński and R. Pl/owiec, "Determination of the shear impedance of viscoelastic liquids using love and Bleustein–Gulyaev surface waves," *The Journal of the Acoustical Society of America*, vol. 86, no. 2, pp. 818–827, 1989.
- [18] A. El Baroudi and J. Y. Le Pommellec, "Bleustein–Gulyaev waves in a finite piezoelectric material loaded with a viscoelastic fluid," *Wave Motion*, vol. 101, p. 102695, 2021.
- [19] K. Morozumi, M. Kadota, and S. Hayashi, "Characteristics of BGS wave resonators using ceramic substrates and their applications," in *Ultrasonics Symposium, 1996. Proceedings., 1996 IEEE*, vol. 1, pp. 81–86, IEEE, 1996.
- [20] M. Kadota, J. Ago, H. Horiuchi, and H. Morii, "Transversely coupled resonator filters utilizing reflection of Bleustein-Gulyaev-Shimizu wave at free edges of substrate," *Japanese Journal of Applied Physics*, vol. 39, no. 5S, p. 3045, 2000.
- [21] M. Kadota, J. Ago, H. Horiuchi, and M. Ikeura, "Very small IF resonator filters using reflection of shear horizontal wave at free edges of substrate," *IEEE transactions on ultrasonics, ferroelectrics, and frequency control*, vol. 49, no. 9, pp. 1269–1279, 2002.
- [22] M. Kadota, J. Ago, H. Horiuchi, and M. Ikeura, "Longitudinally coupled resonator filter using edge reflection of Bleustein-Gulyaev-Shimizu and shear horizontal waves with var-

- ious bandwidths realized by selecting substrates,” *Japanese Journal of Applied Physics*, vol. 40, no. 5S, p. 3722, 2001.
- [23] M. Kadota, J. Ago, and H. Horiuchi, “A Bleustein-Gulyaev-Shimizu wave resonator having resonances for TV and VCR traps,” *IEEE transactions on microwave theory and techniques*, vol. 44, no. 12, pp. 2758–2762, 1996.
- [24] J. T. M. Van Beek, P. G. Steeneken, and B. Giesbers, “A 10MHz piezoresistive MEMS resonator with high Q,” in *International Frequency Control Symposium and Exposition, 2006 IEEE*, pp. 475–480, IEEE, 2006.
- [25] M. Sanbi, E. L. Essoufi, and M. Rahmoune, “Gyroscopic effect and temperature on surface acoustic waves propagating in a thermo-piezoelectric half space,” *International Journal of Solids and Structures*, vol. 37, pp. 4933–4947, 2009.
- [26] H. Fang, J. Yang, and Q. Jiang, “Gyroscopic effect on surface waves in piezoelectrics,” in *Ultrasonics Symposium, 1999. Proceedings. 1999 IEEE*, vol. 1, pp. 497–500, IEEE, 1999.
- [27] H. Fang, J. Yang, and Q. Jiang, “Rotation-perturbed surface acoustic waves propagating in piezoelectric crystals,” *International Journal of Solids and Structures*, vol. 37, no. 36, pp. 4933–4947, 2000.
- [28] Y.-H. Zhou and Q. Jiang, “Effects of coriolis force and centrifugal force on acoustic waves propagating along the surface of a piezoelectric half-space,” *Zeitschrift für Angewandte Mathematik und Physik (ZAMP)*, vol. 52, no. 6, pp. 950–965, 2001.
- [29] F. Alshaikh, “Electromechanical coupling of Bleustein–Gulyaev wave propagation in rotating prestressed piezoelectric layered materials,” *Continuum Mechanics and Thermodynamics*, vol. 32, no. 3, pp. 749–759, 2020.

- [30] K. Nakamura, "Piezoelectric applications of ferroelectric single crystals," in *Applications of Ferroelectrics, 2002. ISAF 2002. Proceedings of the 13th IEEE International Symposium on*, pp. 389–394, IEEE, 2002.
- [31] D. Ivanov, "BioMEMS sensor systems for bacterial infection detection," *Biodrugs*, vol. 20, no. 6, pp. 351–356, 2006.
- [32] M. A. L. A. Ganguly, "Bleustein-Gulyaev waves in a pre-stressed piezoelectric half space," in *Proc. Indian Acad. Sci., Sect. A*, vol. 50, pp. 375–381, 1984.
- [33] J. S. Yang, "Bleustein-Gulyaev waves in strained piezoelectric ceramics," *Mechanics Research Communications*, vol. 28, no. 6, pp. 679–683, 2001.
- [34] H. Liu, Z. B. Kuang, and Z. M. Cai, "Propagation of Bleustein–Gulyaev waves in a pre-stressed layered piezoelectric structure," *Ultrasonics*, vol. 41, no. 5, pp. 397–405, 2003.
- [35] T. I. Belyankova and V. V. Kalinchuk, "Shear horizontal waves in piezoelectric structures with a functionally graded coating," *Mechanics of Advanced Materials and Structures*, vol. 28, no. 5, pp. 486–494, 2021.
- [36] P. Li and F. Jin, "Bleustein–Gulyaev waves in a transversely isotropic piezoelectric layered structure with an imperfectly bonded interface," *Smart Materials and Structures*, vol. 21, no. 4, p. 045009, 2012.
- [37] C. Maerfeld, F. Gires, and P. Tournois, "Bleustein-Gulyaev surface wave amplification in CdS," *Applied Physics Letters*, vol. 18, no. 7, pp. 269–272, 1971.
- [38] G. Cambon, C. Fournier, and M. Rouzeyre, "Bleustein-wave amplification in photoconducting CdS," *Electronics Letters*, vol. 8, no. 3, pp. 60–62, 1972.

- [39] M. Ganguly and A. K. Pal, "Amplification of BG waves in a pre-stressed piezoelectric half space of hexagonal symmetry," *Acta Physica Hungarica*, vol. 63, no. 3, pp. 321–329, 1988.
- [40] N. Kalyanasundaram, "Non-linear propagation characteristics of Bleustein-Gulyaev waves," *Journal of Sound and Vibration*, vol. 96, no. 4, pp. 411–420, 1984.
- [41] A. Wolski, "Theory of electromagnetic fields," *arXiv preprint arXiv:1111.4354*, 2011.
- [42] J. R. Birchak, C. G. Gardner, J. E. Hipp, and J. M. Victor, "High dielectric constant microwave probes for sensing soil moisture," *Proceedings of the IEEE*, vol. 62, no. 1, pp. 93–98, 1974.
- [43] K. Brock and D. Stoakes, "Oil permittivity sensor," July 1973. US Patent 3,746,974.
- [44] K. Folgero, T. Friiso, J. Hilland, and T. Tjomsland, "A broad-band and high-sensitivity dielectric spectroscopy measurement system for quality determination of low-permittivity fluids," *Measurement Science and Technology*, vol. 6, no. 7, p. 995, 1995.
- [45] G. Smith, A. P. Duffy, J. Shen, and C. J. Olliff, "Dielectric relaxation spectroscopy and some applications in the pharmaceutical sciences," *Journal of pharmaceutical sciences*, vol. 84, no. 9, pp. 1029–1044, 1995.
- [46] W. Ellison, A. Balana, G. Delbos, K. Lamkaouchi, L. Eymard, C. Guillou, and C. Prigent, "New permittivity measurements of seawater," *Radio science*, vol. 33, no. 3, pp. 639–648, 1998.
- [47] T. Meissner and F. J. Wentz, "The complex dielectric constant of pure and sea water from microwave satellite observations," *IEEE Transactions on Geoscience and remote Sensing*, vol. 42, no. 9, pp. 1836–1849, 2004.

- [48] A. Taeb, M. A. Basha, S. Gigoyan, M. Marsden, and S. Safavi-Naeini, "Label-free DNA sensing using millimeter-wave silicon WGM resonator," *Optics express*, vol. 21, no. 17, pp. 19467–19472, 2013.
- [49] B. Laemmle, K. Schmalz, J. C. Scheytt, R. Weigel, and D. Kissinger, "A 125-GHz permittivity sensor with read-out circuit in a 250-nm SiGe BiCMOS technology," *IEEE Transactions on Microwave Theory and Techniques*, vol. 61, no. 5, pp. 2185–2194, 2013.
- [50] T. Chen, D. Dubuc, M. Poupot, J.-J. Fournie, and K. Grenier, "Accurate nanoliter liquid characterization up to 40 GHz for biomedical applications: Toward noninvasive living cells monitoring," *IEEE Transactions on Microwave Theory and Techniques*, vol. 60, no. 12, pp. 4171–4177, 2012.
- [51] S. Gabriel, R. W. Lau, and C. Gabriel, "The dielectric properties of biological tissues: II. measurements in the frequency range 10 hz to 20 GHz," *Physics in medicine and biology*, vol. 41, no. 11, p. 2251, 1996.
- [52] U. Khan, N. Al-Moayed, N. Nguyen, M. Obol, K. Korolev, M. Afsar, and S. Naber, "High frequency dielectric characteristics of tumorous and non-tumorous breast tissues," in *Microwave Symposium, 2007. IEEE/MTT-S International*, pp. 1341–1344, IEEE, 2007.
- [53] G. Qiao, W. Wang, W. Duan, F. Zheng, A. J. Sinclair, and C. R. Chatwin, "Bioimpedance analysis for the characterization of breast cancer cells in suspension," *IEEE Transactions on biomedical engineering*, vol. 59, no. 8, pp. 2321–2329, 2012.
- [54] E. H. Grant, V. E. R. McClean, N. R. V. Nightingale, R. J. Sheppard, and M. J. Chapman, "Dielectric behavior of water in biological solutions: Studies on myoglobin, human low-density lipoprotein, and polyvinylpyrrolidone," *Bioelectromagnetics*, vol. 7, no. 2, pp. 151–162, 1986.

- [55] M. Hofmann, G. Fischer, R. Weigel, and D. Kissinger, "Microwave-based noninvasive concentration measurements for biomedical applications," *IEEE Transactions on Microwave Theory and Techniques*, vol. 61, no. 5, pp. 2195–2204, 2013.
- [56] F. I. Jamal, S. Guha, M. H. Eissa, J. Borngräber, C. Meliani, H. J. Ng, D. Kissinger, and J. Wessel, "Low-power miniature k -band sensors for dielectric characterization of biomaterials," *IEEE Transactions on Microwave Theory and Techniques*, vol. 65, no. 3, pp. 1012–1023, 2017.
- [57] F. V. D. Touw, J. W. H. Briede, and M. Mandel, "Electric permittivity of alfalfa mosaic virus in aqueous solutions," *Biopolymers: Original Research on Biomolecules*, vol. 12, no. 1, pp. 111–119, 1973.
- [58] M. P. Hughes, H. Morgan, and F. J. Rixon, "Measuring the dielectric properties of herpes simplex virus type 1 virions with dielectrophoresis," *Biochimica et Biophysica Acta (BBA)-General Subjects*, vol. 1571, no. 1, pp. 1–8, 2002.
- [59] S. Chen, F. Zhou, K. Xu, P. Zhao, Y. Yang, X. Zhu, and G. Wang, "A portable microwave interferometry sensor for permittivity detection based on CCMRC," *IEEE Access*, vol. 8, pp. 140323–140332, 2020.
- [60] S. Kiani, P. Rezaei, and M. Navaei, "Dual-sensing and dual-frequency microwave SRR sensor for liquid samples permittivity detection," *Measurement*, vol. 160, p. 107805, 2020.
- [61] A. Bhardwaj, D. Pratap, K. V. Srivastava, and S. A. Ramakrishna, "Highly sensitive permittivity sensor using an inhomogeneous metamaterial cylindrical waveguide," *IEEE Sensors Journal*, vol. 21, no. 7, pp. 9120–9127, 2021.

- [62] M. Karami, P. Rezaei, S. Kiani, and R. A. Sadeghzadeh, "Modified planar sensor for measuring dielectric constant of liquid materials," *Electronics Letters*, vol. 53, no. 19, pp. 1300–1302, 2017.
- [63] G. Vlachogiannakis, Z. Hu, H. T. Shivamurthy, A. Neto, M. A. P. Pertijs, L. C. N. De Vreede, and M. Spirito, "Miniaturized broadband microwave permittivity sensing for biomedical applications," *IEEE Journal of Electromagnetics, RF and Microwaves in Medicine and Biology*, vol. 3, no. 1, pp. 48–55, 2018.
- [64] O. Elhadidy, M. Elkholy, A. A. Helmy, S. Palermo, and K. Entesari, "A CMOS fractional- n PLL-based microwave chemical sensor with 1.5% permittivity accuracy," *IEEE Transactions on Microwave Theory and Techniques*, vol. 61, no. 9, pp. 3402–3416, 2013.
- [65] M. M. Bajestan, A. A. Helmy, H. Hedayati, and K. Entesari, "A 0.62–10 GHz complex dielectric spectroscopy system in CMOS," *IEEE Transactions on Microwave Theory and Techniques*, vol. 62, no. 12, pp. 3522–3537, 2014.
- [66] O. Elhadidy, S. Shakib, K. Krenek, S. Palermo, and K. Entesari, "A wide-band fully-integrated CMOS ring-oscillator PLL-based complex dielectric spectroscopy system," *IEEE Transactions on Circuits and Systems I: Regular Papers*, vol. 62, no. 8, pp. 1940–1949, 2015.
- [67] E. Fratticcioli, M. Dionigi, and R. Sorrentino, "A simple and low-cost measurement system for the complex permittivity characterization of materials," *IEEE Transactions on Instrumentation and Measurement*, vol. 53, no. 4, pp. 1071–1077, 2004.
- [68] W. Withayachumnankul, K. Jaruwongrungee, A. Tuantranont, C. Fumeaux, and D. Abbott, "Metamaterial-based microfluidic sensor for dielectric characterization," *Sensors and Actuators A: Physical*, vol. 189, pp. 233–237, 2013.

- [69] M. Islam, S. J. M. Rao, G. Kumar, B. P. Pal, and D. R. Chowdhury, "Role of resonance modes on terahertz metamaterials based thin film sensors," *Scientific Reports*, vol. 7, no. 1, pp. 1–8, 2017.
- [70] L. Su, J. Mata-Contreras, P. Vélez, A. Fernández-Prieto, and F. Martín, "Analytical method to estimate the complex permittivity of oil samples," *Sensors*, vol. 18, no. 4, p. 984, 2018.
- [71] B. D. Wiltshire, T. Zarifi, and M. H. Zarifi, "Passive split ring resonator tag configuration for RFID-based wireless permittivity sensing," *IEEE Sensors Journal*, vol. 20, no. 4, pp. 1904–1911, 2019.
- [72] E. L. Chuma, Y. Iano, G. Fontgalland, L. L. B. Roger, and H. Loschi, "PCB-integrated non-destructive microwave sensor for liquid dielectric spectroscopy based on planar metamaterial resonator," *Sensors and Actuators A: Physical*, vol. 312, p. 112112, 2020.
- [73] S. O. Nelson, W. R. Forbus, K. C. Lawrence, *et al.*, "Assessment of microwave permittivity for sensing peach maturity," *Transactions of the ASAE*, vol. 38, no. 2, pp. 579–585, 1995.
- [74] S. O. Nelson, W.-c. Guo, S. Trabelsi, and S. J. Kays, "Dielectric spectroscopy of watermelons for quality sensing," *Measurement Science and Technology*, vol. 18, no. 7, p. 1887, 2007.
- [75] V. Turgul and I. Kale, "Characterization of the complex permittivity of glucose/water solutions for noninvasive RF/microwave blood glucose sensing," in *2016 IEEE International Instrumentation and Measurement Technology Conference Proceedings*, pp. 1–5, IEEE, 2016.
- [76] A. Ebrahimi, J. Scott, and K. Ghorbani, "Ultrahigh-sensitivity microwave sensor for microfluidic complex permittivity measurement," *IEEE Transactions on Microwave Theory and Techniques*, vol. 67, no. 10, pp. 4269–4277, 2019.

- [77] A. Alu and N. Engheta, “Dielectric sensing in ϵ -near-zero narrow waveguide channels,” *Physical Review B*, vol. 78, no. 4, p. 045102, 2008.
- [78] J. Muñoz-Enano, J. Martel, P. Vélez, F. Medina, L. Su, and F. Martín, “Parametric analysis of the edge capacitance of uniform slots and application to frequency-variation permittivity sensors,” *Applied Sciences*, vol. 11, no. 15, p. 7000, 2021.
- [79] T. Chretiennot, D. Dubuc, and K. Grenier, “A microwave and microfluidic planar resonator for efficient and accurate complex permittivity characterization of aqueous solutions,” *IEEE Transactions on Microwave Theory and Techniques*, vol. 61, no. 2, pp. 972–978, 2012.
- [80] C. D. Ellis, J. L. Davidson, and T. A. Baginski, “Microelectronic moisture sensor from variable dielectric capacitances of polyimide film,” in *Proceedings., Eighth University/Government/Industry Microelectronics Symposium*, pp. 87–91, IEEE, 1989.
- [81] A. Risos, N. Long, A. Hunze, and G. Gouws, “Interdigitated sensors: A design principle for accurately measuring the permittivity of industrial oils,” *IEEE Sensors Journal*, vol. 17, no. 19, pp. 6232–6239, 2017.
- [82] H. Lobato-Morales, A. Corona-Chávez, J. L. Olvera-Cervantes, R. A. Chávez-Pérez, and J. L. Medina-Monroy, “Wireless sensing of complex dielectric permittivity of liquids based on the RFID,” *IEEE Transactions on Microwave Theory and Techniques*, vol. 62, no. 9, pp. 2160–2167, 2014.
- [83] F. Costa, A. Gentile, S. Genovesi, L. Buoncristiani, A. Lazaro, R. Villarino, and D. Girbau, “A depolarizing chipless RF label for dielectric permittivity sensing,” *IEEE Microwave and Wireless Components Letters*, vol. 28, no. 5, pp. 371–373, 2018.

- [84] Y. T. Hu, J. S. Yang, and Q. Jiang, "Surface waves in electrostrictive materials under biasing fields," *Zeitschrift für Angewandte Mathematik und Physik (ZAMP)*, vol. 55, no. 4, pp. 678–700, 2004.
- [85] I. E. Kuznetsova, B. D. Zaitsev, P. V. Polyakov, and M. B. Mysenko, "External electric field effect on the properties of Bleustein-Gulyaev surface acoustic waves in lithium niobate and strontium titanate," *Ultrasonics*, vol. 36, no. 1-5, pp. 431–434, 1998.
- [86] J. Coromina, J. Muñoz-Enano, P. Vélez, A. Ebrahimi, J. Scott, K. Ghorbani, and F. Martín, "Permittivity sensor based on a slow-wave artificial transmission line," in *2020 Fourteenth International Congress on Artificial Materials for Novel Wave Phenomena (Metamaterials)*, pp. 069–071, IEEE, 2020.
- [87] J. S. Yang, "Bleustein-Gulyaev waves in piezoelectromagnetic materials," *International Journal of Applied Electromagnetics and Mechanics*, vol. 12, no. 3, 4, pp. 235–240, 2000.
- [88] P. Li, F. Jin, and Z. Qian, "Propagation of the Bleustein–Gulyaev waves in a functionally graded transversely isotropic electro-magneto-elastic half-space," *European Journal of Mechanics-A/Solids*, vol. 37, pp. 17–23, 2013.
- [89] J. W. Waanders, *Piezoelectric ceramics: properties and applications*. NV Philips' Gloeilampenfabrieken, 1991.
- [90] A. Amin, M. J. Haun, B. Badger, H. McKinstry, and L. E. Cross, "A phenomenological Gibbs function for the single cell region of the PbZrO_3 : PbTiO_3 solid solution system," *Ferroelectrics*, vol. 65, no. 1, pp. 107–130, 1985.
- [91] Y. Liu, K. L. Ren, H. F. Hofmann, and Q. Zhang, "Investigation of electrostrictive polymers for energy harvesting," *IEEE transactions on ultrasonics, ferroelectrics, and frequency control*, vol. 52, no. 12, pp. 2411–2417, 2005.

- [92] K. Uchino, *Ferroelectric Devices 2nd Edition*. CRC press, 2009.
- [93] I. D. Avramov, “1 GHz low loss coupled resonator filter using surface skimming bulk waves and Bleustein-Gulyaev waves,” *Electronics letters*, vol. 27, no. 5, pp. 414–415, 1991.
- [94] A. K. Namdeo and H. B. Nemade, “Simulation on effects of electrical loading due to interdigital transducers in surface acoustic wave resonator,” *Procedia Engineering*, vol. 64, pp. 322–330, 2013.
- [95] A. Venema, *Transduction and propagation of surface acoustic waves in three-layered media with an electrically conductive substrate*. PhD thesis, TU Delft, Delft University of Technology, 1980.
- [96] A. J. Slobodnik, “Surface acoustic waves and SAW materials,” *Proceedings of the IEEE*, vol. 64, no. 5, pp. 581–595, 1976.
- [97] “American Piezo Ceramics: Properties Of Materials.”
<https://www.americanpiezo.com/apc-materials/piezoelectric-properties.html>. Accessed: 2020-12-23.
- [98] B. Collet, M. Destrade, and G. A. Maugin, “Bleustein–Gulyaev waves in some functionally graded materials,” *European Journal of Mechanics-A/Solids*, vol. 25, no. 5, pp. 695–706, 2006.
- [99] K. Nakamura, “Shear-horizontal piezoelectric surface acoustic waves,” *Japanese Journal of Applied Physics*, vol. 46, no. 7S, p. 4421, 2007.
- [100] “Boston Piezo Optics.”
<https://www.bostonpiezooptics.com/lithium-niobate>. Accessed: 2021-05-06.

- [101] M. Kadota, T. Yoneda, K. Fujimoto, T. Nakao, and E. Takata, "Resonator filters using shear horizontal-type leaky surface acoustic wave consisting of heavy-metal electrode and quartz substrate," *IEEE transactions on ultrasonics, ferroelectrics, and frequency control*, vol. 51, no. 2, pp. 202–210, 2004.
- [102] N. Smagin, L. Djoumi, E. Herth, M. Vanotti, D. Fall, V. Blondeau-Patissier, M. Duquenois, and M. Ouafouh, "Fast time-domain laser Doppler vibrometry characterization of surface acoustic waves devices," *Sensors and Actuators A: Physical*, vol. 264, pp. 96–106, 2017.
- [103] W. Yuan, J. Zhao, D. Zhang, and Z. Zhong, "Measurement of surface acoustic wave using air coupled transducer and laser Doppler vibrometer," in *Proceedings of the 21st International Conference on Composite Materials, Xian, China*, pp. 20–25, Chinese Society for Composite Materials, 2017.
- [104] A. Miyamoto, S. I. Wakana, and A. Ito, "Novel optical observation technique for shear horizontal wave in SAW resonators on 42°/spl deg/YX-cut lithium tantalate," in *2002 IEEE Ultrasonics Symposium, 2002. Proceedings.*, vol. 1, pp. 89–92, IEEE, 2002.
- [105] M.-G. Kim, K. Jo, H.-S. Kwon, W. Jang, Y. Park, and J.-H. Lee, "Fiber-optic laser Doppler vibrometer to dynamically measure MEMS actuator with in-plane motion," *Journal of Microelectromechanical Systems*, vol. 18, no. 6, pp. 1365–1370, 2009.
- [106] M. Arabi, M. Gopanchuk, E. Abdel-Rahman, and M. Yavuz, "Measurement of in-plane motions in MEMS," *Sensors*, vol. 20, no. 12, p. 3594, 2020.
- [107] V. Plessky, W. Wang, H. Wang, H. Wu, and Y. Shui, "P2M-4 optimization of STW resonator by using FEM/BEM," in *2006 IEEE Ultrasonics Symposium*, pp. 1863–1865, IEEE, 2006.

- [108] M. Mimura, D. Ajima, C. Konoma, and T. Murase, "Small sized band 20 SAW duplexer using low acoustic velocity rayleigh SAW on LiNbO₃ substrate," in *2017 IEEE International Ultrasonics Symposium (IUS)*, pp. 1–4, IEEE, 2017.
- [109] R. Kowarsch, W. Ochs, M. Giesen, A. Dräbenstedt, M. Winter, and C. Rembe, "Real-time 3D vibration measurements in microstructures," in *Optical Micro-and Nanometrology IV*, vol. 8430, p. 84300C, International Society for Optics and Photonics, 2012.
- [110] Y. Chiba, T. Ebihara, K. Mizutani, and N. Wakatsuki, "Measurement of Love wave propagation characteristics along elastic substrate and viscoelastic surface layer," in *Proceedings of Symposium on Ultrasonic Electronics*, vol. 37, 2016.
- [111] J. Ayers, N. Apetre, M. Ruzzene, and K. Sabra, "Measurement of Lamb wave polarization using a one-dimensional scanning laser vibrometer (I)," *The Journal of the Acoustical Society of America*, vol. 129, no. 2, pp. 585–588, 2011.
- [112] T. E. Schmidt, J. Tyson, K. Galanulis, D. M. Revilock, and M. E. Melis, "Full-field dynamic deformation and strain measurements using high-speed digital cameras," in *26th International Congress on High-Speed Photography and Photonics*, vol. 5580, pp. 174–185, International Society for Optics and Photonics, 2005.
- [113] D. A. Ehrhardt, M. S. Allen, S. Yang, and T. J. Beberniss, "Full-field linear and non-linear measurements using continuous-scan laser Doppler vibrometry and high speed three-dimensional digital image correlation," *Mechanical Systems and Signal Processing*, vol. 86, pp. 82–97, 2017.
- [114] Z. Butt, Z. Anjum, A. Sultan, F. Qayyum, H. M. K. Ali, and S. Mehmood, "Investigation of electrical properties & mechanical quality factor of piezoelectric material (PZT-4A)," *Journal of Electrical Engineering & Technology*, vol. 12, no. 2, pp. 846–851, 2017.

- [115] F. Caspers, “RF engineering basic concepts: S-parameters,” *CERN Yellow Report CERN-2011-007*, pp. 67-93, pp. 67–78, Jan. 2012.
- [116] W. Soluch, “Scattering matrix approach to one-port SAW resonators,” *IEEE transactions on ultrasonics, ferroelectrics, and frequency control*, vol. 47, no. 6, pp. 1615–1618, 2000.
- [117] P. N. Kambali and A. K. Pandey, “Capacitance and force computation due to direct and fringing effects in MEMS/NEMS arrays,” *IEEE Sensors Journal*, vol. 16, no. 2, pp. 375–382, 2015.
- [118] D. A. DeAngelis and G. W. Schulze, “Performance of PZT8 versus PZT4 piezoceramic materials in ultrasonic transducers,” *Physics Procedia*, vol. 87, pp. 85–92, 2016.
- [119] S. Gong and G. Piazza, “Laterally vibrating lithium niobate MEMS resonators with high electromechanical coupling and quality factor,” in *2012 IEEE International Ultrasonics Symposium*, pp. 1051–1054, IEEE, 2012.
- [120] L. Meirovitch, *Fundamentals of Vibrations*. McGraw-Hill, 2001.
- [121] W. R. Inc., “Mathematica.”
<https://www.wolfram.com/mathematica>. Accessed: 2020-12-23.
- [122] Y. Cho, “Determination of electrostrictive and third-order dielectric constants of piezoelectric ceramic,” *Japanese Journal of Applied Physics*, vol. 39, no. 6R, p. 3524, 2000.
- [123] A. H. Nayfeh and B. Balachandran, *Applied nonlinear dynamics: analytical, computational, and experimental methods*. John Wiley & Sons, 2008.
- [124] H. Bhugra and G. Piazza, *Piezoelectric MEMS resonators*. Springer, 2017.

- [125] M. I. Younis, *MEMS linear and nonlinear statics and dynamics*, vol. 20. Springer Science & Business Media, 2011.
- [126] A. K. Jonscher, "The 'universal' dielectric response," *nature*, vol. 267, no. 5613, pp. 673–679, 1977.
- [127] B. M. A. Rahman and S. Haxha, "Optimization of microwave properties for ultrahigh-speed etched and unetched lithium niobate electrooptic modulators," *Journal of lightwave technology*, vol. 20, no. 10, p. 1856, 2002.
- [128] S. M. Puranik, A. C. Kumbharkhane, and S. C. Mehrotra, "Temperature dependent dielectric studies of ethanol and ethylene glycol using time domain reflectometry," *Indian J. Phys. B*, vol. 67, pp. 9–13, 1993.
- [129] U. Kaatze, "Complex permittivity of water as a function of frequency and temperature," *Journal of Chemical and Engineering Data*, vol. 34, no. 4, pp. 371–374, 1989.
- [130] C. Gokcek, "Tracking the resonance frequency of a series RLC circuit using a phase locked loop," in *Proceedings of 2003 IEEE Conference on Control Applications, 2003. CCA 2003.*, vol. 1, pp. 609–613, IEEE, 2003.
- [131] S. N. Jiang, Q. Jiang, X. F. Li, S. H. Guo, H. G. Zhou, and J. S. Yang, "Piezoelectromagnetic waves in a ceramic plate between two ceramic half-spaces," *International Journal of Solids and Structures*, vol. 43, no. 18, pp. 5799–5810, 2006.
- [132] R. S. Weis and T. K. Gaylord, "Lithium niobate: summary of physical properties and crystal structure," *Applied Physics A*, vol. 37, no. 4, pp. 191–203, 1985.

- [133] J. A. Kosinski, A. Ballato, and Y. Lu, “Pure-mode measurements of dilithium tetraborate material properties,” in *Frequency Control Symposium, 1993. 47th., Proceedings of the 1993 IEEE International*, pp. 359–370, IEEE, 1993.
- [134] D. G. Piliposyan, K. B. Ghazaryan, G. T. Piliposian, and A. S. Avetisyan, “Wave propagation in periodic piezoelectric elastic waveguides,” in *ASME 2012 Conference on Smart Materials, Adaptive Structures and Intelligent Systems*, pp. 1–9, American Society of Mechanical Engineers, 2012.
- [135] A. A. Alvarez-Mesquida, R. Rodriguez-Ramos, F. Comas, G. Monsivais, and R. Esquivel-Sirvent, “Scattering of shear horizontal piezoelectric waves in piezocomposite media,” *Journal of Applied Physics*, vol. 89, no. 5, pp. 2886–2892, 2001.
- [136] A. Authier, “Introduction to the properties of tensors,” in *International Tables for Crystallography Volume D: Physical properties of crystals*, pp. 3–33, Springer, 2006.

Appendices

Appendix A

Material Constants

Table A.1: Properties of different material considered for the permittivity sensor substrate.

Property	PZT4 [97, 131]	LiNbO ₃ [100, 132]	BaTiO ₃ [131]	Li ₂ B ₄ O ₇ [133]	LiTO ₃ [134]	PZT5 [131]	PZT6B [131]	PZT7A [131]	PZT7 [131]	ZnO [135]
G [GPa]	25.6	59.5	43.9	57.1	17.8	21.1	35.5	25.3	25	42.47
e [N/(Vm)]	12.7	4.1	11.6	0.39	0.89	12.3	4.6	9.2	13.5	-0.48
$\epsilon \times 8.85$ $\times 10^{-12}$ [F/m]	718	44	1109.6	8.66	7.27	916.4	406.8	459.9	1932.2	8.55
ρ [Kg/m ³]	7600	4647	5700	2432	3402	7750	7550	7600	7800	5680

Appendix B

Tensor Manipulations

Voigt reduction of a higher order tensor into a matrix form [136], and the reverse un-reduction for the two cases encountered by this work are as follows:

For 3x3 tensors, like stress, the process is defined, provided there is diagonal symmetry, such as:

$$\begin{pmatrix} \gamma_{11} & \gamma_{12} & \gamma_{13} \\ \gamma_{21} & \gamma_{22} & \gamma_{23} \\ \gamma_{31} & \gamma_{32} & \gamma_{33} \end{pmatrix} = \begin{pmatrix} \gamma_1 & \gamma_6 & \gamma_5 \\ \gamma_6 & \gamma_2 & \gamma_4 \\ \gamma_5 & \gamma_4 & \gamma_3 \end{pmatrix} \Leftrightarrow \begin{pmatrix} \gamma_1 \\ \gamma_2 \\ \gamma_3 \\ \gamma_4 \\ \gamma_5 \\ \gamma_6 \end{pmatrix}$$

For all tensors other than the stress tensor the definition is slightly different, as there is an half multiplicand in the definition of the non diagonal terms. For a 3x3x3x3 tensor reduced to a 6x6

matrix, like in the case of the stiffness or the electrostrictive constant tensors:

$$\begin{pmatrix}
 \begin{pmatrix} \Gamma_{1111} & \Gamma_{2111} & \Gamma_{3111} \\ \Gamma_{1112} & \Gamma_{2112} & \Gamma_{3112} \\ \Gamma_{1113} & \Gamma_{2113} & \Gamma_{3113} \end{pmatrix} &
 \begin{pmatrix} \Gamma_{1121} & \Gamma_{2121} & \Gamma_{3121} \\ \Gamma_{1122} & \Gamma_{2122} & \Gamma_{3122} \\ \Gamma_{1123} & \Gamma_{2123} & \Gamma_{3123} \end{pmatrix} &
 \begin{pmatrix} \Gamma_{1131} & \Gamma_{2131} & \Gamma_{3131} \\ \Gamma_{1132} & \Gamma_{2132} & \Gamma_{3132} \\ \Gamma_{1133} & \Gamma_{2133} & \Gamma_{3133} \end{pmatrix} \\
 \begin{pmatrix} \Gamma_{1211} & \Gamma_{2211} & \Gamma_{3211} \\ \Gamma_{1212} & \Gamma_{2212} & \Gamma_{3212} \\ \Gamma_{1213} & \Gamma_{2213} & \Gamma_{3213} \end{pmatrix} &
 \begin{pmatrix} \Gamma_{1221} & \Gamma_{2221} & \Gamma_{3221} \\ \Gamma_{1222} & \Gamma_{2222} & \Gamma_{3222} \\ \Gamma_{1223} & \Gamma_{2223} & \Gamma_{3223} \end{pmatrix} &
 \begin{pmatrix} \Gamma_{1231} & \Gamma_{2231} & \Gamma_{3231} \\ \Gamma_{1232} & \Gamma_{2232} & \Gamma_{3232} \\ \Gamma_{1233} & \Gamma_{2233} & \Gamma_{3233} \end{pmatrix} \\
 \begin{pmatrix} \Gamma_{1311} & \Gamma_{2311} & \Gamma_{3311} \\ \Gamma_{1312} & \Gamma_{2312} & \Gamma_{3312} \\ \Gamma_{1313} & \Gamma_{2313} & \Gamma_{3313} \end{pmatrix} &
 \begin{pmatrix} \Gamma_{1321} & \Gamma_{2321} & \Gamma_{3321} \\ \Gamma_{1322} & \Gamma_{2322} & \Gamma_{3322} \\ \Gamma_{1323} & \Gamma_{2323} & \Gamma_{3323} \end{pmatrix} &
 \begin{pmatrix} \Gamma_{1331} & \Gamma_{2331} & \Gamma_{3331} \\ \Gamma_{1332} & \Gamma_{2332} & \Gamma_{3332} \\ \Gamma_{1333} & \Gamma_{2333} & \Gamma_{3333} \end{pmatrix}
 \end{pmatrix}$$

$$= \begin{pmatrix}
 \begin{pmatrix} \Gamma_{11} & \Gamma_{61} & \Gamma_{51} \\ \Gamma_{16} & \Gamma_{66} & \Gamma_{56} \\ \Gamma_{15} & \Gamma_{65} & \Gamma_{55} \end{pmatrix} &
 \begin{pmatrix} \Gamma_{16} & \Gamma_{66} & \Gamma_{56} \\ \Gamma_{12} & \Gamma_{62} & \Gamma_{52} \\ \Gamma_{14} & \Gamma_{64} & \Gamma_{54} \end{pmatrix} &
 \begin{pmatrix} \Gamma_{15} & \Gamma_{65} & \Gamma_{55} \\ \Gamma_{14} & \Gamma_{64} & \Gamma_{54} \\ \Gamma_{13} & \Gamma_{63} & \Gamma_{53} \end{pmatrix} \\
 \begin{pmatrix} \Gamma_{61} & \Gamma_{21} & \Gamma_{41} \\ \Gamma_{66} & \Gamma_{26} & \Gamma_{46} \\ \Gamma_{65} & \Gamma_{25} & \Gamma_{45} \end{pmatrix} &
 \begin{pmatrix} \Gamma_{66} & \Gamma_{26} & \Gamma_{46} \\ \Gamma_{62} & \Gamma_{22} & \Gamma_{42} \\ \Gamma_{64} & \Gamma_{24} & \Gamma_{44} \end{pmatrix} &
 \begin{pmatrix} \Gamma_{65} & \Gamma_{25} & \Gamma_{45} \\ \Gamma_{64} & \Gamma_{24} & \Gamma_{44} \\ \Gamma_{63} & \Gamma_{23} & \Gamma_{43} \end{pmatrix} \\
 \begin{pmatrix} \Gamma_{51} & \Gamma_{41} & \Gamma_{31} \\ \Gamma_{56} & \Gamma_{46} & \Gamma_{36} \\ \Gamma_{55} & \Gamma_{45} & \Gamma_{35} \end{pmatrix} &
 \begin{pmatrix} \Gamma_{56} & \Gamma_{46} & \Gamma_{36} \\ \Gamma_{52} & \Gamma_{42} & \Gamma_{32} \\ \Gamma_{54} & \Gamma_{44} & \Gamma_{34} \end{pmatrix} &
 \begin{pmatrix} \Gamma_{55} & \Gamma_{45} & \Gamma_{35} \\ \Gamma_{54} & \Gamma_{44} & \Gamma_{34} \\ \Gamma_{53} & \Gamma_{43} & \Gamma_{33} \end{pmatrix}
 \end{pmatrix} \Leftrightarrow \begin{pmatrix}
 \Gamma_{11} & \Gamma_{12} & \Gamma_{13} & \Gamma_{14} & \Gamma_{15} & \Gamma_{16} \\
 \Gamma_{21} & \Gamma_{22} & \Gamma_{23} & \Gamma_{24} & \Gamma_{25} & \Gamma_{26} \\
 \Gamma_{31} & \Gamma_{32} & \Gamma_{33} & \Gamma_{34} & \Gamma_{35} & \Gamma_{36} \\
 \Gamma_{41} & \Gamma_{42} & \Gamma_{43} & \Gamma_{44} & \Gamma_{45} & \Gamma_{46} \\
 \Gamma_{51} & \Gamma_{52} & \Gamma_{53} & \Gamma_{54} & \Gamma_{55} & \Gamma_{56} \\
 \Gamma_{61} & \Gamma_{62} & \Gamma_{63} & \Gamma_{64} & \Gamma_{65} & \Gamma_{66}
 \end{pmatrix}$$

Appendix C

Nonlinear Operators and Equations

C.1 Electrostriction Operators

The electrostriction operators L_1 and L_2 appearing in the wave equations, (2.22) and (2.23), are defined as:

$$L_1(E_x, E_y) = G \nabla \cdot \begin{pmatrix} -2E_x E_y \\ E_y^2 - E_x^2 \end{pmatrix} \quad (\text{C.1})$$

$$\begin{aligned} L_2(u_z, E_x, E_y) = & 2 \left(-4eE_x \frac{\partial E_x}{\partial y} - 3eE_x \frac{\partial E_y}{\partial x} - 3eE_y \frac{\partial E_x}{\partial x} + 2eE_y \frac{\partial E_y}{\partial y} + 2G \frac{\partial u_z}{\partial x} \left(\frac{\partial E_x}{\partial y} + \frac{\partial E_y}{\partial x} \right) \right. \\ & - G \frac{\partial u_z}{\partial y} \left(\frac{\partial E_y}{\partial y} - \frac{\partial E_x}{\partial x} \right) + 2GE_y \frac{\partial^2 u_z}{\partial x^2} - GE_y \frac{\partial^2 u_z}{\partial y^2} + 3GE_x \frac{\partial^2 u_z}{\partial x \partial y} \\ & \left. - 3GM(E_x^2 + E_y^2) \nabla \cdot \begin{pmatrix} E_x \\ E_y \end{pmatrix} - 6GME_x E_y \nabla \cdot \begin{pmatrix} E_y \\ E_x \end{pmatrix} \right) \end{aligned} \quad (\text{C.2})$$

In potential form, the operators reduce to:

$$L_1(\psi) = 2\left(\frac{\partial\psi}{\partial y}\frac{\partial^2\psi}{\partial y^2} - \frac{\partial\psi}{\partial y}\frac{\partial^2\psi}{\partial x^2} - 2\frac{\partial\psi}{\partial x}\frac{\partial^2\psi}{\partial x\partial y}\right) \quad (\text{C.3})$$

$$L_2(u_z, \psi) = eL_{2A}(u_z, \psi) + MGL_{2B}(u_z, \psi) \quad (\text{C.4})$$

$$\begin{aligned} L_{2A}(u_z, \psi) = & \frac{\partial\psi}{\partial y}\left(-6\frac{\partial^2\psi}{\partial x^2} + 4\frac{\partial^2\psi}{\partial y^2} - 4\frac{G}{e}\frac{\partial^2 u_z}{\partial x^2} + 2\frac{G}{e}\frac{\partial^2 u_z}{\partial y^2}\right) \\ & - \frac{\partial\psi}{\partial x}\left(14\frac{\partial^2\psi}{\partial x\partial y} + 6\frac{G}{e}\frac{\partial^2 u_z}{\partial x\partial y}\right) + 2\frac{G}{e}\frac{\partial u_z}{\partial y}\left(\frac{\partial^2\psi}{\partial y^2} - \frac{\partial^2\psi}{\partial x^2}\right) - 8\frac{G}{e}\frac{\partial u_z}{\partial x}\frac{\partial^2\psi}{\partial x\partial y} \end{aligned} \quad (\text{C.5})$$

$$L_{2B}(u_z, \psi) = 6\left(\frac{\partial^2\psi}{\partial x^2} + \frac{\partial^2\psi}{\partial y^2}\right)\left(\left(\frac{\partial\psi}{\partial y}\right)^2 + \left(\frac{\partial\psi}{\partial x}\right)^2\right) + 24\frac{\partial\psi}{\partial x}\frac{\partial\psi}{\partial y}\frac{\partial^2\psi}{\partial x\partial y} \quad (\text{C.6})$$

C.2 Equilibrium Equations

The discretized equilibrium equations for a four-mode expansion can be written as the following algebraic system:

$$p_{s1} + q_{s1} + \alpha_1 p_{s1} p_{s2} + \alpha_2 p_{s2} p_{s3} + \alpha_3 p_{s3} p_{s4} = 0 \quad (\text{C.7})$$

$$p_{s2} + q_{s2} + \alpha_4 p_{s1}^2 + \alpha_5 p_{s1} p_{s3} + \alpha_6 p_{s2} p_{s4} = 0 \quad (\text{C.8})$$

$$p_{s3} + q_{s3} + \alpha_7 p_{s1} p_{s2} + \alpha_8 p_{s1} p_{s4} = 0 \quad (\text{C.9})$$

$$p_{s4} + q_{s4} + \alpha_9 p_{s2}^2 + \alpha_{10} p_{s1} p_{s3} = 0 \quad (\text{C.10})$$

$$\begin{aligned} q_{s1} + \alpha_{11} p_{s1} + \alpha_{13} p_{s1} p_{s2} + \alpha_{16} p_{s2} p_{s3} + \alpha_{20} p_{s3} p_{s4} + \alpha_{23} p_{s2} q_{s1} + \alpha_{24} p_{s1} q_{s2} \\ + \alpha_{25} p_{s3} q_{s2} + \alpha_{26} p_{s2} q_{s3} + \alpha_{27} p_{s4} q_{s3} + \alpha_{28} p_{s3} q_{s4} + \alpha_{12} p_{s1}^3 + \alpha_{14} p_{s1} p_{s2}^2 + \alpha_{15} p_{s1}^2 p_{s3} \\ + \alpha_{17} p_{s2}^2 p_{s3} + \alpha_{18} p_{s1} p_{s3}^2 + \alpha_{22} p_{s1} p_{s4}^2 + \alpha_{19} p_{s1} p_{s2} p_{s4} + \alpha_{21} p_{s2} p_{s3} p_{s4} = \alpha_{29} V_{DC} \end{aligned} \quad (\text{C.11})$$

$$\begin{aligned}
& q_{s2} + \alpha_{11}p_{s2} + \alpha_{30}p_{s1}^2 + \alpha_{33}p_{s1}p_{s3} + \alpha_{37}p_{s2}p_{s4} + \alpha_{41}p_{s1}q_{s1} + \alpha_{42}p_{s3}q_{s1} \\
& + \alpha_{43}p_{s4}q_{s2} + \alpha_{44}p_{s1}q_{s3} + \alpha_{45}p_{s2}q_{s4} + \alpha_{32}p_{s2}^3 + \alpha_{31}p_{s1}^2p_{s2} + \alpha_{35}p_{s2}p_{s3}^2 \\
& + \alpha_{36}p_{s1}^2p_{s4} + \alpha_{39}p_{s3}^2p_{s4} + \alpha_{40}p_{s2}p_{s4}^2 + \alpha_{34}p_{s1}p_{s2}p_{s3} + \alpha_{38}p_{s1}p_{s3}p_{s4} = 0
\end{aligned} \tag{C.12}$$

$$\begin{aligned}
& q_{s3} + \alpha_{11}p_{s3} + \alpha_{47}p_{s1}p_{s2} + \alpha_{52}p_{s1}p_{s4} + \alpha_{56}p_{s2}q_{s1} + \alpha_{57}p_{s4}q_{s1} \\
& + \alpha_{56}p_{s1}q_{s2} + \alpha_{58}p_{s1}q_{s4} + \alpha_{46}p_{s1}^3 + \alpha_{51}p_{s3}^3 + \alpha_{48}p_{s1}p_{s2}^2 + \alpha_{49}p_{s1}^2p_{s3} \\
& + \alpha_{50}p_{s2}^2p_{s3} + \alpha_{55}p_{s3}p_{s4}^2 + \alpha_{53}p_{s1}p_{s2}p_{s4} + \alpha_{54}p_{s2}p_{s3}p_{s4} = \alpha_{59}V_{DC}
\end{aligned} \tag{C.13}$$

$$\begin{aligned}
& q_{s4} + \alpha_{11}p_{s4} + \alpha_{61}p_{s2}^2 + \alpha_{62}p_{s1}p_{s3} + \alpha_{69}p_{s3}q_{s1} + \alpha_{70}p_{s2}q_{s2} + \alpha_{69}p_{s1}q_{s3} + \alpha_{68}p_{s4}^3 \\
& + \alpha_{60}p_{s1}^2p_{s2} + \alpha_{64}p_{s2}p_{s3}^2 + \alpha_{65}p_{s1}^2p_{s4} + \alpha_{66}p_{s2}^2p_{s4} + \alpha_{67}p_{s3}^2p_{s4} + \alpha_{63}p_{s1}p_{s2}p_{s3} = 0
\end{aligned} \tag{C.14}$$

where q_{si} and p_{si} are the static modal coordinates and the coefficients α_i depend on the substrate properties and the permittivity ratio r .

C.3 Equations of Motion

The discretized dynamic system for a four-mode expansion is made of the following set of ordinary differential equations:

$$\begin{aligned}
& \ddot{q}_1 + \alpha_{75}\dot{q}_1 + \alpha_{71}q_1 + (\alpha_{71} + \alpha_{72}p_{s2})p_1 + (\alpha_{72}p_{s1} + \alpha_{73}p_{s3})p_2 \\
& + (\alpha_{73}p_{s2} + \alpha_{74}p_{s4})p_3 + \alpha_{74}p_{s3}p_4 + \alpha_{72}p_1p_2 + \alpha_{73}p_2p_3 + \alpha_{74}p_3p_4 = 0
\end{aligned} \tag{C.15}$$

$$\begin{aligned}
& \ddot{q}_2 + \alpha_{75}\dot{q}_2 + \alpha_{79}q_2 + (\alpha_{76}p_{s1} + \alpha_{77}p_{s3})p_1 + (\alpha_{79} + \alpha_{80}p_{s4})p_2 \\
& + \alpha_{77}p_{s1}p_3 + \alpha_{80}p_{s2}p_4 + \alpha_{77}p_1p_3 + \alpha_{80}p_2p_4 + \alpha_{78}p_1^2 = 0
\end{aligned} \tag{C.16}$$

$$\begin{aligned}
& \ddot{q}_3 + \alpha_{75}\dot{q}_3 + \alpha_{83}q_3 + (\alpha_{82}p_{s4} + \alpha_{81}p_{s2})p_1 + \alpha_{83}p_3 \\
& + \alpha_{81}p_{s1}p_2 + \alpha_{82}p_{s1}p_4 + \alpha_{81}p_1p_2 + \alpha_{82}p_1p_4 = 0
\end{aligned} \tag{C.17}$$

$$\ddot{q}_4 + \alpha_{75}\dot{q}_4 + \alpha_{87}q_4 + \alpha_{87}p_4 + \alpha_{84}p_{s3}p_1 + \alpha_{85}p_{s2}p_2 + \alpha_{84}p_{s1}p_3 + \alpha_{84}p_1p_3 + \alpha_{86}p_2^2 = 0 \tag{C.18}$$

$$\begin{aligned}
& \alpha_{90}p_{s1}^2\dot{p}_1 + \alpha_{91}p_{s2}\dot{p}_1 + \alpha_{14}p_{s2}^2\dot{p}_1 + \alpha_{18}p_{s3}^2\dot{p}_1 + \alpha_{22}p_{s4}^2\dot{p}_1 + \alpha_{93}q_{s2}\dot{p}_1 + \alpha_{90}p_1^2\dot{p}_1 + \alpha_{91}p_2\dot{p}_1 \\
& + \alpha_{14}p_2^2\dot{p}_1 + \alpha_{18}p_3^2\dot{p}_1 + \alpha_{22}p_4^2\dot{p}_1 + \alpha_{93}q_2\dot{p}_1 + \alpha_{91}p_{s1}\dot{p}_2 + \alpha_{98}p_{s3}\dot{p}_2 + \alpha_{100}q_{s1}\dot{p}_2 + \alpha_{101}q_{s3}\dot{p}_2 \\
& + \alpha_{91}p_1\dot{p}_2 + \alpha_{98}p_3\dot{p}_2 + \alpha_{100}q_1\dot{p}_2 + \alpha_{101}q_3\dot{p}_2 + \alpha_{15}p_{s1}^2\dot{p}_3 + \alpha_{98}p_{s2}\dot{p}_3 + \alpha_{17}p_{s2}^2\dot{p}_3 + \alpha_{102}p_{s4}\dot{p}_3 \\
& + \alpha_{103}q_{s2}\dot{p}_3 + \alpha_{104}q_{s4}\dot{p}_3 + \alpha_{15}p_1^2\dot{p}_3 + \alpha_{98}p_2\dot{p}_3 + \alpha_{17}p_2^2\dot{p}_3 + \alpha_{102}p_4\dot{p}_3 + \alpha_{103}q_2\dot{p}_3 + \alpha_{104}q_4\dot{p}_3 \\
& + \alpha_{102}p_{s3}\dot{p}_4 + \alpha_{105}q_{s3}\dot{p}_4 + \alpha_{102}p_3\dot{p}_4 + \alpha_{105}q_3\dot{p}_4 + \alpha_{100}p_{s2}\dot{q}_1 + \alpha_{100}p_2\dot{q}_1 + \alpha_{93}p_{s1}\dot{q}_2 + \alpha_{103}p_{s3}\dot{q}_2 \\
& + \alpha_{93}p_1\dot{q}_2 + \alpha_{103}p_3\dot{q}_2 + \alpha_{101}p_{s2}\dot{q}_3 + \alpha_{105}p_{s4}\dot{q}_3 + \alpha_{101}p_2\dot{q}_3 + \alpha_{105}p_4\dot{q}_3 + \alpha_{104}p_{s3}\dot{q}_4 + \alpha_{104}p_3\dot{q}_4 \\
& + \alpha_{92}p_{s1}p_{s3}\dot{p}_1 + \alpha_{19}p_{s2}p_{s4}\dot{p}_1 + \alpha_{94}p_{s1}p_1\dot{p}_1 + \alpha_{92}p_{s3}p_1\dot{p}_1 + \alpha_{95}p_{s2}p_2\dot{p}_1 + \alpha_{19}p_{s4}p_2\dot{p}_1 \\
& + \alpha_{92}p_{s1}p_3\dot{p}_1 + \alpha_{96}p_{s3}p_3\dot{p}_1 + \alpha_{92}p_1p_3\dot{p}_1 + \alpha_{19}p_{s2}p_4\dot{p}_1 + \alpha_{97}p_{s4}p_4\dot{p}_1 + \alpha_{19}p_2p_4\dot{p}_1 + \alpha_{95}p_{s1}p_{s2}\dot{p}_2 \\
& + \alpha_{99}p_{s2}p_{s3}\dot{p}_2 + \alpha_{19}p_{s1}p_{s4}\dot{p}_2 + \alpha_{21}p_{s3}p_{s4}\dot{p}_2 + \alpha_{95}p_{s2}p_1\dot{p}_2 + \alpha_{19}p_{s4}p_1\dot{p}_2 + \alpha_{95}p_{s1}p_2\dot{p}_2 \\
& + \alpha_{99}p_{s3}p_2\dot{p}_2 + \alpha_{95}p_1p_2\dot{p}_2 + \alpha_{99}p_{s2}p_3\dot{p}_2 + \alpha_{21}p_{s4}p_3\dot{p}_2 + \alpha_{99}p_2p_3\dot{p}_2 + \alpha_{19}p_{s1}p_4\dot{p}_2 + \alpha_{21}p_{s3}p_4\dot{p}_2 \\
& + \alpha_{19}p_1p_4\dot{p}_2 + \alpha_{21}p_3p_4\dot{p}_2 + \alpha_{96}p_{s1}p_{s3}\dot{p}_3 + \alpha_{21}p_{s2}p_{s4}\dot{p}_3 + \alpha_{92}p_{s1}p_1\dot{p}_3 + \alpha_{96}p_{s3}p_1\dot{p}_3 + \alpha_{99}p_{s2}p_2\dot{p}_3 \\
& + \alpha_{21}p_{s4}p_2\dot{p}_3 + \alpha_{96}p_{s1}p_3\dot{p}_3 + \alpha_{96}p_1p_3\dot{p}_3 + \alpha_{21}p_{s2}p_4\dot{p}_3 + \alpha_{21}p_2p_4\dot{p}_3 + \alpha_{19}p_{s1}p_{s2}\dot{p}_4 + \alpha_{21}p_{s2}p_{s3}\dot{p}_4 \\
& + \alpha_{97}p_{s1}p_{s4}\dot{p}_4 + \alpha_{19}p_{s2}p_1\dot{p}_4 + \alpha_{97}p_{s4}p_1\dot{p}_4 + \alpha_{19}p_{s1}p_2\dot{p}_4 + \alpha_{21}p_{s3}p_2\dot{p}_4 + \alpha_{19}p_1p_2\dot{p}_4 + \alpha_{21}p_{s2}p_3\dot{p}_4 \\
& + \alpha_{21}p_2p_3\dot{p}_4 + \alpha_{97}p_{s1}p_4\dot{p}_4 + \alpha_{97}p_1p_4\dot{p}_4 + \alpha_{88}p_{s1} + \alpha_{89}p_1 + \alpha_{11}\dot{p}_1 + \alpha_{106}\dot{q}_1 = \alpha_{107}V_{AC} \sin(\Omega t)
\end{aligned} \tag{C.19}$$

$$\begin{aligned}
& \alpha_{11}\dot{p}_2 + \alpha_{106}\dot{q}_2 + \alpha_{108}p_{s1}\dot{p}_1 + \alpha_{110}p_{s3}\dot{p}_1 + \alpha_{112}q_{s1}\dot{p}_1 + \alpha_{113}q_{s3}\dot{p}_1 + \alpha_{108}p_1\dot{p}_1 \\
& + \alpha_{110}p_3\dot{p}_1 + \alpha_{112}q_1\dot{p}_1 + \alpha_{113}q_3\dot{p}_1 + \alpha_{31}p_{s1}^2\dot{p}_2 + \alpha_{114}p_{s2}^2\dot{p}_2 + \alpha_{35}p_{s3}^2\dot{p}_2 + \alpha_{115}p_{s4}\dot{p}_2 \\
& + \alpha_{40}p_{s4}^2\dot{p}_2 + \alpha_{116}q_{s4}\dot{p}_2 + \alpha_{31}p_1^2\dot{p}_2 + \alpha_{114}p_2^2\dot{p}_2 + \alpha_{35}p_3^2\dot{p}_2 + \alpha_{115}p_4\dot{p}_2 + \alpha_{40}p_4^2\dot{p}_2 \\
& + \alpha_{116}q_4\dot{p}_2 + \alpha_{110}p_{s1}\dot{p}_3 + \alpha_{121}q_{s1}\dot{p}_3 + \alpha_{110}p_1\dot{p}_3 + \alpha_{121}q_1\dot{p}_3 + \alpha_{36}p_{s1}^2\dot{p}_4 + \alpha_{115}p_{s2}\dot{p}_4 \\
& + \alpha_{39}p_{s3}^2\dot{p}_4 + \alpha_{122}q_{s2}\dot{p}_4 + \alpha_{36}p_1^2\dot{p}_4 + \alpha_{115}p_2\dot{p}_4 + \alpha_{39}p_3^2\dot{p}_4 + \alpha_{122}q_2\dot{p}_4 + \alpha_{112}p_{s1}\dot{q}_1 \\
& + \alpha_{121}p_{s3}\dot{q}_1 + \alpha_{112}p_1\dot{q}_1 + \alpha_{121}p_3\dot{q}_1 + \alpha_{122}p_{s4}\dot{q}_2 + \alpha_{122}p_4\dot{q}_2 + \alpha_{113}p_{s1}\dot{q}_3 + \alpha_{113}p_1\dot{q}_3 \\
& + \alpha_{116}p_{s2}\dot{q}_4 + \alpha_{116}p_2\dot{q}_4 + \alpha_{109}p_{s1}p_{s2}\dot{p}_1 + \alpha_{34}p_{s2}p_{s3}\dot{p}_1 + \alpha_{111}p_{s1}p_{s4}\dot{p}_1 + \alpha_{38}p_{s3}p_{s4}\dot{p}_1 \\
& + \alpha_{109}p_{s2}p_1\dot{p}_1 + \alpha_{111}p_{s4}p_1\dot{p}_1 + \alpha_{109}p_{s1}p_2\dot{p}_1 + \alpha_{34}p_{s3}p_2\dot{p}_1 + \alpha_{109}p_1p_2\dot{p}_1 + \alpha_{34}p_{s2}p_3\dot{p}_1 \\
& + \alpha_{38}p_{s4}p_3\dot{p}_1 + \alpha_{34}p_2p_3\dot{p}_1 + \alpha_{111}p_{s1}p_4\dot{p}_1 + \alpha_{38}p_{s3}p_4\dot{p}_1 + \alpha_{111}p_1p_4\dot{p}_1 + \alpha_{38}p_3p_4\dot{p}_1 \\
& + \alpha_{34}p_{s1}p_{s3}\dot{p}_2 + \alpha_{109}p_{s1}p_1\dot{p}_2 + \alpha_{34}p_{s3}p_1\dot{p}_2 + \alpha_{117}p_{s2}p_2\dot{p}_2 + \alpha_{34}p_{s1}p_3\dot{p}_2 + \alpha_{118}p_{s3}p_3\dot{p}_2 \\
& + \alpha_{34}p_1p_3\dot{p}_2 + \alpha_{119}p_{s4}p_4\dot{p}_2 + \alpha_{34}p_{s1}p_{s2}\dot{p}_3 + \alpha_{118}p_{s2}p_{s3}\dot{p}_3 + \alpha_{38}p_{s1}p_{s4}\dot{p}_3 + \alpha_{120}p_{s3}p_{s4}\dot{p}_3 \\
& + \alpha_{34}p_{s2}p_1\dot{p}_3 + \alpha_{38}p_{s4}p_1\dot{p}_3 + \alpha_{34}p_{s1}p_2\dot{p}_3 + \alpha_{118}p_{s3}p_2\dot{p}_3 + \alpha_{34}p_1p_2\dot{p}_3 + \alpha_{118}p_{s2}p_3\dot{p}_3 \\
& + \alpha_{120}p_{s4}p_3\dot{p}_3 + \alpha_{118}p_2p_3\dot{p}_3 + \alpha_{38}p_{s1}p_4\dot{p}_3 + \alpha_{120}p_{s3}p_4\dot{p}_3 + \alpha_{38}p_1p_4\dot{p}_3 + \alpha_{120}p_3p_4\dot{p}_3 \\
& + \alpha_{38}p_{s1}p_{s3}\dot{p}_4 + \alpha_{119}p_{s2}p_{s4}\dot{p}_4 + \alpha_{111}p_{s1}p_1\dot{p}_4 + \alpha_{38}p_{s3}p_1\dot{p}_4 + \alpha_{119}p_{s4}p_2\dot{p}_4 + \alpha_{38}p_{s1}p_3\dot{p}_4 \\
& + \alpha_{120}p_{s3}p_3\dot{p}_4 + \alpha_{38}p_1p_3\dot{p}_4 + \alpha_{119}p_{s2}p_4\dot{p}_4 + \alpha_{119}p_2p_4\dot{p}_4 + \alpha_{88}p_{s2} + \alpha_{89}p_2 = 0
\end{aligned} \tag{C.20}$$

$$\begin{aligned}
& \alpha_{11}\dot{p}_3 + \alpha_{106}\dot{q}_3 + \alpha_{123}p_{s1}^2\dot{p}_1 + \alpha_{124}p_{s2}\dot{p}_1 + \alpha_{48}p_{s2}^2\dot{p}_1 + \alpha_{126}p_{s4}\dot{p}_1 + \alpha_{127}q_{s2}\dot{p}_1 \\
& + \alpha_{128}q_{s4}\dot{p}_1 + \alpha_{123}p_1^2\dot{p}_1 + \alpha_{124}p_2\dot{p}_1 + \alpha_{48}p_2^2\dot{p}_1 + \alpha_{126}p_4\dot{p}_1 + \alpha_{127}q_2\dot{p}_1 + \alpha_{128}q_4\dot{p}_1 \\
& + \alpha_{124}p_{s1}\dot{p}_2 + \alpha_{127}q_{s1}\dot{p}_2 + \alpha_{124}p_1\dot{p}_2 + \alpha_{127}q_1\dot{p}_2 + \alpha_{49}p_{s1}^2\dot{p}_3 + \alpha_{50}p_{s2}^2\dot{p}_3 + \alpha_{132}p_{s3}^2\dot{p}_3 \\
& + \alpha_{55}p_{s4}^2\dot{p}_3 + \alpha_{49}p_1^2\dot{p}_3 + \alpha_{50}p_2^2\dot{p}_3 + \alpha_{132}p_3^2\dot{p}_3 + \alpha_{55}p_4^2\dot{p}_3 + \alpha_{126}p_{s1}\dot{p}_4 + \alpha_{135}q_{s1}\dot{p}_4 \\
& + \alpha_{126}p_1\dot{p}_4 + \alpha_{135}q_1\dot{p}_4 + \alpha_{127}p_{s2}\dot{q}_1 + \alpha_{135}p_{s4}\dot{q}_1 + \alpha_{127}p_2\dot{q}_1 + \alpha_{135}p_4\dot{q}_1 + \alpha_{127}p_{s1}\dot{q}_2 \\
& + \alpha_{127}p_1\dot{q}_2 + \alpha_{128}p_{s1}\dot{q}_4 + \alpha_{128}p_1\dot{q}_4 + \alpha_{125}p_{s1}p_{s3}\dot{p}_1 + \alpha_{53}p_{s2}p_{s4}\dot{p}_1 + \alpha_{129}p_{s1}p_1\dot{p}_1 \\
& + \alpha_{125}p_{s3}p_1\dot{p}_1 + \alpha_{130}p_{s2}p_2\dot{p}_1 + \alpha_{53}p_{s4}p_2\dot{p}_1 + \alpha_{125}p_{s1}p_3\dot{p}_1 + \alpha_{125}p_1p_3\dot{p}_1 + \alpha_{53}p_{s2}p_4\dot{p}_1 \\
& + \alpha_{53}p_2p_4\dot{p}_1 + \alpha_{130}p_{s1}p_{s2}\dot{p}_2 + \alpha_{131}p_{s2}p_{s3}\dot{p}_2 + \alpha_{53}p_{s1}p_{s4}\dot{p}_2 + \alpha_{54}p_{s3}p_{s4}\dot{p}_2 \\
& + \alpha_{130}p_{s2}p_1\dot{p}_2 + \alpha_{53}p_{s4}p_1\dot{p}_2 + \alpha_{130}p_{s1}p_2\dot{p}_2 + \alpha_{131}p_{s3}p_2\dot{p}_2 + \alpha_{130}p_1p_2\dot{p}_2 + \alpha_{131}p_{s2}p_3\dot{p}_2 \\
& + \alpha_{54}p_{s4}p_3\dot{p}_2 + \alpha_{131}p_2p_3\dot{p}_2 + \alpha_{53}p_{s1}p_4\dot{p}_2 + \alpha_{54}p_{s3}p_4\dot{p}_2 + \alpha_{53}p_1p_4\dot{p}_2 + \alpha_{54}p_3p_4\dot{p}_2 \\
& + \alpha_{54}p_{s2}p_{s4}\dot{p}_3 + \alpha_{125}p_{s1}p_1\dot{p}_3 + \alpha_{131}p_{s2}p_2\dot{p}_3 + \alpha_{54}p_{s4}p_2\dot{p}_3 + \alpha_{133}p_{s3}p_3\dot{p}_3 \\
& + \alpha_{54}p_{s2}p_4\dot{p}_3 + \alpha_{134}p_{s4}p_4\dot{p}_3 + \alpha_{54}p_2p_4\dot{p}_3 + \alpha_{53}p_{s1}p_{s2}\dot{p}_4 + \alpha_{54}p_{s2}p_{s3}\dot{p}_4 + \alpha_{134}p_{s3}p_{s4}\dot{p}_4 \\
& + \alpha_{53}p_{s2}p_1\dot{p}_4 + \alpha_{53}p_{s1}p_2\dot{p}_4 + \alpha_{54}p_{s3}p_2\dot{p}_4 + \alpha_{53}p_1p_2\dot{p}_4 + \alpha_{54}p_{s2}p_3\dot{p}_4 + \alpha_{134}p_{s4}p_3\dot{p}_4 \\
& + \alpha_{54}p_2p_3\dot{p}_4 + \alpha_{134}p_{s3}p_4\dot{p}_4 + \alpha_{134}p_3p_4\dot{p}_4 + \alpha_{88}p_{s3} + \alpha_{89}p_3 = \alpha_{136}V_{AC} \sin(\Omega t)
\end{aligned} \tag{C.21}$$

$$\begin{aligned}
& \alpha_{11}\dot{p}_4 + \alpha_{106}\dot{q}_4 + \alpha_{138}p_{s3}\dot{p}_1 + \alpha_{140}q_{s3}\dot{p}_1 + \alpha_{138}p_3\dot{p}_1 + \alpha_{140}q_3\dot{p}_1 + \alpha_{141}p_{s1}^2\dot{p}_2 + \alpha_{142}p_{s2}\dot{p}_2 \\
& + \alpha_{64}p_{s3}^2\dot{p}_2 + \alpha_{144}q_{s2}\dot{p}_2 + \alpha_{141}p_1^2\dot{p}_2 + \alpha_{142}p_2\dot{p}_2 + \alpha_{64}p_3^2\dot{p}_2 + \alpha_{144}q_2\dot{p}_2 + \alpha_{138}p_{s1}\dot{p}_3 \\
& + \alpha_{140}q_{s1}\dot{p}_3 + \alpha_{138}p_1\dot{p}_3 + \alpha_{140}q_1\dot{p}_3 + \alpha_{65}p_{s1}^2\dot{p}_4 + \alpha_{66}p_{s2}^2\dot{p}_4 + \alpha_{67}p_{s3}^2\dot{p}_4 + \alpha_{147}p_{s4}^2\dot{p}_4 \\
& + \alpha_{65}p_1^2\dot{p}_4 + \alpha_{66}p_2^2\dot{p}_4 + \alpha_{67}p_3^2\dot{p}_4 + \alpha_{147}p_4^2\dot{p}_4 + \alpha_{140}p_{s3}\dot{q}_1 + \alpha_{140}p_3\dot{q}_1 + \alpha_{144}p_{s2}\dot{q}_2 + \alpha_{144}p_2\dot{q}_2 \\
& + \alpha_{140}p_{s1}\dot{q}_3 + \alpha_{140}p_1\dot{q}_3 + \alpha_{137}p_{s1}p_{s2}\dot{p}_1 + \alpha_{63}p_{s2}p_{s3}\dot{p}_1 + \alpha_{139}p_{s1}p_{s4}\dot{p}_1 + \alpha_{137}p_{s2}p_1\dot{p}_1 \\
& + \alpha_{139}p_{s4}p_1\dot{p}_1 + \alpha_{137}p_{s1}p_2\dot{p}_1 + \alpha_{63}p_{s3}p_2\dot{p}_1 + \alpha_{137}p_1p_2\dot{p}_1 + \alpha_{63}p_{s2}p_3\dot{p}_1 + \alpha_{63}p_2p_3\dot{p}_1 \\
& + \alpha_{139}p_{s1}p_4\dot{p}_1 + \alpha_{139}p_1p_4\dot{p}_1 + \alpha_{63}p_{s1}p_{s3}\dot{p}_2 + \alpha_{143}p_{s2}p_{s4}\dot{p}_2 + \alpha_{137}p_{s1}p_1\dot{p}_2 + \alpha_{63}p_{s3}p_1\dot{p}_2 \\
& + \alpha_{143}p_{s4}p_2\dot{p}_2 + \alpha_{63}p_{s1}p_3\dot{p}_2 + \alpha_{145}p_{s3}p_3\dot{p}_2 + \alpha_{63}p_1p_3\dot{p}_2 + \alpha_{143}p_{s2}p_4\dot{p}_2 + \alpha_{143}p_2p_4\dot{p}_2 \\
& + \alpha_{63}p_{s1}p_{s2}\dot{p}_3 + \alpha_{145}p_{s2}p_{s3}\dot{p}_3 + \alpha_{146}p_{s3}p_{s4}\dot{p}_3 + \alpha_{63}p_{s2}p_1\dot{p}_3 + \alpha_{63}p_{s1}p_2\dot{p}_3 + \alpha_{145}p_{s3}p_2\dot{p}_3 \\
& + \alpha_{63}p_1p_2\dot{p}_3 + \alpha_{145}p_{s2}p_3\dot{p}_3 + \alpha_{146}p_{s4}p_3\dot{p}_3 + \alpha_{145}p_2p_3\dot{p}_3 + \alpha_{146}p_{s3}p_4\dot{p}_3 + \alpha_{146}p_3p_4\dot{p}_3 \\
& + \alpha_{139}p_{s1}p_1\dot{p}_4 + \alpha_{143}p_{s2}p_2\dot{p}_4 + \alpha_{146}p_{s3}p_3\dot{p}_4 + \alpha_{148}p_{s4}p_4\dot{p}_4 + \alpha_{88}p_{s4} + \alpha_{89}p_4 = 0
\end{aligned} \tag{C.22}$$